

Reducing Neutron Multiplicity Counting Bias for Plutonium Warhead Authentication

Malte Götttsche

Dissertation with the aim of achieving a doctoral degree
at the Faculty of Mathematics, Informatics and Natural Sciences

Department of Physics
of Universität Hamburg

2015, HAMBURG

Eidesstattliche Versicherung

Hiermit erkläre ich an Eides statt, dass ich die vorliegende Dissertationsschrift selbst verfasst und keine anderen als die angegebenen Quellen und Hilfsmittel benutzt habe.

Hamburg, den 05. März 2015

Malte Götsche

Day of oral defense: 05 June 2015

The following evaluators recommend the admission of the dissertation:

Prof. Dr. Gerald Kirchner

Prof. Dr. Götz Neuneck

Meinen Eltern

Acknowledgments

This work would not have been possible without strong support. I thank Gerald Kirchner for taking a lot of time and effort to discuss the physics and for his thorough and helpful comments on my writings. Throughout my studies, Götz Neuneck has been a real and honest supporter of my interdisciplinary endeavors. I am deeply grateful for his insights and wisdom. His continuous inspiration and backing are invaluable. I have been lucky to also have Caren Hagner encourage my research and have an open ear for all concerns. It is Martin Kalinowski who opened up so many opportunities early on in my career that enabled my engagement in international projects. Paolo Peerani not only facilitated my measurements in the PERLA laboratory in Ispra, but also took his time to advise me on various measurement and simulation issues. Ole Reistad is a source of inspiration for me; I profited a lot from my visits to Oslo and the student seminar we jointly organized. With my colleagues in Hamburg and those involved in the German Network Nuclear Disarmament Verification, my work has been embedded in fruitful discussions and support. Frederik Postelt ensured that I never lost sight of the idealism, always remembering why I do what I do. We have been and will continue to be a team! The discussions with Moritz Kütt have been very valuable. In Fabio Zeiser and Matthew McArthur, I found very intelligent and capable students that I had a good time working together with. The very helpful comments on the draft of my dissertation from Marie Alt, Claire Duvernet, Moritz Kütt, Frederik Postelt and Dimitrios Rompotis enhanced the quality of this work. Finally, I feel very privileged to have my family and friends. I am so grateful for being with Claire, she is my greatest gift! My parents did everything they could to support me in any situation. Without their unconditional trust and support, I would be far away from where and who I am today. Last but not least, I am grateful to all my friends for their encouragement and good times!

Abstract

Confidence in future nuclear arms control agreements could be enhanced by direct verification of warheads. It would include warhead authentication. This is the assessment based on measurements whether a declaration that a specific item is a nuclear warhead is true. An information barrier can be used to protect sensitive information during measurements. It could for example show whether attributes such as a fissile mass exceeding a threshold are met without indicating detailed measurement results. Neutron multiplicity measurements would be able to assess a plutonium fissile mass attribute if it were possible to show that their bias is low.

Plutonium measurements have been conducted with the He-3 based Passive Scrap Multiplicity Counter. The measurement data has been used as a reference to test the capacity of the Monte Carlo code MCNPX-PoliMi to simulate neutron multiplicity measurements. The simulation results with their uncertainties are in agreement with the experimental results. It is essential to use cross-sections which include neutron scattering with the detector's polyethylene molecular structure. Further MCNPX-PoliMi simulations have been conducted in order to study bias that occurs when measuring samples with large plutonium masses such as warheads.

Simulation results of solid and hollow metal spheres up to 6000 g show that the masses are underpredicted by as much as 20%. The main source of this bias has been identified in the false assumption that the neutron multiplication does not depend on the position where a spontaneous fission event occurred. The multiplication refers to the total number of neutrons leaking a sample after a primary spontaneous fission event, taking induced fission into consideration. The correction of the analysis has been derived and implemented in a MATLAB code. It depends on four geometry-dependent correction coefficients. When the sample configuration is fully known,

these can be exactly determined and remove this type of bias.

As the exact configuration of warheads includes sensitive information which must be protected, it will not be fully declared and the coefficients must be estimated. Assuming that the plutonium component of warheads can be approximated by hollow spheres, it is shown that the coefficients could be approximated if the thickness of the hollow sphere were known. Other parameters such as the radius have a very small influence: Only knowing the thickness introduces a negligible bias of 1% for the fissile mass. If the thickness remained unknown, a less accurate estimate of the correction coefficients could also be estimated from the multiplication which is directly measured by neutron multiplicity counting. Bias from this approach is smaller than using the analysis based on the false assumption. In order to study the influence of further materials in the warhead and the container the warhead would be placed in, correction coefficients were also studied for plutonium spheres surrounded by polyethylene. The result of the polyethylene is that the correction coefficients are somewhat smaller. Applying the correction coefficients that do not take further materials into account to these cases, the fissile masses are overestimated by around 7% in exemplary simulations. Bias would be further reduced if information on further materials could be included in the correction coefficients' assessment.

By having developed a method to reduce bias, the reliability of neutron multiplicity counting measurements has been increased. The obtained level of reliability may suffice in the context of additional verification measures as these also add to the overall confidence.

Zusammenfassung

Vertrauen in zukünftige nukleare Rüstungskontrollvereinbarungen könnte durch direkte Verifikation von Sprengköpfen erhöht werden. Dies würde die Authentifizierung von Sprengköpfen beinhalten. Das ist die Überprüfung anhand von Messungen, ob eine Deklaration, dass es sich bei einem spezifischen Objekt um einen Sprengkopf handelt, wahr ist. Eine Informationsbarriere könnte eingesetzt werden um sensitive Informationen bei den Messungen zu schützen. So könnte zum Beispiel angezeigt werden, ob Attribute wie das Überschreiten eines Grenzwertes einer spaltbaren Masse erfüllt sind, ohne dabei genaue Messergebnisse preiszugeben. Neutronenmultiplizitätsmessungen wären geeignet ein solches Plutoniummasseattribut zu evaluieren falls gezeigt werden könnte, dass systematische Unsicherheiten gering sind.

Plutoniummessungen wurden mit dem He-3 basierten Passive Scrap Multiplicity Counter durchgeführt. Die Messdaten wurden als Referenz verwendet, um die Fähigkeit des Monte Carlo Codes MCNPX-PoliMi zu testen, Multiplizitätsmessungen zu simulieren. Die Simulationsergebnisse stimmen innerhalb ihrer Unsicherheiten mit den experimentellen Resultaten überein. Dafür ist es notwendig Wirkungsquerschnitte zu verwenden, die die Neutronenstreuung an der Molekülstruktur von Polyethylen im Detektor beinhalten. Weitere MCNPX-PoliMi Simulationen wurden durchgeführt, um systematische Unsicherheiten zu untersuchen, die bei Messungen großer Plutoniummassen, wie bei Sprengköpfen, vorhanden sind.

Simulationsergebnisse von Voll- und Hohlkugeln aus Metall bis 6000 g zeigen, dass die Massen um bis zu 20% unterschätzt werden. Die relevanteste Ursache der systematischen Unsicherheit wurde in der falschen Annahme identifiziert, dass die Neutronenmultiplikation nicht von dem Ort der Spontanspaltung abhängt. Die Multiplikation ist die gesamte Anzahl an Neutronen nach einer primären Spontanspal-

tung, die unter Berücksichtigung induzierter Spaltung einer Probe entkommt. Die korrigierte Analyse wurde hergeleitet und in einem MATLAB Skript implementiert. Sie hängt von vier Korrekturkoeffizienten ab. Falls die Konfiguration einer Probe vollständig bekannt ist, können diese exakt bestimmt werden und beseitigen diese systematische Unsicherheit.

Da die genaue Konfiguration der Sprengköpfe sensitive Informationen beinhaltet, die geschützt werden müssen, wird sie nicht vollständig deklariert werden, sodass die Koeffizienten abgeschätzt werden müssen. In der Annahme, dass die Plutoniumkomponente der Sprengköpfe durch Hohlkugeln angenähert werden kann wird gezeigt, dass die Koeffizienten genähert werden können, wenn die Dicke der Hohlkugel bekannt ist. Andere Parameter wie der Radius haben einen geringen Einfluss: Wenn ausschließlich die Dicke bekannt ist, führt dies zu einer vernachlässigbaren Unsicherheit von 1% für die spaltbare Masse. Falls die Dicke unbekannt bleibt, können die Korrekturkoeffizienten mithilfe der Multiplikation, einem direkten Ergebnis der Multiplizitätsmessungen, mit geringerer Genauigkeit geschätzt werden. Die systematische Unsicherheit ist geringer als bei der Analyse mit der falschen Annahme. Um den Einfluss weiterer Materialien im Sprengkopf bzw. im Container, in dem der Sprengkopf gelagert wäre, zu untersuchen, wurden die Korrekturkoeffizienten für Plutoniumkugeln bestimmt, die von Polyethylen umgeben sind. Das Ergebnis des Polyethylens sind etwas geringere Korrekturkoeffizienten. Werden auf diese Fälle die Korrekturkoeffizienten, die keine weiteren Materialien berücksichtigen, angewandt, werden die spaltbaren Massen in beispielhaften Simulationen um 7% überschätzt. Die systematische Unsicherheit würde weiter reduziert werden, falls Informationen zu weiteren Materialien für die Bestimmung der Korrekturkoeffizienten verwendet werden könnten.

Durch die entwickelte Methode, die systematische Unsicherheit zu reduzieren, konnte die Zuverlässigkeit von Neutronenmultiplizitätsmessungen erhöht werden. Die erreichte Zuverlässigkeit könnte im Kontext zusätzlicher Verifikationsmaßnahmen ausreichen, da diese ebenfalls zum Gesamtvertrauen beitragen.

Preface

The Non-Proliferation Treaty has been agreed upon because it not only includes the nonproliferation obligations, but also calls for nuclear disarmament. Arsenals have been significantly reduced, but still it seems that not all states take disarmament obligations very seriously. I dream of a world free of nuclear weapons - in my lifetime!

I believe that nuclear disarmament can only be sustainable when the international community has confidence in it. This is not only a challenge for nuclear weapon states, but for non-nuclear weapon states alike. I see it as a requirement that both must work jointly on effective verification measures. While there is a lot of technical work in some nuclear weapon states, capacities and capabilities must be developed particularly in non-nuclear weapon states. The goal of my work in the past few years was to make a modest contribution towards the development of according concepts and techniques.

My research has been part of a project at the Carl Friedrich von Weizsäcker-Centre for Science and Peace Research in cooperation with the Institute for Peace Research and Security Policy, entitled “Nuclear Weapons Authentication with an Attribute Information Barrier: A Feasibility Study.” Without providing the details yet, war-head authentication is considered a central component of an overall disarmament verification regime. In its core, it is a technical challenge as appropriate measurement techniques must be developed. However, it also concerns national and international security issues and thereby it must include policy deliberations as well. This has been reflected in the project’s aim: to demonstrate the technical feasibility taking political boundary conditions into consideration. The project was funded by the German Foundation for Peace Research.

This dissertation focuses on the physical and technical challenges and results. Regarding political boundary conditions, it was a pleasure to be able to contribute my non-nuclear weapon state perspective to the international Verification Pilot Project of the Nuclear Threat Initiative. I am co-author of its report

Nuclear Threat Initiative, *Innovating Verification: New Tools & New Actors to Reduce Nuclear Risks, Verifying Baseline Declarations of Nuclear Warheads and Materials* (2014).

Some further contents of this dissertation have also been published:

M. Götttsche and G. Kirchner, “Measurement techniques for warhead authentication with attributes: Advantages and limitations,” *Science & Global Security* **22**, 83-110 (2014).

M. Götttsche and G. Kirchner, “MCNPX-PoliMi simulation capacity using thermal neutron cross-sections to assess the reliability of the neutron multiplicity mass analysis where shielding is unknown,” in *55th INMM Annual Meeting* (Atlanta, 2014).

M. Götttsche and G. Kirchner, “Neutron multiplicity counting for future verification missions: Bias when the sample configuration remains unknown,” in *2014 IAEA Symposium on International Safeguards* (Vienna, 2014).

As part of the research project, I have also guided the students Matthew McArthur (3 month internship June to August 2013) and Fabio Zeiser (Bachelor thesis delivered in August 2013) at the Centre for Science and Peace Research. Wherever this dissertation covers joint research results, it is indicated per footnote.

Contents

1	Introduction	1
1.1	Information Barriers	4
1.2	Measurement Issues	6
1.3	Research Task and Methodology	7
2	Neutron Multiplicity Counting	9
2.1	Neutron Sources and Interactions	9
2.1.1	Spontaneous and induced fission	9
2.1.2	Further interactions	12
2.2	Detection	14
2.3	Basis of Neutron Multiplicity Counting	15
2.3.1	Description of neutron source	17
2.3.2	Extraction of correlated moments from the measurement	19
2.3.3	Calculating the plutonium fissile mass	22
3	Neutron Multiplicity Measurements of Plutonium Samples	23
3.1	He-3 Detector	23
3.2	Plutonium Samples and Measurements	25
4	Monte Carlo Simulation Capacity	29
4.1	Simulation tools	29
4.1.1	MCNPX-PoliMi	29
4.1.2	Implementation of the multiplicity analysis	30
4.2	Thermal Neutron Scattering	31
4.3	Simulation Results	32
4.3.1	Systematic and statistical uncertainties	34
4.3.2	Simulation capacity assessment	38
5	Neutron Multiplicity Counting Bias	40

5.1	Bias from Inadequate Knowledge of Parameters	41
5.1.1	Preparations for further bias studies	43
5.1.2	Simulation uncertainties	45
5.2	Bias for Highly Multiplicative Plutonium Samples	46
5.2.1	Spatially variant multiplication	48
5.2.2	Existing correction model	55
5.2.3	Corrected multiplicity analysis	58
5.2.4	Testing the analysis	59
5.2.5	Reducing the bias for warhead authentication	61
5.3	Bias from Reflected Configurations	69
5.3.1	Correction factors	73
6	Conclusions and Implications	77
	References	81
A	Elements of the Mathematical Formalism of Neutron Multiplicity Counting	87
A.1	The Multiplicity Distribution of Emitted Neutrons	87
A.2	The Multiplicity Distribution of Detected Neutrons	89
A.3	The Multiplicity Distribution of Detected and Counted Neutrons	90
A.4	Solving S , D and T	92
B	Measurements and Simulations	94
C	The Thermal Neutron Scattering Kernel	98
D	Derivation of the Corrected Multiplicity Analysis	101
E	Graphs of the Correction Coefficients	103

List of Figures

2.1	Pu-239 cross-sections of induced fission, (n, γ) and (n, n')	11
2.2	Pu-240 cross-sections of induced fission, (n, γ) and (n, n')	11
2.3	Neutron spectrum of Pu-240 spontaneous and Pu-239 induced fission	12
2.4	Neutron multiplicity distributions for spontaneous and induced fission	13
2.5	Energy dependence of mean number of neutrons emitted by ind. fission	13
2.6	Plutonium metal neutron multiplicity measurement	16
3.1	Cross-section of the ${}^3\text{He}(n, p){}^3\text{H}$ reaction	24
3.2	The PSMC	25
3.3	“PM1” sample	28
3.4	“PERLAPuO ₂ 10” sample	28
3.5	“CBNM 61” sample	28
4.1	Derived and meas. total thermal and nuclear polyethylene cross-section	32
5.1	Spectrum of Pu-239 induced fission and of a 1000 g Pu metal sphere	44
5.2	Neutron flux density of the 1000 g solid sphere	50
5.3	Neutron flux density of the 6000 g hollow sphere	50
5.4	$P(r)$ and $A(r)$ for the 1000 g solid sphere and the 6000 g hollow sphere	51
5.5	1000 g solid sphere divided into 5 hollow spheres of equal mass	52
5.6	$N(r)$ of the 1000 g solid sphere and the 6000 g hollow sphere	53
5.7	Neutron generation probabilities	53
5.8	Multiplication as a function of spontaneous fission source radius	54
5.9	flux density isolines for a point neutron source in a 6000 g hollow sphere	55
5.10	$f(M)$ for the 1000 g solid sphere and the 6000 g hollow sphere	60
5.11	g_2 as a function of fissile mass for a range of simulations	63
5.12	g_2 as a function of the thickness for a range of simulations	64
5.13	M as a function of the thickness for a range of simulations	65
5.14	g_2 as a function of M for a range of simulations	68
5.15	Neutron flux density of the reflected 1000 g solid sphere	71

5.16	Neutron flux density of the reflected 6000 g hollow sphere	71
5.17	Energy distribution of neutrons at different positions	72
5.18	$P(r)$ and $A(r)$ for the reflected spheres	73
5.19	M as a function of radius for the reflected spheres	74
C.1	Frequency spectrum for the polyethylene chain	100
E.1	g_3 as a function of fissile mass for a range of simulations	104
E.2	g_4 as a function of fissile mass for a range of simulations	104
E.3	g_5 as a function of fissile mass for a range of simulations	105
E.4	g_3 as a function of thickness for a range of simulations	105
E.5	g_4 as a function of thickness for a range of simulations	106
E.6	g_5 as a function of thickness for a range of simulations	106
E.7	g_3 as a function of M for a range of simulations	107
E.8	g_4 as a function of M for a range of simulations	107
E.9	g_5 as a function of M for a range of simulations	108

List of Tables

3.1	Characteristics of the PSMC	26
3.2	Characteristics of measured samples	27
3.3	PSMC measurement results	27
4.1	Comparison of measured and simulated S , D and T rates	33
4.3	Description and estimation of systematic uncertainties	35
4.4	Deviations between theoretical and experimental stat. uncertainties	38
5.1	Multiplicity analysis results for two simulations	46
5.2	Multiplicity analysis results of MCNPX-PoliMi simulations	49
5.3	M and g_n based on MCNPX-PoliMi simulations	59
5.4	Results of the corrected multiplicity analysis	60
5.5	Characterization and simulated values of oxide sample (solid sphere)	66
5.6	g_n for different isotopic compositions	66
5.7	Multiplicity analysis results using the $r_{in} = 2.0$ cm reference data	67
5.8	Parameters for fit function	68
5.9	Multiplicity analysis results using the reference curves $g_n(M)$	69
5.10	M and g_n based on MCNPX-PoliMi simulations	74
5.11	Multiplicity analysis results with correct and unreflected g_n	75
B.1	Characteristics of measured metal samples	95
B.2	Characteristics of measured oxide samples	96
B.3	Comparison of measured to simulated S , D and T	97

List of Frequently Used Symbols

α	ratio of (α, n) to spontaneous fission neutrons
α_{mult}	ratio of (α, n) to spontaneous fission neutrons from the simulated multiplicity analysis, based on the point model
α_{true}	true simulated ratio of (α, n) to spontaneous fission neutrons
ν_n	factorial moments of the superfission multiplicity distribution
ν_{in}	factorial moments of the neutron multiplicity distribution for induced fission, averaged over the specific spectrum of a sample
ν_{sfn}	factorial moments of the spontaneous fission multiplicity distribution
r_n	factorial moments of $r(i)$
ϵ	neutron detection efficiency
$\Phi(E, \vec{r})$	neutron flux density
ρ	material density
$\sigma(E)$	cross-section
$\sigma^2(M)$	second central moment, or variance, of $M(r)$
$\sigma^3(M)$	third central moment of $M(r)$
τ	neutron detector die-away time

$A(\vec{r})$	neutron absorption rate per volume
D	Doubles rate
d	thickness of hollow sphere shell
F	spontaneous fission rate
f_d	ratio of Doubles counted within a finite gate length to Doubles counted with an infinite gate length
f_t	ratio of Triples counted within a finite gate length to Triples counted with an infinite gate length
G	gate length
M	net leakage multiplication
M_{corr}	multiplication from the simulated corrected multiplicity analysis
M_{mult}	multiplication from the simulated multiplicity analysis, based on the point model
$m_{Pu,corr}$	total plutonium mass from the simulated corrected multiplicity analysis
$m_{Pu,mult}$	total plutonium mass from the simulated multiplicity analysis, based on the point model
$m_{Pu,true}$	true simulated total plutonium mass
m_{Pu}	total plutonium mass
M_{true}	true simulated multiplication (direct result of MCNPX-PoliMi simulations)
$N(\vec{r})$	net neutron production
N_α	neutron emission rate due to (α, n) reactions
N_{prod}	net number of neutrons produced in the entire volume
p	probability that a neutron induces fission
$P(\vec{r})$	neutron production rate per volume

PD predelay

$r(i)$ probability distribution of counting i correlated neutrons after a trigger

r_{in} inner radius of a hollow sphere

r_{out} outer sphere radius

R_{xxx} isotopic mass fraction of plutonium isotope xxx

S Singles rate

T Triples rate

$W(E)$ neutron energy spectrum

Chapter 1

Introduction

Nowadays, verification of nuclear arms control refers to the verification of delivery vehicles. This is the case for instance in the New START Treaty between Russia and the United States [1]. Warheads are counted indirectly via the delivery vehicles they are associated with. Once a warhead leaves the delivery vehicle, it is not considered any further in the verification regime. It could, however, be deployed again at any time.

Going beyond deployed warheads that are verified nowadays between the US and Russia, the total inventory also includes undeployed warheads and warhead components¹ at various locations as well as those in transport or under maintenance [2, p. 21]. Individual warheads rotate between all these statuses. To prevent re-deployment, irreversible nuclear disarmament requires the dismantlement of warheads. In this case, they are transported to the dismantlement facility, where they are physically taken apart. This results in non-nuclear components and the fissile material in form of the warhead components. To ensure the irreversibility of disarmament, the fissile material from the warhead components must be retrieved and then disposed or converted to exclusively civil purposes. Otherwise, components could be used to build new warheads.

Regarding the longer-term future of nuclear arms control and disarmament, there seems to be fairly broad agreement that verification must become more intrusive and

¹For the purpose of this dissertation, the term “warhead component” refers to that part of a nuclear warhead that contains the fissile material.

that the above-mentioned inventories and processes must be directly verified. This would allow states to know the number of existing warheads and to understand the complete nuclear armament potential. After having made declarations at the entry into force of an agreement and having established a baseline inventory of their nuclear warheads and warhead components, states would allow others to verify that the declarations are accurate. After the baseline has been established, inventory changes must be declared and verified. This includes in particular the verified dismantlement of nuclear warheads. In addition, verification of fissile material production and stocks is required to have confidence that new warheads are not produced and that the fissile material obtained from the dismantlement process is not re-used in warheads. Such verification provisions are relevant for a Fissile Material (Cutoff) Treaty. Fissile material verification is, however, out of the scope of this dissertation which focuses on the verification of warheads and warhead components.²

In order to truly understand the importance of warhead verification, it must be further elaborated: The confidence provided from declaring and verifying nuclear warhead and warhead component inventories as well as dismantlement of warheads could play a key role in maintaining security and stability. This is likely required for potential parties to engage in a process of deep reductions: It is unlikely that deep cuts in U.S. and Russian nuclear arsenals, as well as those of all other states possessing nuclear weapons, will become possible until all have high confidence that agreed-to drawdowns are occurring on a mutual and reciprocal basis. Currently, minor levels of uncertainties may be permissible: Reductions have left arsenals large enough that cheating on a minor scale will not have dramatic effects on stability due to the sufficient size of the remaining arsenal. Furthermore, nuclear weapon states may believe that their current nuclear doctrines deter from complete circumvention of agreements. In the future, if all states come to embrace the policy of a world free of nuclear weapons and take further steps toward that goal, numbers of warheads will eventually be reduced to levels where the remaining arsenals are small, accordingly minor cheating may effect the perceived stability. Due to reduced capabilities, current deterrence doctrines need to be changed to forms that may be perceived to be less effective. This will probably only be possible if the parties are confident that their counterparts have also reduced their capabilities accordingly. Cheating would be a much larger concern making it likely that no further reductions would be undertaken without a path to highly effective verification.

²Further information on a Fissile Material (Cutoff) Treaty and its verification can be found in [3].

Article VI of the Non-Proliferation Treaty *inter alia* calls for pursuing negotiations in good faith “on a treaty on general and complete disarmament under strict and effective international control.” Some non-nuclear weapon states have been quite vocal in their expectation of greater progress. In the very extreme, they might decide not to comply with the Non-Proliferation Treaty as the result of perceived noncompliance of Article VI by nuclear weapon states. As disarmament can only be verified comprehensively by including warheads and their dismantlement in the regime, this appears to be a requirement in order to enable “strict and effective international control” as demanded by Article VI. The language also strongly suggests that non-nuclear weapon states should be involved in a verification regime. By appropriate verification measures, nuclear weapon states could demonstrate compliance with disarmament commitments to the international community. Furthermore, if states possessing nuclear weapons outside the Non-Proliferation Treaty decided to reduce their arsenals, according verification could significantly increase the confidence of the international community, including other states in the region.

From a global perspective, it is the responsibility of the US and Russia to commence with the process of serious reductions due to their vast nuclear arsenals. In view of a world without nuclear weapons, all other states possessing nuclear weapons must reduce as well at some point. While bilateral US-Russian agreements may continue to be a basis for disarmament, future agreements will eventually need to include the five nuclear weapon states recognized by the Non-Proliferation Treaty and also the states outside the Treaty. Then, it seems clear that all these states must be included in the corresponding verification activities. Besides the Treaty’s Article VI requirement, directly including non-nuclear weapon states in verification activities is the most efficient and possibly the only feasible way for non-nuclear weapon states to obtain confidence in reductions. Due to its expertise from verification of nonproliferation obligations, the International Atomic Energy Agency may be a possible actor in this regard. In this case, special challenges must be taken into account: The Non-Proliferation Treaty prohibits nuclear weapon states from “in any way” assisting, encouraging or inducing “any non-nuclear-weapon state to manufacture or otherwise acquire nuclear weapons” while non-nuclear weapon states promise not to manufacture nuclear weapons. In effect, the Treaty might therefore place some fairly strict constraints on verification activities involving direct inspections of nuclear warheads as inspectors might obtain information on how to build them. To enable multilateral verification including non-nuclear weapon states, the specific challenges must be understood and resolved.

Whatever parties will be involved in verification, there are three overarching technical requirements for the task of verifying inventory declarations and warhead dismantlement:

- Each warhead and warhead component needs to be uniquely identified so that it is never counted twice, substituted with a fake, and can be tracked within a high security environment. Two different ways to securely identify a warhead or warhead component are to record an intrinsic signature of the item similar to a fingerprint or to attach a tamper-resistant tag to it.
- A Continuity of Knowledge of the inventoried warheads and warhead components must be maintained at all times, including during their eventual dismantlement. This means keeping continuous track of the warheads and warhead components in the form of an uninterrupted thread of evidence over time. Applicable techniques are containment and surveillance measures such as cameras or seals.
- An item declared to be a warhead or warhead component must be authenticated which means that verification measures must confirm its identity as warhead or warhead component. This dissertation focuses on this requirement.

1.1 Information Barriers

States declaring their nuclear arsenals will very likely not allow inspections that reveal information of their warheads or warhead components which they consider sensitive. The Non-Proliferation Treaty sets boundaries when verification involves non-nuclear weapon state participants. However, due to reasons of national security, nuclear weapon state participants may not have access to significantly more information [2, p. 38]. Assuming a case where verification measures are decided upon in a cooperative manner, mutual agreement on warhead authentication activities can only be reached in the case where nuclear-armed states are confident that their sensitive information is not at stake. The inspecting party – whose interest is to gain maximum confidence on the true nature of a declared warhead – would likely prefer rather intrusive and comprehensive authentication measures. The goal is to create a warhead authentication system which builds confidence while preventing

unacceptable levels of intrusion that could leak information the inspected state is unwilling or legally not allowed to share. This intuitively appears to be somewhat contradictory.

A solution would be to take potentially intrusive measurements containing sensitive information, but to automatically process the measurement information via an algorithm so that the only output visible to the inspector would be of non-sensitive nature (e.g. a green, yellow or red light indicating “specified warhead”, “inconclusive measurement” or “not specified warhead”). Preventing the leakage of sensitive information would be the task of a so-called information barrier.

Two types of authentication systems are frequently discussed. The template type uses the unique radiation spectrum or other measurable signatures of a previously authenticated item to compare it to the signature of the item under consideration. When the signatures match, the item is successfully authenticated as long as there is sufficient confidence that the reference signature comes from a correctly authenticated item. This dissertation focuses on the other type, the attribute approach: The inspected party would declare attributes that characterize the warhead or warhead component to be authenticated. It is essential that attributes do not deliver sensitive information. For obtaining maximum confidence, the attributes should be chosen in a way to minimize the possibility of cheating, so that other items will not fulfill all attributes, but that the authenticated items will. This idealistic concept might not hold in reality: There might be false positives and false negatives. The challenge will then be to define attributes and analysis algorithms in such a way that the analysis results in reasonable confidence, i.e. to minimize the probabilities of false results. The definition of the level of confidence deemed necessary is a political task. An attribute information barrier only analyzes whether the item under investigation meets the defined attributes; the value of an information barrier then depends on the attribute definitions and algorithms as well as on the quality of the measurement techniques.

Attributes might be of qualitative or quantitative nature. Attributes based on quantitative thresholds provide the benefit that it is not necessary to declare the actual values which might be sensitive. If these thresholds deviate too much from the actual values, however, other items might also satisfy them. This would reduce the confidence that could be gained from such attributes. The following list contains examples of published attributes for plutonium-based warheads and warhead components [4]:

- Presence of plutonium
- Plutonium ratio Pu-240/Pu-239
- Plutonium mass threshold

1.2 Measurement Issues

A high reliability of attribute measurement techniques is required as inspectors cannot review and analyze detailed measurement results, if they are in doubt for whatever reasons. In contrast to other situations where radioactive samples are characterized, the knowledge that exists prior to the measurements, for example the sample's geometry, may be inadequate. Many measurement techniques require certain information on a sample to function accurately. For example, the detector calibration may need to be performed using calibration sources that are similar to the samples measured afterwards. Due to the lack of knowledge, the measurement system should be chosen which requires a minimum amount of assumptions regarding the nature of the item for delivering accurate results. Reducing the dependency of measurements on geometry could allow more meaningful attribute thresholds as close as possible to the real values to increase the confidence gained from such a system.

The potential undeclared presence of materials between warhead component and detector is part of this issue. In the case of fully assembled warheads, materials such as a conventional explosive surround the fissile component. Furthermore, most nuclear warheads are stored in containers for safety reasons [2, p. 33]. Warhead components may also be stored in containers [2, p. 33]. Such issues could have an impact on the measurement and therefore on the output of the attribute analysis.

Inspectors must understand how large deviations between real and measured values (bias) become as the properties of the item and intervening materials vary in plausible manners. Then they can assess the reliability of specific measurement methods and attribute analyses when it is impossible to obtain further information on the item.

1.3 Research Task and Methodology

A promising attribute measurement system is a combination of gamma spectroscopy and neutron multiplicity counting. Gamma spectroscopy could determine the isotopic composition of a sample, specifically the plutonium isotope ratio. Once the isotopic composition is known, neutron multiplicity counting could potentially deduce the fissile mass from measuring the rate of neutrons from spontaneous fission. Both measurement techniques are frequently used in the context of Safeguards and nuclear security. In most cases, sufficient knowledge exists regarding the configuration of the samples to be measured and bias is usually small. Furthermore, neutron multiplicity counting has been used for research for verifying warhead dismantlement. The major projects in this regards are the Trilateral Initiative, the Fissile Material Transparency Technology Demonstration and the Attribute Verification with Neutrons and Gamma Rays project, which were all engagements of nuclear weapon states.³ All three initiatives concluded that their neutron multiplicity counting systems functioned successfully [5, 6, 7].

While all three research projects significantly advanced the technical discussion of verified warhead dismantlement, their publications do not detail potential issues and limitations of neutron multiplicity counting. The technical research to date has focused on preventing measurement systems to release sensitive information. In general, there is very little research investigating proposed systems in regard to reducing false assessments, which is the main requirement of the inspecting party. The lack and need of such research is expressed in [2, pp. 32]. As it is essential for an inspecting party to trust the functionality of a system, this dissertation presents research on sources of bias in neutron multiplicity counting. As warheads and warhead components have much larger masses and volumes compared to those samples which are frequently assayed nowadays, it is specifically examined whether there is a bias when measuring samples with large masses. Furthermore, it is investigated how bias depends on the sample configuration in order to assess the reliability of neutron multiplicity counting when the configuration remains unknown. The aim of this dissertation is to reduce bias and thereby increase the reliability of neutron multiplicity counting measurements.

The methodology of the research is a combination of neutron multiplicity measurements of plutonium samples and Monte-Carlo simulations. Measurements can be

³In the Trilateral Initiative, the International Atomic Energy Agency was involved as well.

used to test whether the simulation code is capable of accurately performing neutron multiplicity counting analyses by comparing its results to the measurement data. The simulations are required as a much larger variety of plutonium samples not available for measurements needs to be examined.

Chapter 2 begins with the description of relevant neutron sources and interactions to allow an understanding of the subsequent description of how the neutron multiplicity counting technique works. The purpose of the overall chapter is to lay the physical foundation of the dissertation. Chapter 3 describes neutron multiplicity measurements of plutonium samples. Chapter 4 introduces the simulation code and compares simulation results to the measurement results. It is explained which data must be implemented for the code to reproduce the measurement results with reasonable accuracy. By discussing the simulation capacity, this chapter serves as the legitimization to base further results on simulations. Chapter 5 contains the analysis of potential bias: First, it discusses bias for such plutonium configurations which are suited to study effects in warhead components without any further materials between plutonium and detector. The aim is to reduce bias for such samples. Then, it discusses plutonium configurations surrounded by further materials where physical effects are expected that would similarly occur in warheads and warhead components placed in containers. Chapter 6 summarizes the main research results and discusses their implications for verified warhead inventories and warhead dismantlement.

Chapter 2

Neutron Multiplicity Counting

2.1 Neutron Sources and Interactions

Fissile materials emit neutrons that can be detected. Those neutron sources and interactions with relevance for this dissertation are introduced in this section. Besides spontaneous fission, induced fission is a primary source of neutrons. Furthermore, (α, n) and (n, γ) reactions and elastic scattering of neutrons are discussed.

2.1.1 Spontaneous and induced fission

The basics of spontaneous fission can be understood from the Bethe-Weizsäcker mass formula [8, 9]. It includes the pairing term which explains the large difference of spontaneous fission yields of plutonium isotopes: Pu-239 has a spontaneous fission rate of 0.007 ± 0.001 fissions/s-g, whereas Pu-240 has 479.1 ± 5.3 fissions/s-g [10, 11]¹. As there is a difference of 5 orders of magnitude, spontaneous fission by Pu-239 can be neglected for the purpose of this dissertation. Cf-252 is another isotope that decays by spontaneous fission at a rate of $6.136 \cdot 10^{11} \pm 2 \cdot 10^9$ fissions/s-g [10]. While isotopes with odd neutron and even proton numbers have low spontaneous fission yields, they can be fissioned by inducing thermal neutrons which have energies

¹For Pu-240, the uncertainty corresponds to the standard deviation of different measurements summarized in [11], which seems more appropriate than listing the much smaller statistical uncertainties.

around 0.025 eV : By capturing a thermal neutron, a compound nucleus with an even number of neutrons is formed which is in an excited state due to the release of the neutron's binding energy. Due to the pairing term, this energy is larger compared to a compound nucleus with an uneven number of neutrons and an even number of protons. For Pu-239 induced fission, the excitation energy is larger than the fission threshold. Even-even isotopes, however, require fast neutrons as additional kinetic energy is required to sufficiently excite the compound nucleus to overcome the fission threshold. Fig. 2.1 and 2.2 show the induced fission cross-sections of Pu-239 and Pu-240. While the Pu-239 induced fission cross-section for 0.025 eV neutrons is 748 b , for Pu-240 it is 0.06 b . At 2 MeV , the cross-sections are similar (2.0 b for Pu-239 and 1.7 b for Pu-240) [10].²

The fission neutron energy spectra can be derived from evaporation theory (which expresses the de-excitation process of the fission fragments as the loss of heat energy by the removal of particles), see [13]. It can be expressed by the Watt spectrum³ [14]

$$W_{fission}(E) = \frac{\exp(-E/a) \sinh(\sqrt{bE})}{\int_0^\infty \exp(-E/a) \sinh(\sqrt{bE}) dE} \quad (2.1)$$

where E is the energy of the emitted neutron, a and b are parameters specific to the nuclide and the nature of the reaction, for example given in [15, page H-1]. The spectra displayed in Fig. 2.3 show that the energy distribution of neutrons emitted from spontaneous fission of Pu-240 and induced fission of Pu-239 are very similar.

A fission process usually releases more than one neutron. The number of neutrons emitted in spontaneous or induced fission is called neutron multiplicity.⁴ It can be shown that this distribution can be approximated by a Gaussian function [16]. The multiplicity distributions of spontaneous fission of Pu-240 and Cf-252 are published in [17]. Distributions for Pu-239 induced fission are published in [18], examples

²A more detailed explanation of the spectra and the fission process in general is omitted in this dissertation in order to keep the focus on neutron multiplicity counting. For a precise understanding of spontaneous and induced fission, including the physics of the different energy regions of the spectra, Fabio Zeiser covers this issue in his Bachelor thesis [12].

³A more detailed explanation of the evaporation theory and applied corrections including the Watt spectrum is omitted in this dissertation, but is covered in Fabio Zeiser's Bachelor thesis [12].

⁴The physics behind the neutron multiplicity distributions are presented in a concise manner here. Fabio Zeiser covers them in more detail in his Bachelor thesis [12].

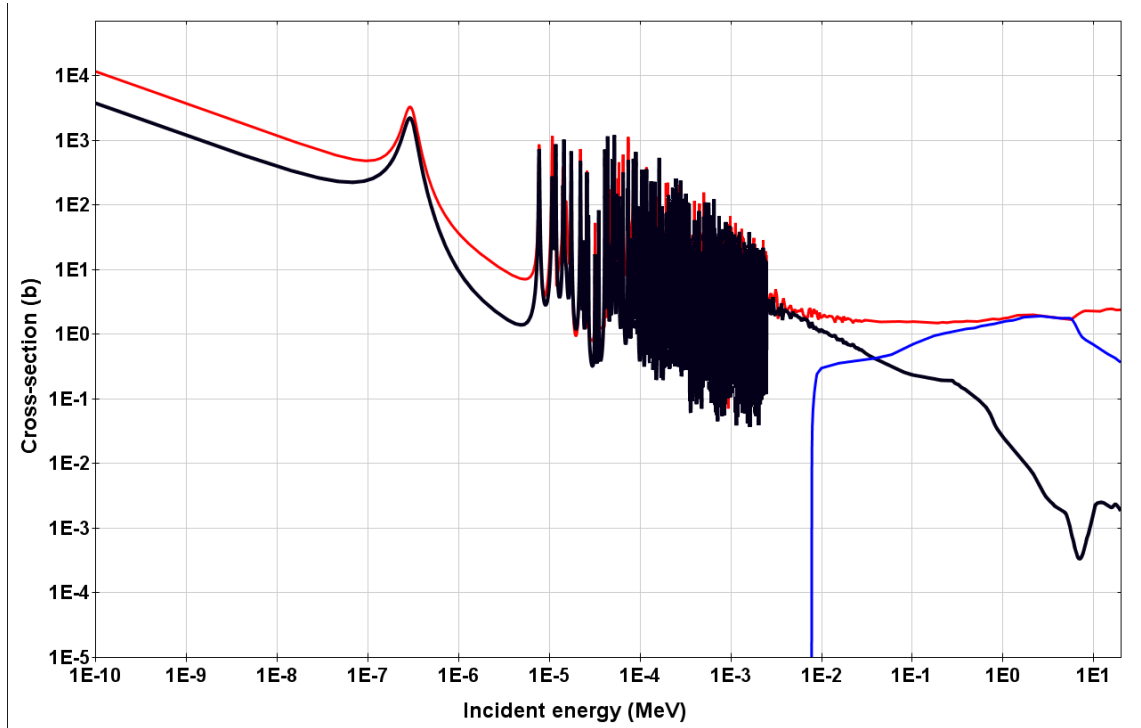


Figure 2.1: Pu-239 cross-sections of induced fission (red), (n, γ) (black) and (n, n') reactions (blue) [10]

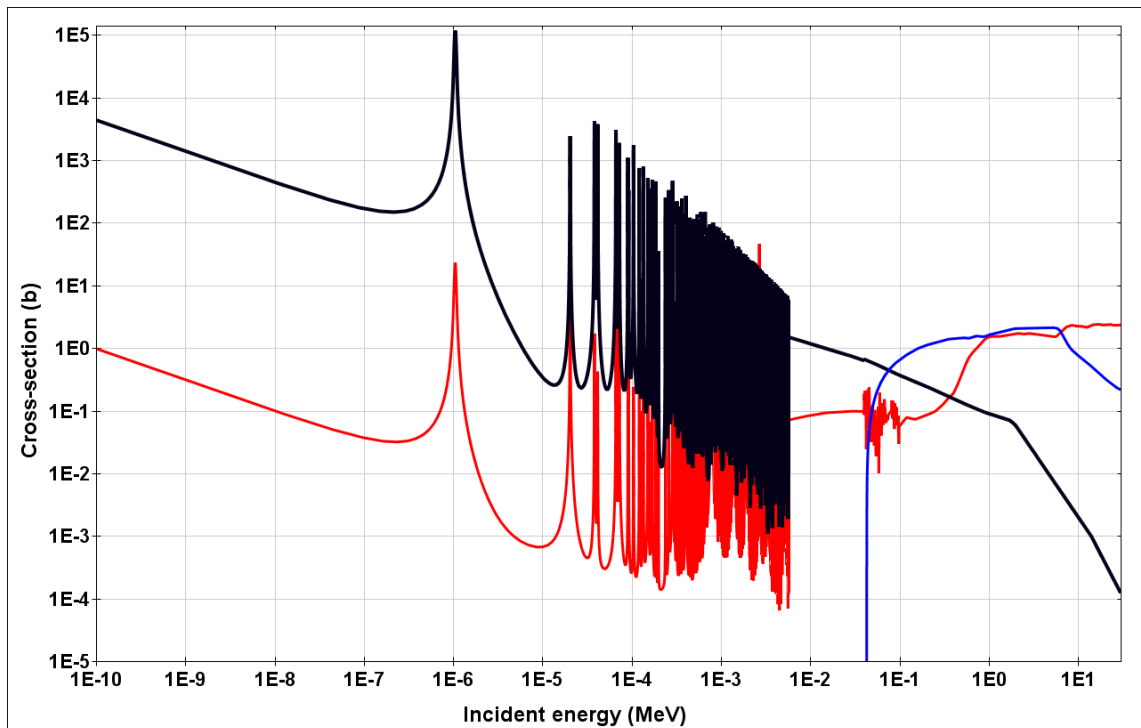


Figure 2.2: Pu-240 cross-sections of induced fission (red), (n, γ) (black) and (n, n') reactions (blue) [10]

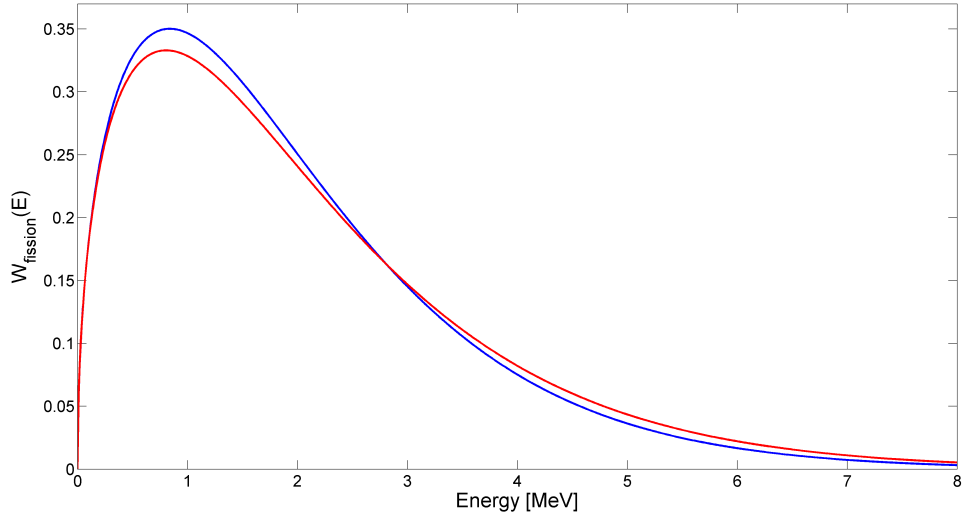


Figure 2.3: Energy spectrum of neutrons emitted from spontaneous fission of Pu-240 (blue) and induced fission of Pu-239 (red)

are shown in Fig. 2.4, all data are based on measurements. One can see that the induced fission multiplicity distributions depend on the energy of the absorbed neutrons. With increasing energy of the absorbed neutron, the mean number of emitted neutrons increase as the kinetic energy of the absorbed neutron must be transferred, see Fig. 2.5. Also the standard deviation of the Gaussian probability density function grows with increasing neutron energy [18].

2.1.2 Further interactions

Besides induced fission, there are further neutron absorption reactions. Examples are the (n, γ) reaction, neutral reactions such as $(n, 2n)$ or charged reactions such as (n, p) or (n, α) . Of these absorption reactions, (n, γ) is the dominant process for plutonium. The cross-sections are shown in Fig. 2.1 and 2.2. The (n, γ) reaction is relevant at thermal energies compared to induced fission. Averaged over the fission neutron energy spectrum for Pu-239, however, its cross-section is two orders of magnitude lower than that of induced fission. For Pu-240, the difference is smaller.

In an inelastic neutron scattering process, denoted by (n, n') , the neutron transfers energy to the nucleus which reaches an excited state which eventually decays by the emission of γ radiation [19, p. 360]. Thereby, the neutron is slowed down and changes its direction. Fig. 2.1 and 2.2 show the cross-sections of inelastic scattering.

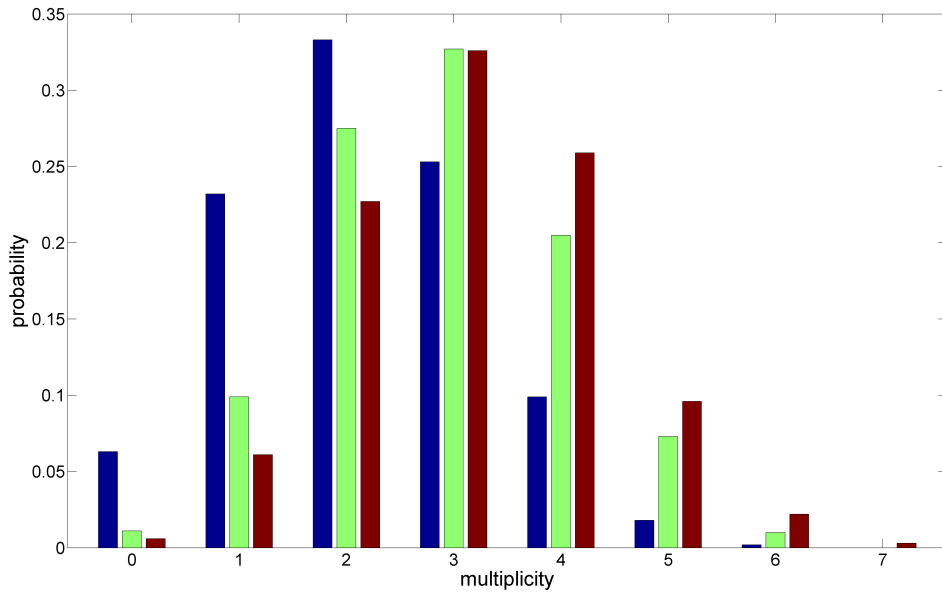


Figure 2.4: Neutron multiplicity distributions for spontaneous fission of Pu-240 (blue), induced fission of Pu-239 by thermal neutrons (green) and by 2 MeV neutrons (brown)

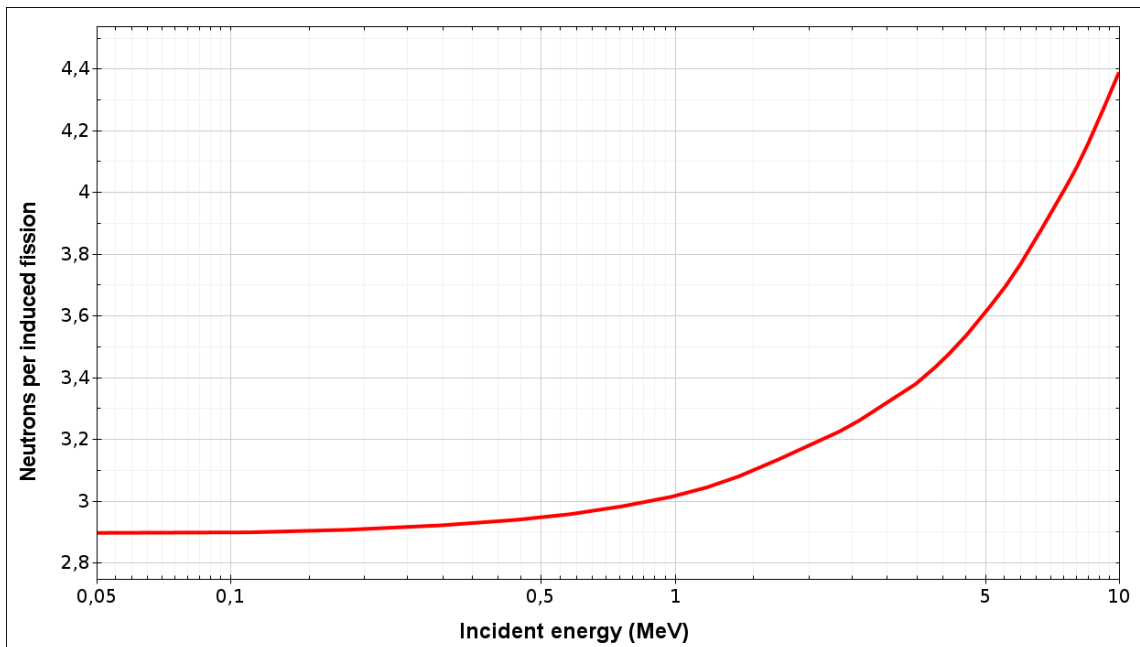


Figure 2.5: Mean number of neutron emitted by induced fission of Pu-239 as a function of the energy of the absorbed neutron [10]

Below a certain neutron energy threshold, inelastic scattering is impossible as neutrons must at least carry enough energy to excite the nucleus to its first excited state. For neutrons having higher energies, the nucleus can be excited to further states. The cross-sections are comparable to induced fission cross-sections for Pu-239 and Pu-240 for neutron energies above 100 *keV*.

In addition to the inelastic reactions, elastic scattering of neutrons takes place. Elastic scattering also slows neutrons down and changes their direction. The average energy loss of the neutrons is given as $\overline{\Delta E} = 2E \cdot A / ((A + 1)^2)$ where A is the mass number of the nucleus [19, p. 360]. Therefore, elastic scattering is much less relevant for elements with a large than for elements with a low mass number (for Pu-239 the average neutron energy loss is 0.8%, for C-12 it is 14.2%, for H-1 it is 50%). In appropriate media, fast neutrons can be moderated to lower (e.g. thermal) energies by multiple elastic scattering.

As the last important aspect, plutonium mainly decays by the emission of α particles. The energies of the α particles from Pu-239 and Pu-240 are in the range of 4 – 5.2 *MeV* [10]. For such energies, (α, n) reactions can take place in certain light isotopes, among them O-17 and O-18 [19, p. 347]. The (α, n) neutron yields are 39.7 ± 1.1 n/s-g for $^{239}\text{PuO}_2$ and 146 ± 4 n/s-g for $^{240}\text{PuO}_2$ with natural oxygen isotope abundances [20].⁵ These reactions may occur to a much lesser extent also in plutonium metals with oxide impurities.

2.2 Detection

In the context of nonproliferation, arms control and nuclear security, neutron detectors are mainly used to count neutrons as opposed to spectroscopy. In contrast to total neutron counting, however, more information can be obtained by performing coincidence measurements. In particular, the spontaneous fission rate can be obtained from which the Pu-240 mass can be determined. When the isotopic composition of a sample is known, e.g. through gamma spectroscopy, the total plutonium mass can be calculated. This section introduces how neutron detection and coincidence measurements work in general. The subsequent section then introduces the mathematics required to deduce the plutonium mass.

⁵The uncertainties are the standard deviations of different measurements summarized in [11], which seems more appropriate than listing the much smaller statistical uncertainties.

No detector registers all neutrons emitted by a sample. Throughout the dissertation, the detection efficiency ϵ is defined as the ratio of detected neutrons to neutrons leaving the fissile material. Depending on the geometry of the detector and the location of the neutron source, not all emitted neutrons necessarily reach it. ϵ is further reduced as not all neutrons that reach the detector are necessarily detected. Accordingly, ϵ also depends on the specific detection mechanism. An example is neutron detection by neutron capture in the detector. In this case, ϵ depends specifically on the capture cross-section of the detector material.

Neutron detectors can be operated to perform coincidence measurements with gates. A method to deduce the Pu-240 mass requires two types of gates: A neutron detection event triggers the Reals+Accidentals (R+A) gate which is opened after a short predelay PD and remain open during the gate length G .⁶ All detected neutrons open a R+A gate, whether another gate is already open or not. The other type of gate, the Accidentals (A) gate, is randomly triggered. For a purely random neutron pulse stream, the two gates would deliver the same results within the statistical uncertainty. If, however, correlated neutrons from fission are present, the number of neutrons measured in the R+A gate would be higher than in the A gate. Fig. 2.6 shows the result of a plutonium metal neutron multiplicity measurement (12.5 g, 95.4% Pu-239, 4.5% Pu-240) performed at the Joint Research Centre in Ispra, Italy.⁷ The abscissa shows the number of neutrons falling into a gate; the ordinate shows the rate of these gates. For the R+A gate, multiplicity 0 means that a neutron triggered a gate. The appropriate gate length can be determined based on the estimated neutron travel time between its emission and the detection [21, pp. 69]. The probability distribution of the travel time $f(t)$ can be approximated by an exponential function with the die-away time τ [22]

$$f(t) \approx \frac{1}{\tau} e^{-t/\tau} \quad (2.2)$$

2.3 Basis of Neutron Multiplicity Counting

In this section, it is shown how information can be retrieved from the R+A and A gates. The neutron flux emitted by a fissile sample is affected by a number of unknown properties:

⁶The predelay is required due to electronic effects in the detector, as explained in [21, page 33]

⁷The He-3 based Passive Scrap Multiplicity Counter has been used to perform the measurement, see section 3.1.

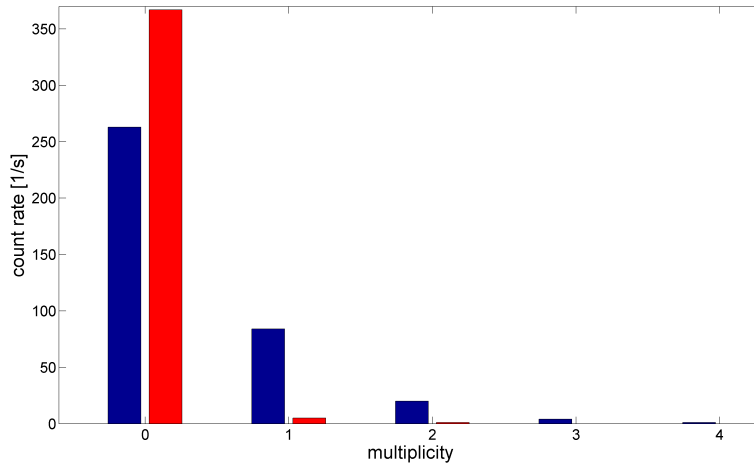


Figure 2.6: Plutonium metal neutron multiplicity measurement with the R+A gate (blue) and A gate (red) distributions (12.5 g, 95.4% Pu-239, 4.5% Pu-240)

- Total spontaneous fission rate
- Neutron multiplication, in particular by induced fission of Pu-239
- (α, n) reaction rate if oxides or certain other light isotopes are present

This multiplicity distribution of detected neutrons can be expressed in terms of its moments. They can be related to the moments of the multiplicity distribution of neutrons emitted by the plutonium sample, i.e. by spontaneous and induced fission as well as the (α, n) reactions. The legitimization to describe the neutrons from all the emission processes in a single multiplicity distribution is the “superfission model”. It defines spontaneous fission and (α, n) as a primary neutron source. Then, it assumes that all induced fission neutrons are emitted simultaneously with the primary spontaneous fission or (α, n) reaction. With this model, the moments of this distribution can be analytically described as functions of the unknown properties. Accordingly, with neutron multiplicity counting the three unknown properties can be assessed. The mathematical formalism is described in the following.⁸

⁸The most widely cited derivation by Ensslin et al. [21] contains minor ambiguities, as was pointed out by Pázsit et al. in [23]. While Pázsit et al. rightly point out parts of the issue, they did not clarify all ambiguities, which is done here. Publications by Hage, Cifarelli and Dierckx [24, 25, 26] each describe parts of the derivation, but do so in a very complex manner. The derivation in [21] is simpler, therefore it is generally followed here.

2.3.1 Description of neutron source

Let $P_{sf}(\nu)$ be the probability distribution of the number of neutrons ν emitted during a spontaneous fission process. The first moment of this distribution is $\boldsymbol{\nu}_{sf1}$ which is equal to the average number of neutrons emitted per fission.⁹ Let F be the spontaneous fission reaction rate and N_{sf} the spontaneous fission neutron rate. If the total neutron emission rate due to (α, n) reactions is N_α , the ratio of (α, n) reaction neutrons to spontaneous fission neutrons is

$$\alpha = \frac{N_\alpha}{N_{sf}} = \frac{N_\alpha}{F \cdot \boldsymbol{\nu}_{sf1}} \quad (2.3)$$

Thus, the total reaction rate of the primary source can be expressed as

$$R_s = F + N_\alpha = F(1 + \alpha \cdot \boldsymbol{\nu}_{sf1}) \quad (2.4)$$

where the subscript s refers to “source”. The multiplicity distribution of the neutrons emitted by spontaneous fission and (α, n) reactions is [27]

$$P_s(\nu) = \frac{F}{R_s} P_{sf}(\nu) + \frac{N_\alpha}{R_s} \delta_{1\nu} \quad (2.5)$$

where δ_{ij} is the Kronecker symbol. Neutrons that are emitted from spontaneous fission or (α, n) reactions may leak the sample, be absorbed or induce fission. These processes can be described as multiplying the number of primary neutrons from spontaneous fission and (α, n) reactions. In reactor physics, this is described by the multiplication factor k_{eff} , which is the ratio of the number of neutrons produced in one generation to the number either absorbed or leaked in the preceding generation. If absorption and leakage outweigh the number of newly produced neutrons, $k_{eff} < 1$. In this case, the primary neutrons produce additional neutrons, but the neutron population declines with each neutron generation. Instead of k_{eff} , the leakage multiplication M (for brevity this dissertation refers to it as “multiplication”) is used in neutron multiplicity counting. It includes the sum of the neutrons from all generations divided by the number of primary neutrons. The total number of neutrons that eventually leak the sample is smaller than the sum of the generations:

⁹For visual clarity, all moments are written in bold font throughout the dissertation.

As this sum includes neutrons from one generation which were captured or induced fission in a later generation and therefore never leak the sample, these neutrons are subtracted to obtain M . Overall, M is the total number of neutrons that leak a sample as a result of primary neutrons divided by the number of primary neutrons. M is derived in [19, pp. 422]:

$$M = \frac{1 - p}{1 - p\nu_{i1}} \quad (2.6)$$

where p is the probability that a neutron induces fission. Neutron leakage is included in this description; p is accordingly smaller than it would be without neutron leakage. ν_{i1} is the first moment of the multiplicity distribution for induced fission (denoted by subscript i), i.e. the average number of neutrons released per induced fission. Taking the primary neutron source (spontaneous fission and (α, n) reactions) and the neutron multiplication together, one can speak of fission bursts, or “superfission” [27] where the neutrons emitted altogether can be described by a normalized multiplicity distribution $P(\nu)$. A probability distribution such as $P(\nu)$ can be equivalently described by their factorial moments (see proof in [27]) which are defined by

$$\begin{aligned} \sum_{\nu=0}^{\infty} \nu P(\nu) &= \nu_1 \\ \sum_{\nu=0}^{\infty} \nu(\nu - 1)P(\nu) &= \nu_2 \\ \sum_{\nu=0}^{\infty} \nu(\nu - 1)\dots(\nu - n + 1)P(\nu) &= \nu_n \end{aligned} \quad (2.7)$$

$n = 3, 4, \dots$

The reason why factorial moments are used is because the mathematical formalism for neutron multiplicity counting is less cumbersome compared to central moments. The derivation of the factorial moments is covered in Appendix section A.1.¹⁰ The results for the first three factorial moments of the multiplicity distribution of emitted neutrons are [27]:

¹⁰The main text follows all steps of the derivation that appear essential for the understanding of neutron multiplicity counting. Other elements of the derivation are included in this dissertation as well for completeness, but are presented in the Appendix to keep the main text concise.

$$\nu_1 = \frac{M}{1 + \alpha\nu_{sf1}} \nu_{sf1}(1 + \alpha) \quad (2.8)$$

$$\nu_2 = \frac{M^2}{1 + \alpha\nu_{sf1}} \left\{ \nu_{sf2} + \left(\frac{M-1}{\nu_{i1}-1} \right) \nu_{sf1}(1 + \alpha)\nu_{i2} \right\} \quad (2.9)$$

$$\begin{aligned} \nu_3 = & \frac{M^3}{1 + \alpha\nu_{sf1}} \left\{ \nu_{sf3} + \left(\frac{M-1}{\nu_{i1}-1} \right) [3\nu_{sf2}\nu_{i2} + \nu_{sf1}(1 + \alpha)\nu_{i3}] \right. \\ & \left. + 3 \left(\frac{M-1}{\nu_{i1}-1} \right)^2 \nu_{sf1}(1 + \alpha)\nu_{i2}^2 \right\} \end{aligned} \quad (2.10)$$

where ν_{sfn} and ν_{in} are the factorial moments of the spontaneous fission and induced fission multiplicity distributions, respectively.

2.3.2 Extraction of correlated moments from the measurement

Next, it must be considered that neutron detectors have a limited detection efficiency ϵ . Due to $\epsilon < 1$, not all of the emitted neutrons are detected, as discussed in Appendix section A.2. Furthermore, the probability of one of the emitted neutrons triggering a gate and subsequent neutrons being detected within the finite gate length must be considered (see Appendix section A.3). $r(i)$ denotes the probability distribution of counting i correlated neutrons (i.e. from one ‘‘superfission’’) after a trigger. Its factorial moments r_n are derived in Appendix section A.3:

$$r_1 = \frac{\epsilon f_d \cdot \nu_2}{2\nu_1} \quad (2.11)$$

$$r_2 = \frac{\epsilon^2 f_t \cdot \nu_3}{3\nu_1} \quad (2.12)$$

$$\text{where } f_d = e^{-PD/\tau}(1 - e^{-G/\tau}) \quad (2.13)$$

$$f_t = f_d^2 \quad (2.14)$$

where equation 2.14 is true if $f(t)$ can be described by equation 2.2 which usually is a good approximation [19, p. 459]. A physical interpretation of f_d and f_t will be given later. The derivation until this point is correctly performed by Ensslin et al. [21] and is the most frequently cited one. In their further considerations, their description of

the process is somewhat ambiguous. Here, these ambiguities are resolved. So far, it has been assumed that only neutrons from one “superfission” event contribute to the detected neutrons in one gate. In reality, neutrons from different “superfission” events may overlap and are detected in the same gate. They must be considered as background neutrons. In fact, the multiplicity distribution $k(i)$ which is the distribution measured in a gate opened by a trigger event (factorial moments \mathbf{k}_n) consists of the following: First, there are correlated neutrons, i.e. belonging to the same “superfission” event as the trigger neutron with the probability distribution $r(i)$ and its factorial moments \mathbf{r}_n . Second, there are background neutrons which belong to a “superfission” event that is not the same as the one the trigger neutron came from. Background neutrons follow the probability distribution $b(i)$ with its factorial moments \mathbf{b}_n . When measuring one neutron in addition to the trigger, it might either be a correlated or a background neutron. When measuring two neutrons, they might be both correlated neutrons, both background neutrons, or one correlated and one background neutron. In the following, this expression is given in mathematical terms; additionally it can be generalized as shown [24]:

$$k(1) = r(1)b(0) + r(0)b(1); \quad k(2) = r(2)b(0) + r(1)b(1) + r(0)b(2) \quad (2.15)$$

$$k(m) = \sum_{i=0}^m r(m-i)b(i) \quad (2.16)$$

An equivalent expression can be given based on the factorial moments of these probability distributions, as shown in [25, eq. (81)]:

$$\mathbf{k}_n = \sum_{j=0}^n \binom{n}{j} \mathbf{r}_j \mathbf{b}_{n-j} \quad (2.17)$$

This expression can be evaluated for $n = 0$, $n = 1$ and $n = 2$. Recognizing that \mathbf{r}_j and \mathbf{b}_{n-j} are normalized, one obtains

$$\mathbf{r}_1 = \mathbf{k}_1 - \mathbf{b}_1 \quad (2.18)$$

$$\mathbf{r}_2 = \mathbf{k}_2 - \mathbf{b}_2 - 2(\mathbf{k}_1 - \mathbf{b}_1)\mathbf{b}_1 \quad (2.19)$$

With this, one can describe the three central quantities used in neutron multiplicity counting which are the Singles, Doubles and Triples rates S , D and T : The Singles rate is the total detection rate of neutrons. It corresponds to the rate of “superfissions” (equation 2.4) multiplied by the detection efficiency and the average number of neutrons emitted per “superfission”:

$$S = F(1 + \alpha \nu_{sf,1}) \epsilon \nu_1 \quad (2.20)$$

Experimentally, S also corresponds to the number of triggers and therefore the number of opened correlated gates since every detected neutron opens a gate. From equations 2.11, 2.18 and 2.20 one obtains D ; from equations 2.12, 2.19 and 2.20 one obtains T :¹¹

$$D = F(1 + \alpha \nu_{sf,1}) \cdot \frac{\epsilon^2 f_d \cdot \nu_2}{2} = S \cdot r_1 = S \cdot [\mathbf{k}_1 - \mathbf{b}_1] \quad (2.21)$$

$$T = F(1 + \alpha \nu_{sf,1}) \cdot \frac{\epsilon^3 f_t \cdot \nu_3}{6} = \frac{S}{2} \cdot r_2 = \frac{S}{2} [\mathbf{k}_2 - \mathbf{b}_2 - 2(\mathbf{k}_1 - \mathbf{b}_1) \mathbf{b}_1] \quad (2.22)$$

The right side of the equations shows how the rates are extracted experimentally: The multiplicity distribution $k(i)$ and its factorial moments \mathbf{k}_n is the measurement result of the R+A gate, while $b(i)$ and \mathbf{b}_n is the result of the A gate. The equations also reveal the physical meaning of S , D and T : They can be interpreted as the factorial moments of the emitted neutrons (ν_n) multiplied by the rate of “superfissions” ($R_s = F(1 + \alpha \cdot \nu_{sf,1})$) taking the detection process (ϵ , f_d , f_t) into account. f_d and f_t indicate that not all neutrons from one “superfission”, even if they are captured in the detector, fall into the gate as some might be detected after the gate has been closed: It can be shown [22] that f_d and f_t correspond to the fraction of D and T counted in the finite gate compared to an infinitely long one:

$$f_d = \frac{D}{D_\infty} \quad (2.23)$$

$$f_t = \frac{T}{T_\infty} \quad (2.24)$$

Finally, using equations 2.8, 2.9, 2.10, 2.20, 2.21 and 2.22, the equations for S , D

¹¹The factor 1/2 in the Triples rate is introduced as a matter of convention.

and T become

$$S = F\epsilon M\nu_{sf1}(1 + \alpha) \quad (2.25)$$

$$D = \frac{F\epsilon^2 f_d M^2}{2} \left[\nu_{sf2} + \left(\frac{M-1}{\nu_{i1}-1} \right) \nu_{sf1}(1 + \alpha)\nu_{i2} \right] \quad (2.26)$$

$$T = \frac{F\epsilon^3 f_t M^3}{6} \left\{ \nu_{sf3} + \left(\frac{M-1}{\nu_{i1}-1} \right) [3\nu_{sf2}\nu_{i2} + \nu_{sf1}(1 + \alpha)\nu_{i3}] + 3 \left(\frac{M-1}{\nu_{i1}-1} \right)^2 \nu_{sf1}(1 + \alpha)\nu_{i2}^2 \right\} \quad (2.27)$$

2.3.3 Calculating the plutonium fissile mass

With equations 2.25, 2.26 and 2.27, the unknown properties M , F and α can be calculated from the measured S , D and T , as shown in Appendix section A.4. With F , the plutonium effective mass can be calculated:

$$m_{240eff} = \frac{F}{479.1 \text{ fissions}/(s \cdot g)} \quad (2.28)$$

It is the mass of Pu-240 that would give the same response as that obtained from all the even isotopes in the actual sample. m_{240eff} needs to be converted to the actual total plutonium mass m_{Pu} . This calculation can be performed if the isotopic mass fractions R_{238} , R_{240} and R_{242} are known [21].¹²

$$m_{Pu} = \frac{m_{240eff}}{2.52 \cdot R_{238} + R_{240} + 1.68 \cdot R_{242}} \quad (2.29)$$

¹²The constants in the formula are determined from the relative spontaneous fission half-lives and the relative neutron multiplicity distributions [19, p. 457].

Chapter 3

Neutron Multiplicity Measurements of Plutonium Samples

This chapter describes a measurement campaign at the PERLA laboratory, Joint Research Centre, Ispra, from 23 April - 4 Mai 2012. Neutron multiplicity measurements have been conducted with a variety of plutonium samples.

3.1 He-3 Detector

Detectors commonly used in the context of nonproliferation, arms control and nuclear security are based on He-3. There is a growing range of alternatives, see for example [28]. While the author has also published a feasibility analysis of using other detectors in the field of warhead authentication [29], this dissertation is limited to He-3 detectors as it has clear advantages. Though being aware of the need of He-3 replacement technologies as the availability of He-3 has become very limited, existing He-3 systems remain available. Therefore, they could still be used for warhead and warhead component authentication, given the importance of the task.

The main advantage of He-3 detectors is their large neutron detection efficiency ϵ . It is due to the large cross-section of the detection reaction ${}^3\text{He}(n,p){}^3\text{H}$ at thermal neutron energies (see Fig. 3.1) . The ${}^3\text{He}(n,p){}^3\text{H}$ reaction releases 765 keV. The proton and triton are charged particles; thus they ionize and excite atoms along their

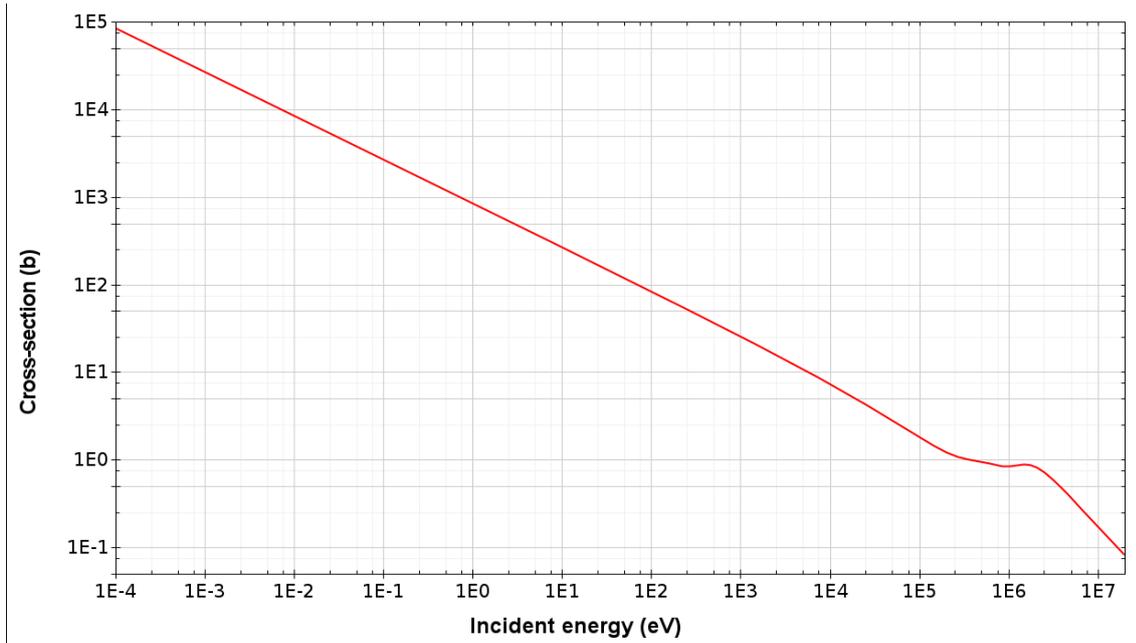


Figure 3.1: Cross-section of the ${}^3\text{He}(n,p){}^3\text{H}$ reaction [10]

way until their energy is exhausted. By applying an electrical potential, the electrons travel towards the anode and the ions towards the cathode which constitutes the detection mechanism. Fig. 3.1 shows the reaction's $1/\sqrt{E}$ dependence. It can be seen that neutrons must be moderated to reach energies where the cross-section is large. For this purpose, He-3 detectors contain high-density polyethylene where neutrons scatter elastically. The He-3 is contained in tubes that are usually arranged in rings, surrounded by polyethylene. With a too small amount of polyethylene, on the one hand, ϵ is below the optimum because neutrons are not ideally moderated. With too much polyethylene, on the other hand, ϵ is also lower than the optimal value because moderated neutrons are captured in the polyethylene which outweighs the positive moderation effect. In particular H-1 has a high thermal neutron capture cross-section. This moderation process has a strong influence on the neutron travel time $f(t)$: The more polyethylene is between the cavity and a specific tube, the longer is the die-away-time ($\tau \approx 50 \mu\text{s}$ for typical He-3 detectors).

Fig. 3.2 shows a specific He-3 detector, the Passive Scrap Multiplicity Counter (PSMC) [30] which has been used to conduct the measurements. The total size of the detector is 661 x 661 x 942 mm with a cylindrical cavity (diameter 20 cm, height 40 cm). The samples are placed in the cavity in the center. The detection efficiency depends on the exact location of the source in the cavity as this influences the neutron flux in the He-3 tubes. An aim of He-3 detector design is to minimize this dependency and achieve an almost constant efficiency at all locations within

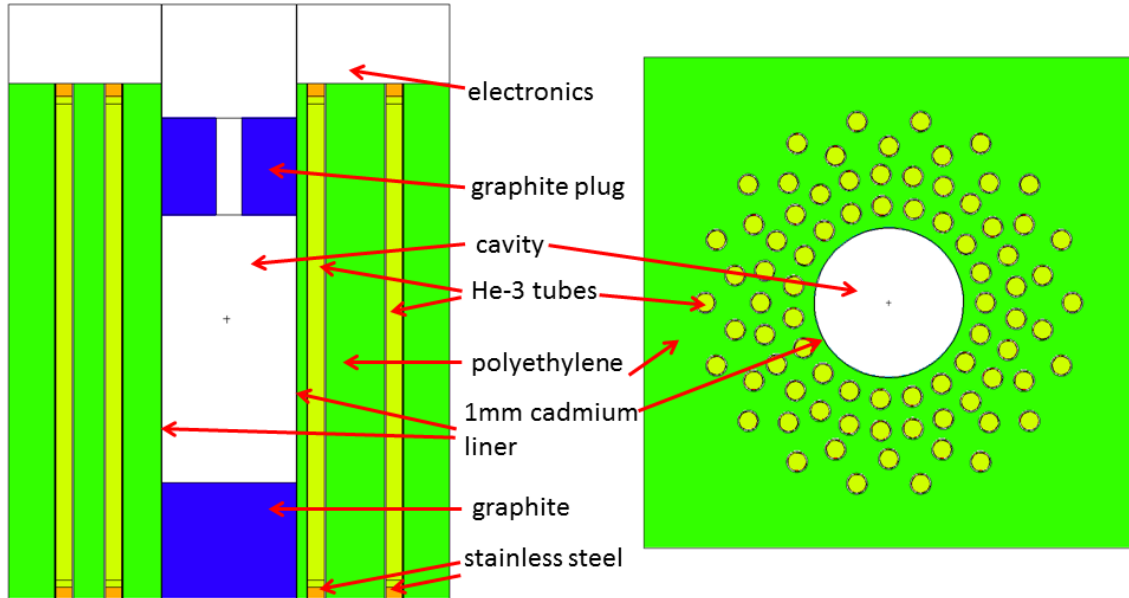


Figure 3.2: The Plutonium Scrap Multiplicity Counter (left: Cut through the vertical plane; right: Cut through the horizontal plane). White indicates air or materials of little relevance for neutron transport, blue indicates graphite, orange stainless steel, green polyethylene, the greenish yellow He-3.

the cavity. The graphite component scatters neutrons that would otherwise escape the detector. Some neutrons that scatter with the detector's polyethylene may be reflected back to the detector cavity. Cadmium has a large thermal neutron capture cross-section. Due to the presence of a cadmium liner, neutrons that were thermalized by elastic scattering with polyethylene and were reflected back are captured, thereby reducing the rate of reflected neutrons in the cavity.

3.2 Plutonium Samples and Measurements

The PSMC in Ispra was characterized using plutonium samples in addition to a Cf-252 source to ensure the validity of the calibration for the plutonium measurement campaign. The results are shown in Table 3.1, where also the dead-time δ is given.¹

¹The reason for the different efficiencies are different energy spectra: Cf-252 spontaneous fission spectra are different from Pu-239 and Pu-240 fission spectra; oxides have a contribution from (α, n) neutrons which also have a different energy spectrum. The efficiencies are given for samples placed in the center of the cavity. For one sample placed in different positions, ϵ varies by less than 1% at different radial locations and by less than 3% at different axial locations, it varies less than 0.5% close to the center [31].

PD	$4.5 \mu s$
G	$64 \mu s$
f_d	0.6111
f_t	0.3859
δ	$44.3 ns$
ϵ	Pu metal: 0.561
	Pu oxide: 0.546
	Cf-252: 0.553

Table 3.1: Characteristics of the PSMC [30, 31]

These values have been used for the analysis (though δ is very short compared to the neutron rates of the measured samples and is therefore insignificant).

During the campaign, three different types of sources have been measured. The isotopic compositions were originally given for specific dates in the past. Because of decay and corresponding ingrowth, they have been updated to the measurement date. Table 3.2 shows the masses and isotopic compositions of those samples (one of each type) that will be analyzed in more detail in this chapter. Complete information on all sources are listed in Appendix Tables B.1 and B.2. In addition, a Cf-252 source has been measured.

Three weapons-grade metal samples in cylindrical shape have been measured (“PM” samples). The masses have been in the range of 10 – 20 *g*. Two of the samples have a Pu-240 content of about 4.5%, one has about 8.5%. The three samples are placed in containers for safety reasons. First, they are surrounded by an aluminum capsule which itself is in a stainless steel container. All containers are similar to the “PM1” sample container (Fig. 3.3).

The “PERLA PuO_2 ” samples are five oxide pellets with differing masses ranging from 2 – 20 *g* and two different isotopic compositions (13% or 26% Pu-240). They are surrounded by a 0.5 *mm* thick stainless steel encapsulation (see “PERLA PuO_2 10” sample in Fig. 3.4).

The “CBNM” samples are four PuO_2 pellets (5.5 *g* plutonium mass) of differing isotopic compositions, ranging from 6% to 25% Pu-240. As a representative example, the “CBNM 61” sample with its stainless steel container is shown in Fig. 3.5.

Altogether, the samples represent a sufficient range of isotopic compositions and masses in order to ensure a meaningful test of MCNPX-PoliMi. After background

	type	Pu mass [g]	isotopic composition [Pu wt-%]		
PM1	metal	12.5 ± 0.3	Pu-238:	0.004	± 0.0004
			Pu-239:	95.420	± 0.029
			Pu-240:	4.529	± 0.032
			Pu-241:	0.032	± 0.0006
			Pu-242:	0.015	± 0.002
			Am-241:	0.245	± 0.001
PERLA PuO_2 10	oxide	1.99	Pu-238:	0.058	
			Pu-239:	86.082	
			Pu-240:	13.270	
			Pu-241:	0.321	
			Pu-242:	0.270	
			Am-241:	1.483	
CBNM 61	oxide	5.55 ± 0.04	Pu-238:	1.028	± 0.003
			Pu-239:	65.837	± 0.028
			Pu-240:	26.698	± 0.024
			Pu-241:	2.020	± 0.009
			Pu-242:	4.418	± 0.006
			Am-241:	6.357	± 0.014

Table 3.2: Characteristics of measured samples (personal communication Dr. Paolo Peerani); uncertainties are listed where available.

	M		α		m_{Pu} [g]
PM1	1.080	± 0.001	-0.002	± 0.006	12.753 ± 0.062
PERLA PuO_2 10	1.024	± 0.001	0.674	± 0.006	1.958 ± 0.009
CBNM 61	1.030	± 0.001	0.994	± 0.006	5.473 ± 0.020

Table 3.3: PSMC measurement results

radiation subtraction, measurements that were at least 1000 seconds long have been performed for all samples. The samples have been placed in the center of a 16 cm spacer, so that they have been in the middle of the detector cavity. All measurement results (S , D and T) are shown in Appendix Table B.3. The values for M , α and m_{Pu} which result from the analysis of the measurement results are shown in Table 3.3. Comparing these results to Table 3.2, it is evident that neutron multiplicity counting can successfully distinguish between metals and oxides (see α) and determine m_{Pu} for low masses and multiplications.² The magnitude of potential systematic uncertainties appear to be low for the discussed measurements because the deviations between measured and characterized plutonium masses are small.

²Only some of the measurement results are shown here as a summary; none of the other measurement results show significantly higher deviations between measured and characterized plutonium masses.

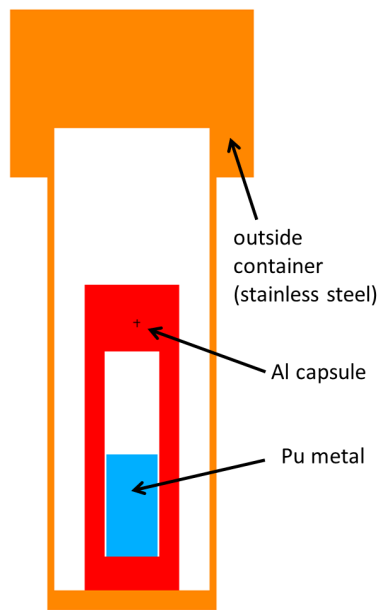


Figure 3.3: “PM1” sample; the outside container has a total height of 90 *mm*.

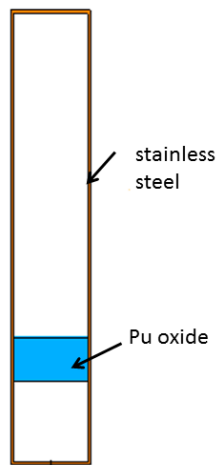


Figure 3.4: “PERLAPuO₂ 10” sample; the outside container has a total height of 79.5 *mm*.

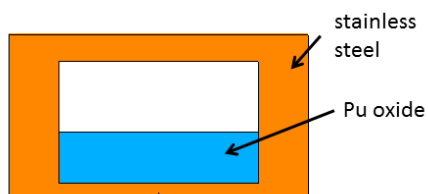


Figure 3.5: “CBNM 61” sample; the Pu oxide has a total height of 3.75 *mm*.

Chapter 4

Monte Carlo Simulation Capacity

Different configurations of items and surrounding materials must be assessed in order to study potential sources of neutron multiplicity counting bias for plutonium warhead and warhead component authentication. Monte Carlo simulations had to be the main tool for such an analysis, as only a very limited choice of sample configurations was available for measurements. For this purpose, the MCNPX-PoliMi code [32] has been used. As a first step, it has been assessed to which extent MCNPX-PoliMi is suited to simulate neutron multiplicity measurements. This has been done by comparing simulation results to the measurement results of section 3.2.

4.1 Simulation tools

4.1.1 MCNPX-PoliMi

The MCNPX-PoliMi code is a modification of the MCNPX code. MCNPX [33] is a Monte Carlo radiation and particle transport code. The user defines the geometry of a problem (for example sample and detector), the material properties within geometry cells, reaction cross-sections to be used with the simulation and the desired output data. Furthermore, a radiation or particle source must be defined (for example spontaneous fission or (α, n) neutrons), including the source geometry/position, type and energy of emitted particles. Unless otherwise stated, cross-sections from

the ENDF/B-VII.1 library [10] have been used.

MCNPX-PoliMi is capable of simulating neutron multiplicity counting measurements: For defined cells (e.g. He-3 detector tubes), it can record a list of reaction events (e.g. neutron capture) and the time when these events occurred [34]. This pulse train data can then be further analyzed to produce S , D and T , see the next sub-section.

MCNPX-PoliMi samples the number of prompt neutrons from appropriate multiplicity distributions for each spontaneous and induced fission event [32]. Spontaneous fission multiplicity data from [17] are implemented for Cf-252 and Pu-240. For Pu-239 induced fission, different data sets can be chosen, in particular data based on models from Terrell [16] or Zucker and Holden [18]. Terrell assumes a Gaussian multiplicity distribution with a constant standard deviation. Since Zucker and Holden show that the standard deviation depends on the energy of the incoming neutron (see also sub-section 2.1.1), the Zucker and Holden data have been used for all simulations. Furthermore, (α, n) sources with neutrons that follow the appropriate energy spectra [35] can be adopted as a source.

4.1.2 Implementation of the multiplicity analysis

A tool that is part of the MCNPX-PoliMi package capable of deducing S , D and T from the pulse train is delivered, but the source code has not been available and having the option to apply changes in the analysis was desired. For this reason, a MATLAB code has been written in order to conduct this analysis and deduce M , α and m_{Pu} .¹

First, the code calculates the R+A and A gate distributions. For this step, it requires the input parameters PD and G . For every neutron pulse, it counts all recorded neutron pulses which occurred between PD and $PD + G$ after the time of the trigger neutron pulse. The A gate distribution is obtained from the neutron pulses counted from $1024 \mu s$ after the R+A gate was opened during the gate length G . After normalization, these distributions correspond to $k(i)$ and $b(i)$. Then, the code calculates S , D and T according to equations 2.20, 2.21 and 2.22 and calculates M , α and m_{Pu} when the required parameters ϵ , f_d , f_t as well as ν_{sfn} and ν_{in} and

¹Matthew McArthur helped develop the MATLAB code during his internship at ZNF in 2013. He has also written a manual for using the code.

the isotopic composition are provided. Calculating M , α and m_{Pu} from the R+A and A gate is called “multiplicity analysis” in the remainder of this dissertation. The MATLAB code has been compared with the MCNPX-PoliMi package tool; the S , D and T rates have been found to be in agreement up to four decimal units.

4.2 Thermal Neutron Scattering

First simulations using MCNPX-PoliMi and the MATLAB multiplicity analysis have been performed. A draft of the PSMC geometry has been implemented in MCNPX-PoliMi together with the sample geometries. All measurement configurations have been simulated. With standard nuclear cross-sections (ENDF/B-VII.1 [10]), one obtains large deviations between multiplicity measurements and simulations. The D and T rates are systematically overestimated by 6-17% and 10-35%, respectively, which would render multiplicity simulations essentially useless. Such deviations cannot be explained by systematic uncertainties of the detector characterization.

The reason for these deviations has been identified in the simulated neutron moderation process in polyethylene. For thermal neutrons, the de-Broglie wavelength becomes sufficiently large that they interact with the polyethylene’s molecular structure. Automatically, however, MCNPX-PoliMi only includes scattering of neutrons with nuclei. There is elastic and inelastic scattering with the molecular structure. In this case (and in contrast to elastic scattering on free atoms), elastic scattering does not include kinetic energy transfer between the neutron and the scatterer, since the scatterer’s mass (considering the entire solid) is much larger than the neutron’s. Inelastic scattering results in an energy loss or gain of the neutrons. Since the scatterer is in thermal motion, it can actually transfer energy to a thermal neutron. The neutron can transfer energy to the scatterer and thereby excite it which can be described by phonon excitation in the case of polyethylene [36]. A single neutron may excite a couple of phonons, or no phonons at all. The latter is the case of elastic scattering. Based on this model, cross-sections for thermal neutron scattering in polyethylene can be derived as detailed in Appendix C. These can be called by MCNPX-PoliMi upon user input. If this option is chosen, the code overwrites the nuclear cross-sections with the appropriate data below 4 eV [33, 37]. The agreement between theory and experiment is excellent, as can be seen from Fig. 4.1. It also shows the significant difference between the cross-sections of scattering with the nucleus and the molecular structure.

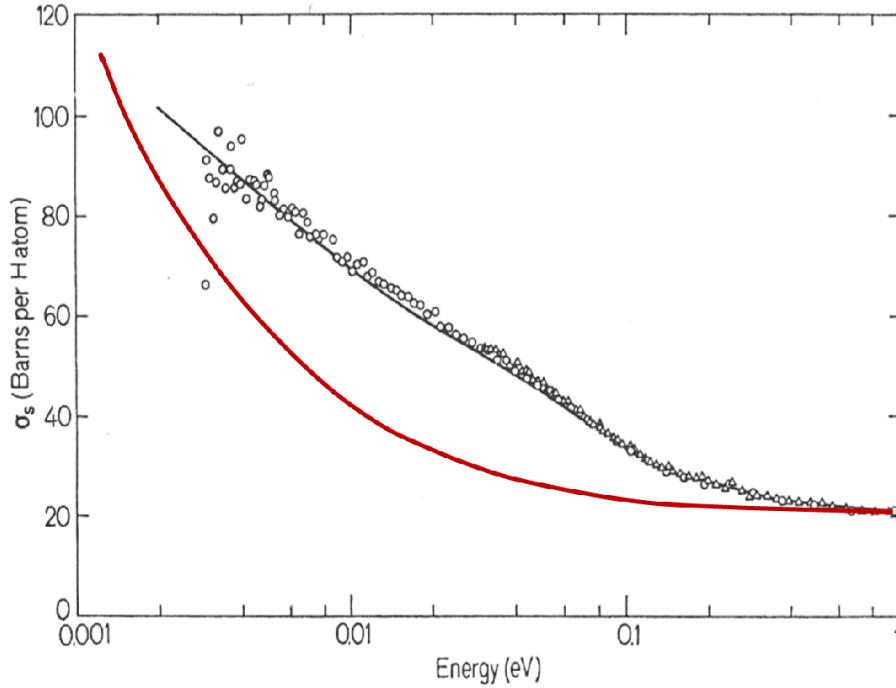


Figure 4.1: The derived (black line) and measured (dots) total cross-section of scattering with the polyethylene’s molecular structure is shown, taken from Sprevak and Koppel [38]. The red line represents the total nuclear cross-section [10].

4.3 Simulation Results

The detector geometry implemented in MCNPX-PoliMi is based on available sketches from the detector manufacturer [30]. Unfortunately, the resolution of the sketch is low and no further information could be obtained. Therefore, MCNPX-PoliMi simulations have been used to optimize the implemented detector design. A variety of parameters whose values were not accurately known has been identified. These have been varied in plausible ways to obtain the optimal parameters yielding the best simulation results while ensuring consistency with all available information. Table 4.1 shows the simulation results, the comparison to experimental values and the systematic and statistical uncertainties for the introduced choice of samples, while Table B.3 in the Appendix shows the simulation results of all samples. The uncertainties are discussed in the next sub-section.

	measured	$S.E.$	simulated	σ_{stat}^a	vert. tube	horiz. tube	polyethylene	gas pres-	multiplicity	emission	mass	isotopics	deviation
	[1/s]	[%]	[1/s]	[%]	pos. [%]	pos. [%]	density [%]	sure [%]	moments [%]	rates [%]	[%]	[%]	[%]
^{252}Cf	S	2884.0	0.1	2835.4	0.1	0.5	2.0	0.2	$Cf: 0.0$				-1.7
	D	1547.0	0.2	1606.5	0.2	1.0	4.5	0.3	$Cf: 0.2$	$^{252}Cf: 0.3$	n.a.	n.a.	3.8
	T	470.0	0.5	519.2	0.5	1.5	7.5	0.5	$Cf: 0.6$				10.5
PM1	S	360.2	0.5	342.2	0.1	0.5	2.0	0.2	$Pu: 0.0$			$^{239}Pu: 0.03$	-5.0
	D	137.9	0.5	136.5	0.2	1.0	4.5	0.3	$Pu: 0.8$	$^{240}Pu: 1.1$	2.4	$^{240}Pu: 0.71$	-1.0
	T	42.2	1.1	41.5	0.5	1.5	7.5	0.5	$Pu: 2.5$				-1.8
PuO_{210}	S	250.6	0.1	258.0	0.1	0.5	2.0	0.2	$Pu: 0.0$	$^{240}Pu: 1.1$			2.9
	D	50.6	0.7	51.9	0.3	1.0	4.5	0.3	$Pu: 0.8$	$(\alpha, n):$	n.a.	n.a.	2.4
	T	10.2	1.7	10.2	0.8	1.5	7.5	0.5	$Pu: 2.5$	2.8			-0.4
CBNM 61	S	2287.5	0.2	2216.1	0.1	0.5	2.0	0.2	$Pu: 0.0$	$^{240}Pu: 1.1$		$^{239}Pu: 0.04$	-3.1
	D	393.6	0.2	406.6	0.4	1.0	4.5	0.3	$Pu: 0.8$	$(\alpha, n):$	0.7	$^{240}Pu: 0.09$	3.3
	T	84.0	0.5	93.2	1.0	1.5	7.5	0.5	$Pu: 2.5$	2.8			11.0

Table 4.1: Comparison of measured and simulated S , D and T rates for four different samples including the deviation between simulation and measurement. For the experimental values, the standard error $S.E.$ is given, for the simulated values, the statistical uncertainties are given as well as further uncertainties addressed in the text. N.a. indicated that data were either not available or that the field is not applicable.

^aThe statistical uncertainty of the simulation is not in agreement with the measurement uncertainty as the simulations do not correspond to the same measurement times.

4.3.1 Systematic and statistical uncertainties

Systematic uncertainties arise from unknown details of the detector design, the sample properties, and nuclear data used in the analysis. Concerning the detector design uncertainties, a sensitivity analysis was performed in order to obtain uncertainty assessments for individual parameters during the optimization process of the simulated detector design. For the sample properties uncertainties, information was either available or a sensitivity analysis has been performed as above. For nuclear data uncertainties, published information has been used. The systematic uncertainties are shown in Table 4.3. Their influence on the S , D and T rates is listed in Table 4.1.

It also shows that the statistical uncertainties of both the simulations and measurements are very small compared to the systematic uncertainties. Nevertheless, this is treated here in more detail. Three different probability density functions were evaluated (Poisson distribution, multinomial distribution, semi-empirical approach). All presented functions were implemented in the MATLAB multiplicity analysis code.²

In the experiment, a measurement consists of multiple runs. Each run measures a multiplicity distribution, from which the S , D and T values are obtained. Their mean and standard error are calculated. The mean of the standard errors $S.E.$ from all the conducted measurements and its standard error are

$$\begin{aligned} S.E._S &= (0.16 \pm 0.11)\% \\ S.E._D &= (0.36 \pm 0.18)\% \\ S.E._T &= (1.05 \pm 0.55)\% \end{aligned} \tag{4.1}$$

For individual simulations, an appropriate model must be chosen for the uncertainty prediction. In Poisson statistics, the uncertainty for a count rate G_i of multiplicity i of the multiplicity distribution $G(i)$ is given as

$$\text{var}(G_i) = G_i \tag{4.2}$$

²They were implemented by Matthew McArthur during his internship at ZNF.

Type	Influence	Estimate
vertical position of He-3 tubes	Influence on ϵ as neutron flux density from a source placed in the middle of the detector is different at various tube heights - being maximal at the same height as the source.	$\pm 1 \text{ cm}$
horizontal position of He-3 tubes	Influence on ϵ and gate fractions. The closer the He-3 tubes are to the cavity, the smaller is the die-away time as neutrons travel through less polyethylene before being detected, thus increasing the gate fraction. Through the change in moderation, ϵ is affected due to neutron spectrum changes and capture by hydrogen.	$\pm 4 \text{ mm}$
polyethylene density	Influence on ϵ and the gate fractions due to neutron moderation and capture.	$\pm 0.5\%$
pressure of the He-3 gas	Direct influence on ϵ .	$\pm 1\%$
cadmium liner thickness	Detection rates increase significantly only after reducing the thickness by a factor 10.	none
position of the sample within the cavity	ϵ depends very little on the sample position, the position was measured well.	none
uncertainties from the gate electronics	The gate lengths were slightly changed, but in all cases the results were much worse than for a gate length of $64 \mu\text{s}$ so that it is assumed that the simulated gate lengths were exact.	none
sample mass and isotopic composition	These uncertainties mainly influence the spontaneous fission rate and the multiplication.	see Table 4.1
sample safety containers	Reasonable variations in the container designs were simulated; the influence was negligible.	none
fission and (α, n) rates	Uncertainty data for Cf-252 and Pu-240 fission and plutonium oxide (α, n) rates are available, see 2.1.	see Table 4.1
multiplicity distribution moments for spontaneous and induced fission	The values of the moments of Pu-239, Pu-240 and Cf-252 are based on the mean value of various measurements. The standard deviation is larger than the individual statistical uncertainties [39] and indicated the uncertainties of the moments. In addition, the induced fission moments of Pu-239 depend on the energy of the incoming neutron (see sub-section 2.1.1). As the exact neutron spectrum is usually not known in experiments, additional uncertainties are introduced, as detailed in sub-section 5.1.	see Table 4.1

Table 4.3: Description and estimation of systematic uncertainties

The variance of S , D and T is calculated by error propagation. However, neutron multiplicity counting does not follow Poisson statistics. As more than one neutron may be emitted with one fission event, not all detected neutrons are independent of each other. The counting technique introduces further correlations, because the same neutron may be counted in more than one gate as more than one gate may be open at the same time. Accordingly, Poisson statistics underestimate the variance.

The multinomial distribution is an often cited model for neutron multiplicity counting, see for example [21, 40]. It assumes that every individual G_i exhibits a binomial distribution and that the total neutron count rate $\Sigma G_i = S$ does not have an associated uncertainty ($\sigma_S = 0$). In addition to the variances, this introduces covariances between the count rates of the individual multiplicities [41]:

$$\text{var}(G_i) = G_i - \frac{G_i^2}{S} \quad \text{cov}(G_i, G_j) = -\frac{G_i \cdot G_j}{S} < 0 \quad (4.3)$$

The variances of S , D and T are again obtained from the error propagation

$$\text{cov}(S, D, T) = A \cdot V \cdot A^T \quad (4.4)$$

where A is the matrix of the partial derivatives $\partial S/\partial G_i$, $\partial D/\partial G_i$ and $\partial T/\partial G_i$, A^T is the corresponding transposed matrix and V is the matrix of the covariances of the individual multiplicities. As $\sigma_S = 0$ does obviously not reflect reality, $\text{var}(S)$ must be calculated by different means. It is reported in [41] that the multinomial approach yields the best uncertainty results compared to other approaches. One could disagree with this conclusion as the multiplicity variances of the multinomial distribution are even smaller compared to the Poisson distribution:

$$G_i - \frac{G_i^2}{S} < G_i \quad (4.5)$$

For $\text{var}(D)$, all derivatives of matrix A are positive.³ Therefore, the contribution from the multiplicity variances is positive. Accordingly, the contributions from the multiplicity covariances are all negative as $\text{cov}(G_i, G_j) < 0$. With this result and

³Matthew McArthur helped calculate the derivatives during his internship at ZNF.

equation 4.5, it is clear that the $var(D)$ using multinomial statistics is smaller compared to Poisson statistics. For $var(T)$, the same applies except for a few covariance terms having a positive contribution, but the negative effect dominates.⁴ It is difficult to understand how the multinomial distribution should be preferred over the Poisson distribution realizing that the Poisson distribution already underestimates the variance.

A third uncertainty model is the semi-empirical approach which adds a correction factor to the Poisson uncertainty. The starting point is an attempt to describe the expected variance theoretically exact (as shown in [42]). Until to-date, however, the theory must be backed up by empirical corrections to agree with measurement results. The variances are [41, 43]

$$\begin{aligned}
var(S) &= \left(1 + \frac{\epsilon \nu_2}{\nu_1}\right) \cdot var(S)_{Poisson} = \left(1 + \frac{2D}{f_d \cdot S}\right) \cdot var(S)_{Poisson} \\
var(D) &= \left(1 + \frac{4\gamma \epsilon \nu_2}{\nu_1}\right) \cdot var(D)_{Poisson} = \left(1 + \frac{8\gamma D}{f_d S}\right) \cdot var(D)_{Poisson} \\
var(T) &= \left(1 + \frac{5\gamma \epsilon \nu_2}{\nu_1}\right) \cdot var(T)_{Poisson} = \left(1 + \frac{10\gamma D}{f_d S}\right) \cdot var(T)_{Poisson} \\
\gamma &= 1 - \frac{(1 - e^{-G/\tau})}{G/\tau}
\end{aligned} \tag{4.6}$$

The standard deviations of all models have been calculated with the MATLAB code for all measured samples and can be compared to the experimental standard errors. For each sample, the deviation between the three models (theoretical uncertainties) and the experimental value have been calculated. The deviations vary extensively among the different samples, however no systematic trends were found between the individual samples. Therefore the means of the deviations of all samples are given along with the corresponding standard errors, see Table 4.4. The mean deviations of S , D and T between the standard deviations calculated with the semi-empirical model and the experimental standard errors are the smallest. It must be taken into account, though, that the standard errors of these deviation means are very large.⁵ Accordingly, the statistical uncertainties in Table 4.1 have been calculated with the semi-empirical approach, as have been all statistical uncertainties of simulations stated in this dissertation.

⁴Ibid.

⁵This is not dramatic as the statistical uncertainties themselves are very small in these cases.

	deviation [%]
S, Poisson	-36.0 ± 31.4
S, Semi-empirical	-13.8 ± 40.9
D, Poisson	-20.4 ± 22.3
D, Multinomial	-28.4 ± 20.5
D, Semi-empirical	-1.4 ± 25.3
T, Poisson	-13.4 ± 51.6
T, Multinomial	-14.4 ± 51.2
T, Semi-empirical	12.3 ± 59.8

Table 4.4: Deviations between theoretical statistical uncertainty predictions and experimental uncertainties

4.3.2 Simulation capacity assessment

Having studied simulated results as well as the systematic and statistical uncertainties, the MCNPX-PoliMi simulation capacity can be assessed. The calculated means of the deviations between simulation and measurement from all samples and the standard errors are

$$\begin{aligned}
\Delta S &= (-2.3 \pm 3.2)\% \\
\Delta D &= (2.9 \pm 3.5)\% \\
\Delta T &= (5.4 \pm 9.4)\%
\end{aligned}
\tag{4.7}$$

Although the identified uncertainties of the individual samples vary somewhat as can be seen from Table 4.1, they are similar and the standard errors of $\Delta S, \Delta D$ and ΔT appear to be in agreement with the systematic and statistical uncertainties addressed in Tables 4.1 and 4.3. It is refrained from performing an exact error propagation as various correlations of errors are difficult to quantify. The uncertainty from the horizontal tube position alone suffices for explaining the overall uncertainty.

As the standard errors of $\Delta S, \Delta D$ and ΔT are larger than $\Delta S, \Delta D$ and ΔT themselves, the conclusion is that the relevant uncertainties were identified, i.e. that potential additional uncertainties only have a minor influence. As the simulated results with their uncertainties are in agreement with the experimental results, it is concluded that the MCNPX-PoliMi code is suited for multiplicity simulations and that the implemented detector model is reasonably accurate. With this confidence, further simulations have been conducted to study potential sources of bias in neutron

multiplicity counting.

Chapter 5

Neutron Multiplicity Counting Bias

This chapter studies sources of bias in neutron multiplicity counting to test the reliability of the technique. This is done particularly in regard to authentication of warheads and warhead components: With the limited and automated output of an information barrier, measurement results are not directly shown. Therefore, a very high reliability of the measurements is required as they cannot be evaluated afterwards by the inspectors.

One type of bias has previously been researched and is physically well understood: It concerns inadequate knowledge of parameters required for the multiplicity analysis. For example, systematic uncertainties may be associated with parameters determined from the detector calibration. Bias from inadequate knowledge of parameters is discussed in section [5.1](#).

As neutron multiplicity counting is usually used for samples that do not have large masses and volumes (i.e. highly multiplicative samples), open research questions regarding the feasibility for highly multiplicative samples remain. Therefore, it is also examined if additional bias occurs when large samples such as warheads or warhead components are measured. The focus is on the fundamental basis of neutron multiplicity counting: It is researched whether the physics of the neutron source is accurately described by the neutron multiplicity counting equations (derivation in sub-section [2.3.1](#)). It is also assessed how the magnitude of bias depends on the specific sample configuration in order to assess the reliability of neutron multiplicity counting when the sample configuration remains largely unknown.

In section 5.2, potential bias of highly multiplicative samples without further materials between plutonium and the detector (which corresponds to bare warhead components) is discussed. In section 5.3 it is shown what the influence of polyethylene around the plutonium component is. This demonstrates relevant effects that would occur in assembled warheads or warhead components located in a storage container.

5.1 Bias from Inadequate Knowledge of Parameters

As can be seen from equations 2.25, 2.26 and 2.27, the parameters ϵ , f_d , f_t , ν_{sfn} and ν_{in} are required as input parameters in the multiplicity analysis to solve the equations for M , α and F . ϵ , f_d and f_t depend on the neutron energy spectrum, the neutron transport from the fissile material to the detector and the detection mechanism.

ϵ depends on the spectrum of neutrons that leave the sample. Therefore, it is influenced by the sample configuration: The reason is the energy-dependence of the (n,p) cross-section of He-3. While ϵ is generally influenced by the isotopic composition as neutrons of different energies are emitted, the spectra of neutrons emitted by Pu-239 and Pu-240 are similar, see Fig. 2.3. The effect will be minor unless relevant amounts of other isotopes are present. ϵ also depends on the sample geometry as elastic and inelastic scattering within the sample changes the neutron spectrum and as the reaction rate depends on the path lengths of the neutrons. Moreover, (α, n) neutrons have a different energy spectrum than fission neutrons. If there are further materials between the fissile material and the detector, scattering in this material will also change the energy spectrum. Also, neutrons may be captured in such materials thus reducing ϵ . The PSMC's efficiency ϵ varies by about 5% for neutron energies between 0.5 and 3 MeV [44].

f_d and f_t depend on the die-away time. The longer the die-away time, the smaller is the fraction of counted D and T coincidences for finite gate lengths. The die-away time is influenced by the measurement configuration: In particular moderating material between fissile material and detector will have an impact on the neutron lifetime. A study finds that the average time when induced fission occurs after the beginning of the specific "superfission" is increased by over a factor 20 when a 7.5 cm thick beryllium reflector is present around the fissile material. It remains

below 200 ns [45]. As this is a very thick reflector, the average time will not be significantly higher for configurations relevant for this dissertation. Furthermore, neutrons may be reflected back to the fissile material either from the detector's polyethylene or from materials between fissile sample and detector. Then, they can undergo secondary reactions, with those neutrons being detected at a later time. To reduce reflection from the detector's polyethylene, a cadmium liner (see section 3.1) can be used between detector and sample to limit this effect, but cadmium does not prevent the reflection of fast neutrons.

The nuclear data uncertainties associated with ν_{sf_n} and ν_{in} have been introduced in Table 4.3. The ν_{in} depend on the energy of the neutron inducing fission (see subsection 2.1.1). By default, the standard software used for multiplicity measurements [40] calculates with the data for 2 MeV neutrons:

$$\nu_{i1} = 3.163 \quad \nu_{i2} = 8.240 \quad \nu_{i3} = 17.321 \quad (5.1)$$

The accurate average induced fission moments are calculated according to

$$\nu_{in} = \int \nu_{in}(E) \cdot W(E) \cdot w_{\sigma}(E) dE \quad (5.2)$$

so it corresponds to an average weighted over the neutron energy spectrum $W(E)$ and the probability of these neutrons to induce fission, i.e. the fission cross-section normalized to unity $w_{\sigma}(E)$. In the following, ν_{in} always refer to the moments averaged over the specific spectrum of a sample. When spectra vary at different positions in the sample, they must be weighted accordingly:

$$W(E) = \frac{1}{V} \int W(E, \vec{r}) dV \quad (5.3)$$

The more is known about a sample in advance, the more accurate will the multiplicity counting analysis be. With sufficient knowledge, calibration sources could be used that closely represent the actual sample for the determination of ϵ , f_d and f_t . If materials between fissile sample and detector will be present, this or similar material can already be present during the detector calibration to include its effects. Monte Carlo simulations could be performed to obtain the neutron spectrum in order to

calculate ν_{in} . As the available information regarding warheads and warhead components will be very limited, increased uncertainties need to be taken into account. These effects are not evaluated further in this dissertation, as they are physically understood.

5.1.1 Preparations for further bias studies

To study the physical effects of the plutonium sample in isolation from the sources of bias introduced above, a theoretical “idealistic detector” has been simulated. The according conditions are a detector that always satisfies $\epsilon = f_d = f_t = 1$, that reflection of neutrons back to the source is minimized and that the accurate average induced fission moments ν_{in} are used.

A hollow sphere of He-3 with an extraordinarily large density of 10 g/cm^3 has been assumed. The inner and outer radii have also been extraordinarily large (20 m and 40 m). He-3 both moderates the neutrons and subsequently captures them. Because of the high density and the large volume, $\epsilon = 1$ is obtained, regardless of the emitted neutron energy spectrum. MCNPX-PoliMi simulations demonstrate that no neutrons escape the detector in the outward direction.

The gate fractions f_d and f_t both equal unity when the simulated gate length is sufficiently long to count all coincidences. MCNPX-PoliMi simulations show that the die-away time of this detector for an unshielded ^{252}Cf source is $5.6\ \mu\text{s}$. Gate lengths of $G = 1000\ \mu\text{s}$ have been applied with $PD = 0\ \mu\text{s}$ for all simulations discussed throughout this chapter.

Reflection of neutrons from the detector back to the sample is minimized due to the large detector cavity. For a neutron escaping the detector surface in the direction of the cavity, the solid angle of the sample is very small for all reasonable sample dimensions. For a plutonium sphere with a 4.9 cm radius, MCNPX-PoliMi simulations show that $8 \cdot 10^{-5}\ \%$ of the neutrons reaching the detector are reflected back and re-enter the plutonium sphere, which is negligible.

The ν_{in} have been calculated for induced fission of Pu-239 assuming the Pu-239 neutron energy spectrum (see Fig. 2.3). With equation 5.2 the result is

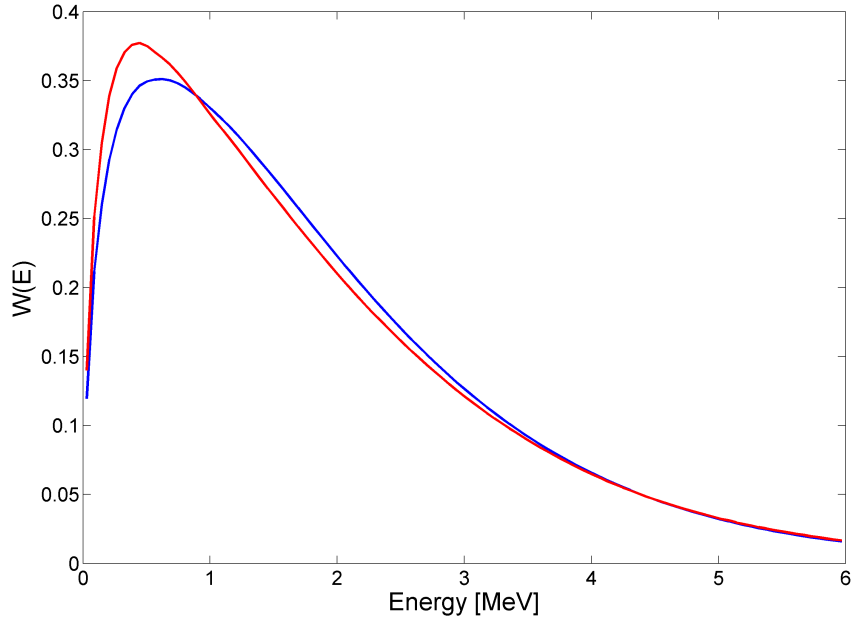


Figure 5.1: Neutron energy spectrum of Pu-239 induced fission (blue) and of a 1000 g plutonium metal solid sphere (red)

$$\nu_{i1} = 3.209 \quad \nu_{i2} = 8.571 \quad \nu_{i3} = 18.740 \quad (5.4)$$

This result could be used for further simulations of different metals containing Pu-239 and Pu-240 if the following assumptions (a) and (b) were reasonable:

(a) it must be assumed that the neutrons that induce fission follow the Pu-239 fission energy spectrum. While the Pu-239 induced fission and Pu-240 spontaneous fission spectra are very similar, the effect of neutron moderation must be taken into account: The neutron spectrum of a solid plutonium metal sphere (1000 g, 94% ^{239}Pu , 6% ^{240}Pu , $\rho = 19.8 \text{ g/cm}^3$, radius 2.29 cm) has been simulated. In Fig. 5.1, this spectrum is compared to the Pu-239 induced fission spectrum. The simulated spectrum is slightly shifted towards lower energies. The neutron moderation is mostly the result of inelastic scattering: Elastic scattering in plutonium results in a small energy change and has very little relevance, see sub-section 2.1.2. The induced fission moments for the simulated spectrum are

$$\nu_{i1} = 3.183 \quad \nu_{i2} = 8.420 \quad \nu_{i3} = 18.196 \quad (5.5)$$

The effect of inelastic scattering on the neutron spectrum depends on the precise

sample configuration. The 1000 g solid sphere is one of the samples with the longest neutron path lengths simulated in this dissertation. It therefore represents a rather pessimistic estimate of how the moments can differ. For most simulations, the moments will be between equations 5.4 and 5.5. As the difference is tolerable it is concluded that assumption (a) is reasonable.

(b) it must be assumed that induced fission in Pu-240 is negligible. This is reasonable in particular due to the similar multiplicities compared to Pu-239 [10], the somewhat lower cross-section compared to Pu-239 (Fig. 2.1 and 2.2) and because there is significantly less Pu-240 than Pu-239 in all reasonable samples. Therefore, the according data will be used in the multiplicity analyses below. Assumptions (a) and (b), however, introduce a small bias.

The simulations do not consider dead-time effects. Due to the small dead-time of the PSMC (44.3 ns [31]), it is irrelevant for small samples. Dead-time and its uncertainties should be taken into account for experiments with larger samples [46]. Dead-time correction procedures remain a research issue, see for example [47].

5.1.2 Simulation uncertainties

With the introduced detector configuration, the systematic uncertainties differ from those discussed in sub-section 4.3.1: As $\epsilon = f_d = f_t = 1$, they do not introduce uncertainty. After having calculated ν_{in} , the nuclear data used in the multiplicity analysis are in agreement with the data used in the MCNPX-PoliMi simulations. As long as parameters remain identical both in the simulation and the multiplicity analysis, no bias is introduced.¹ This leaves minor systematic uncertainties in addition to the statistical uncertainties.

To test this, two MCNPX-PoliMi simulations have been performed with the “idealistic detector” and the samples placed in the cavity’s center. A solid sphere of 20 g plutonium has been simulated (94% ^{239}Pu , 6% ^{240}Pu , $\rho = 19.8 \text{ g/cm}^3$, radius 0.622 cm) and a hollow sphere with the same mass, density and isotopic composition (inner radius 3.5 cm, outer radius 3.5065 cm). The simulated measurement time has been 3600 s. M , α and m_{Pu} have been calculated from the multiplicity analysis using S , D and T (indicated by subscript “*mult*”) and compared to the real data

¹Once a simulation is compared to a measurement, however, nuclear data uncertainty must be considered.

	20 g solid sphere	20 g hollow sphere
S [1/s]	1361.4 \pm 1.1	1244.5 \pm 1.0
D [1/s]	1603.2 \pm 3.9	1111.8 \pm 3.1
T [1/s]	1568.0 \pm 6.7	536.3 \pm 4.7
M_{mult}	1.0988 \pm 0.0004	1.0048 \pm 0.0003
α_{mult}	-0.001 \pm 0.004	0.000 \pm 0.004
$m_{Pu,mult}$ [g]	20.02 \pm 0.09	20.01 \pm 0.08
M_{true}	1.0996	1.0052
α_{true}	0.000	0.000
$m_{Pu,true}$ [g]	20.00	20.00
ΔM [%]	-0.07 \pm 0.04	-0.04 \pm 0.03
Δm_{Pu} [%]	0.10 \pm 0.45	0.05 \pm 0.40

Table 5.1: Multiplicity analysis results for two simulations

(subscript “*true*”): $m_{Pu,true}$ was known from the MCNPX-PoliMi input, $\alpha_{true} = 0$ as no oxides are present and M_{true} has been determined from the MCNPX-PoliMi output directly without the multiplicity analysis. The results are shown in Table 5.1, where also the deviations between multiplicity analysis and true values ΔM and Δm_{Pu} are given.

The mass deviations are smaller than their uncertainties, the multiplication deviations are slightly larger. This can be explained by the ν_{in} uncertainty addressed above. The deviations in both cases remain very small; the data does not indicate additional systematic uncertainties. This demonstrates that the utilization of the “idealistic detector” and the implemented ν_{in} data give excellent results. Without adapting the usually used 2 MeV ν_{in} data, the fissile mass is overestimated by around 3%, as calculations carried out for this work show.

5.2 Bias for Highly Multiplicative Plutonium Samples

To study bias, MCNPX-PoliMi simulations of solid and hollow spheres of mostly weapons-grade configurations of plutonium have been analyzed. It has been assumed that these configurations are suited to study effects that would similarly occur in warhead components (see for example [48]).

To study the multiplication process of the samples, neutron production and absorption rates have been determined from simulations. Neutrons produced in addition to spontaneous fission and (α, n) neutrons mainly come from induced fission, while

other reactions have reaction rates which are negligible for the analyses here. This neutron production rate per volume can be given as

$$P(\vec{r}) = N \cdot \int \Phi(E, \vec{r}) \cdot \nu_{i1}(E) \cdot (R_{239} \cdot \sigma_{239Pu f_{is}}(E) + R_{240} \cdot \sigma_{240Pu f_{is}}(E)) dE \quad (5.6)$$

where N is the number of targets per unit volume, $\Phi(E, \vec{r})$ is the neutron flux density, R_{239} and R_{240} are the isotopic fractions of Pu-239 and Pu-240 and $\sigma_{239Pu f_{is}}(E)$ and $\sigma_{240Pu f_{is}}(E)$ are the Pu-239 and Pu-240 induced fission cross-sections. Only these two isotopes are present in all following simulations. If further isotopes were present, they would need to be included in this and the following equations. $P(\vec{r})$ is a function of the position \vec{r} within the sample. In $P(\vec{r})$, only the newly produced neutrons from induced fission are considered, not the absorption of neutrons that induce fission. Including these and all further neutron absorption events in the cross-sections $\sigma_{239Pu abs}(E)$ and $\sigma_{240Pu abs}(E)$, the neutron absorption rate per volume is

$$A(\vec{r}) = N \cdot \int \Phi(E, \vec{r}) \cdot \{R_{239} \cdot (\sigma_{239Pu f_{is}}(E) + \sigma_{239Pu abs}(E)) + R_{240} \cdot (\sigma_{240Pu f_{is}}(E) + \sigma_{240Pu abs}(E))\} dE \quad (5.7)$$

The net number of neutrons N_{prod} produced in the entire volume corresponds to

$$N(\vec{r}) = P(\vec{r}) - A(\vec{r})$$

$$N_{prod} = \int N(\vec{r}) dV \quad (5.8)$$

The multiplication in the sample (total rate of neutrons leaking the sample divided by rate of primary neutrons, see sub-section 2.3.1) is expressed by

$$M = \frac{\nu_{sf1}F + N_{\alpha} + N_{prod}}{\nu_{sf1}F + N_{\alpha}} \quad (5.9)$$

The multiplication calculated with this equation corresponds to M_{true} . Besides taking into account neutrons from spontaneous fission and (α, n) reactions, the numerator includes N_{prod} which is the number of neutrons produced by induced

fission, taking into account neutron leakage,² subtracted by the number of absorbed neutrons. This shows the agreement with the explanation of the multiplication in sub-section 2.3.2. Table 5.2 shows the multiplicity analysis results performed after MCNPX-PoliMi simulations of the “idealistic detector” and solid and hollow sphere samples containing 94% Pu-239 and 6% Pu-240 ($\rho = 19.8 \text{ g/cm}^3$) of varying masses. The inner radius of the simulated hollow spheres is $r_{in} = 3.5 \text{ cm}$, the outer radii r_{out} of the solid and hollow spheres vary according to the masses.

In both simulation series, the multiplication increases with sample mass as is expected. For the hollow spheres, the same multiplication values correspond to larger masses than for the solid spheres. For small multiplications, the multiplicity analysis results agree with the true values either within their statistical uncertainties or are slightly larger, which can be explained by the ν_{in} uncertainties. However, as $m_{Pu,true}$ and M_{true} become larger, M_{mult} is overestimated and $m_{Pu,mult}$ underestimated. Comparing the solid and hollow spheres it can be seen that the deviation is neither a simple function of M nor m_{Pu} . In the simulations, the multiplication is overpredicted by as much as 5%, the mass is underpredicted by as much as 20%. Both deviations cannot be explained by the statistical uncertainties and increase with increasing mass/multiplication.

5.2.1 Spatially variant multiplication

The $m_{Pu,true} = 1000 \text{ g}$ solid sphere and $m_{Pu,true} = 6000 \text{ g}$ hollow sphere have been analyzed in more detail to understand the physics of these samples. Both have a fairly high mass bias so it should be possible to observe relevant systematic effects, furthermore differences between the different geometries can be studied. In the multiplicity analysis it is assumed that all spontaneous fission and (α, n) neutrons have the same multiplication, irrespective of the position of their emission \vec{r} . This can be seen from equation 2.6 where p , and accordingly M , are considered constant parameters. This assumption is called the “point model” [27]. To test the hypothesis that this issue is the reason of the bias, the dependence of M on \vec{r} has been studied and is presented in this sub-section.

²Neutron leakage is automatically included as N_{prod} is based on the neutron flux density which is obtained from MCNPX-PoliMi simulations of the precise geometry. Not including neutron leakage would correspond to a case where all neutrons would be reflected back once they leak a sample corresponding to an increased neutron flux density. This is not the case in the simulations.

	M_{true}	$m_{Pu,true}$ [g]	M_{mult}	$m_{Pu,mult}$ [g]	ΔM [%]	Δm_{Pu} [%]
solid	1.0996	20	1.0988 ± 0.0004	20.02 ± 0.09	-0.07 ± 0.04	0.1 ± 0.4
	1.1426	50	1.1443 ± 0.0004	49.73 ± 0.22	0.14 ± 0.03	-0.5 ± 0.4
	1.1887	100	1.1841 ± 0.0004	95.66 ± 0.44	-0.39 ± 0.03	-4.3 ± 0.5
	1.3997	500	1.4235 ± 0.0005	469.4 ± 2.4	1.70 ± 0.03	-6.1 ± 0.6
	1.5873	1000	1.6343 ± 0.0006	889.9 ± 5.0	2.96 ± 0.04	-11.0 ± 0.6
	1.9445	2000	2.0454 ± 0.0006	1595 ± 10	5.19 ± 0.03	-20.3 ± 0.8
hollow	1.0052	20	1.0048 ± 0.0003	20.01 ± 0.08	-0.04 ± 0.03	0.1 ± 0.4
	1.0116	50	1.0112 ± 0.0003	50.05 ± 0.18	-0.04 ± 0.03	0.1 ± 0.4
	1.0212	100	1.0206 ± 0.0003	100.18 ± 0.36	-0.06 ± 0.03	0.2 ± 0.4
	1.0856	500	1.0845 ± 0.0003	501.5 ± 1.9	-0.10 ± 0.03	0.3 ± 0.4
	1.1575	1000	1.1571 ± 0.0004	1001.0 ± 4.1	-0.03 ± 0.03	0.1 ± 0.4
	1.2969	2000	1.3000 ± 0.0005	1982 ± 9	0.24 ± 0.04	-0.9 ± 0.5
	1.5955	4000	1.6115 ± 0.0006	3851 ± 20	1.00 ± 0.04	-3.7 ± 0.5
	1.9577	6000	1.9966 ± 0.0006	5541 ± 32	1.99 ± 0.03	-7.7 ± 0.6

Table 5.2: Multiplicity analysis results (multiplication and mass) of MCNPX-PoliMi simulations (subscript *mult*), the true simulated values (subscript *true*) and the deviations of the simulated from the true values for different solid and hollow spheres

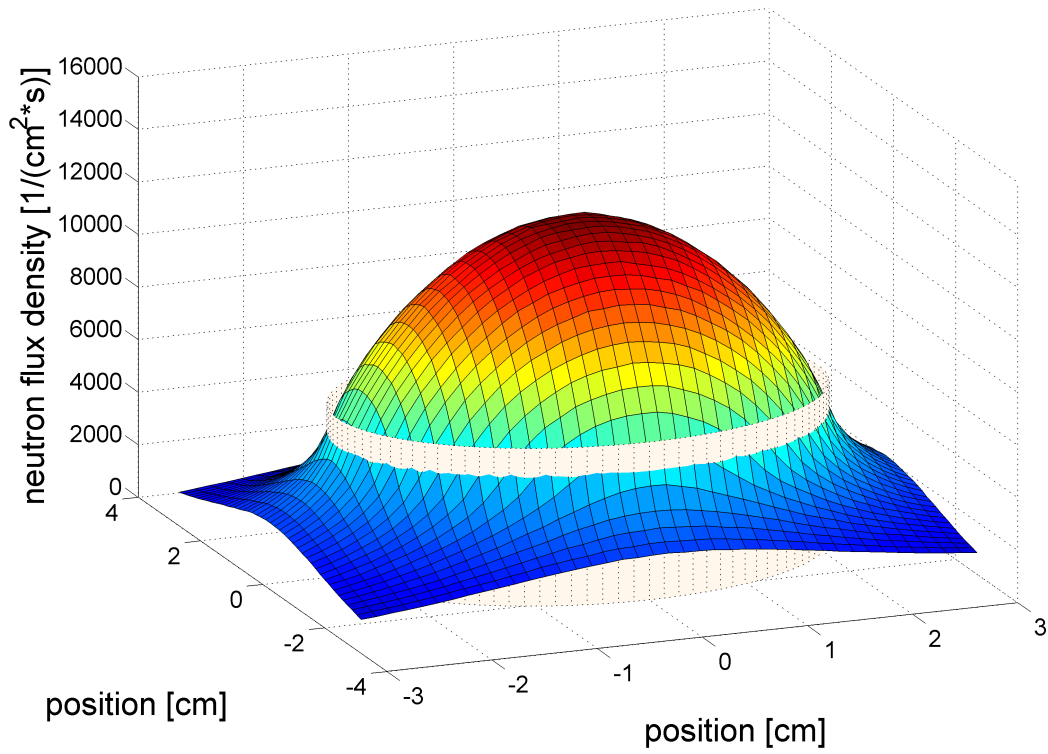


Figure 5.2: Neutron flux density of the 1000 g solid sphere. The cylinder marks r_{out} .

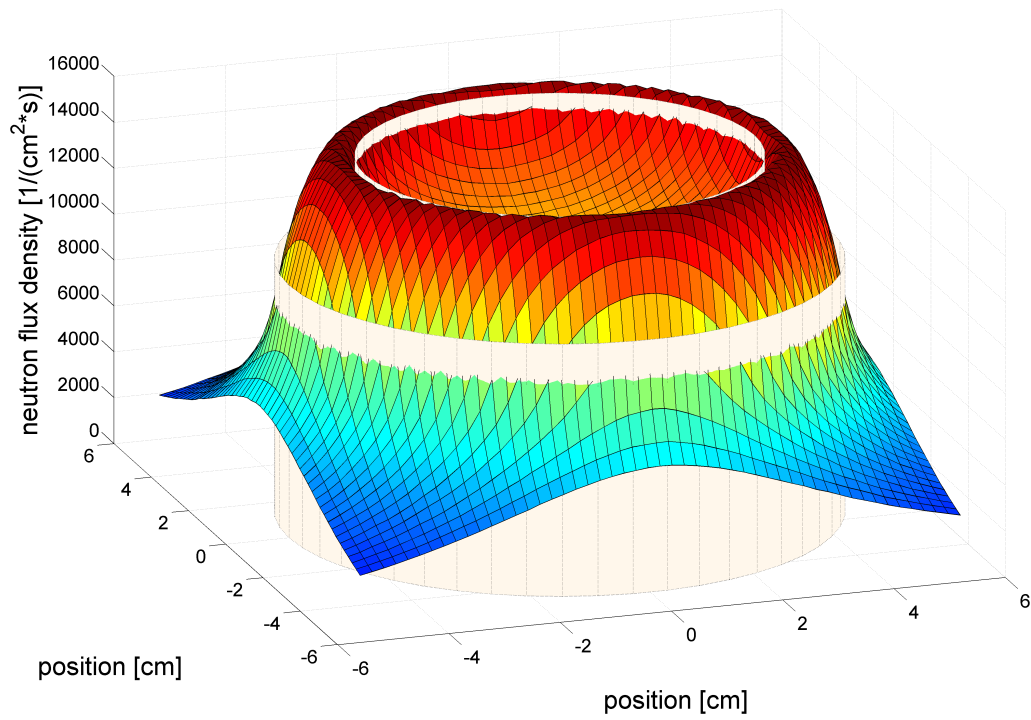


Figure 5.3: Neutron flux density of the 6000 g hollow sphere. The cylinders mark r_{in} and r_{out} .

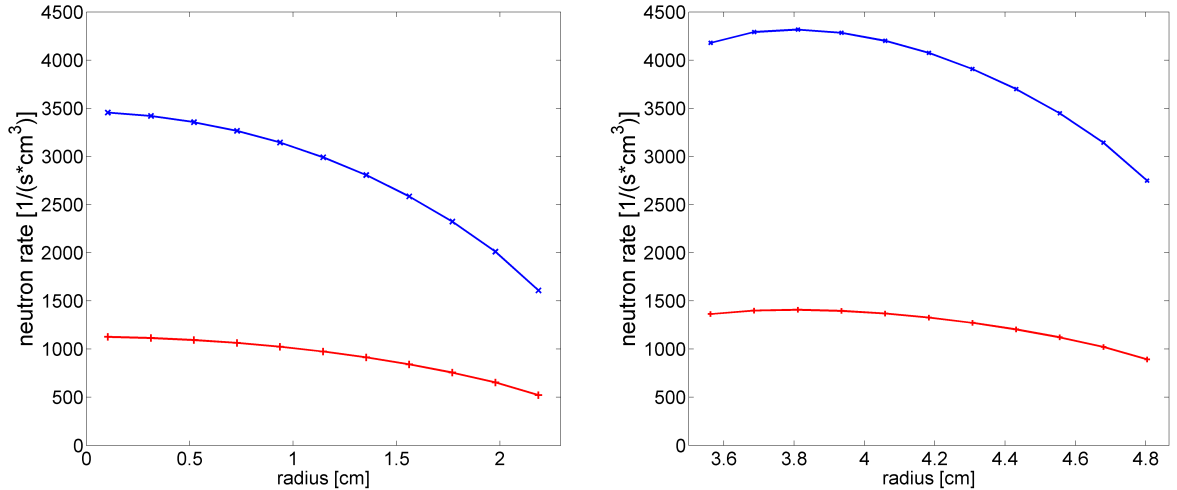


Figure 5.4: $P(r)$ (blue) and $A(r)$ (red) for the 1000 g solid sphere (left) and the 6000 g hollow sphere (right), lines are for guiding the eyes only

Fig. 5.2 and 5.3 show the total neutron flux density $\Phi(\vec{r})$ of a slice through both samples, obtained from MCNPX-PoliMi simulations. The observed rotational symmetry of the flux density is expected due to the sample geometries. It allows to consider the flux density as a function of radius $\Phi(\vec{r}) = \Phi(r)$ and correspondingly $P(r)$ and $A(r)$. For the solid sphere the maximum flux density is $\Phi_{max} = 12600 \text{ cm}^{-2}\text{s}^{-1}$, for the hollow sphere $\Phi_{max} = 15700 \text{ cm}^{-2}\text{s}^{-1}$. This difference can be explained by the hollow sphere's higher multiplication.

From $\Phi(r)$, $P(r)$ and $A(r)$ have been calculated at different positions in the volume by MCNPX-PoliMi, see Fig. 5.4. Each data point represents a hollow sphere volume element (imagine onion skins). $P(r)$ and $A(r)$ are almost proportional to $\Phi(r)$ because the neutron spectra are similar throughout the volume.

While spontaneous fission was previously simulated over the entire plutonium volume, more can be learned from the multiplication process of spontaneous fission neutrons only emitted at specific locations within the sample. For this purpose, partial volumes of the overall spheres have been defined: The solid sphere has been artificially divided into five spherical shells that contained 200 g of plutonium each (see Fig. 5.5); the hollow sphere has been divided into six spherical shells containing 1000 g. One MCNPX-PoliMi simulation has been run per spherical shell. Spontaneous fission has been programmed to only occur within the one spherical shell that has been considered, but neutron transport and all other reactions have been simulated throughout the entire sample volumes (1000 g and 6000 g, respectively). Fig.

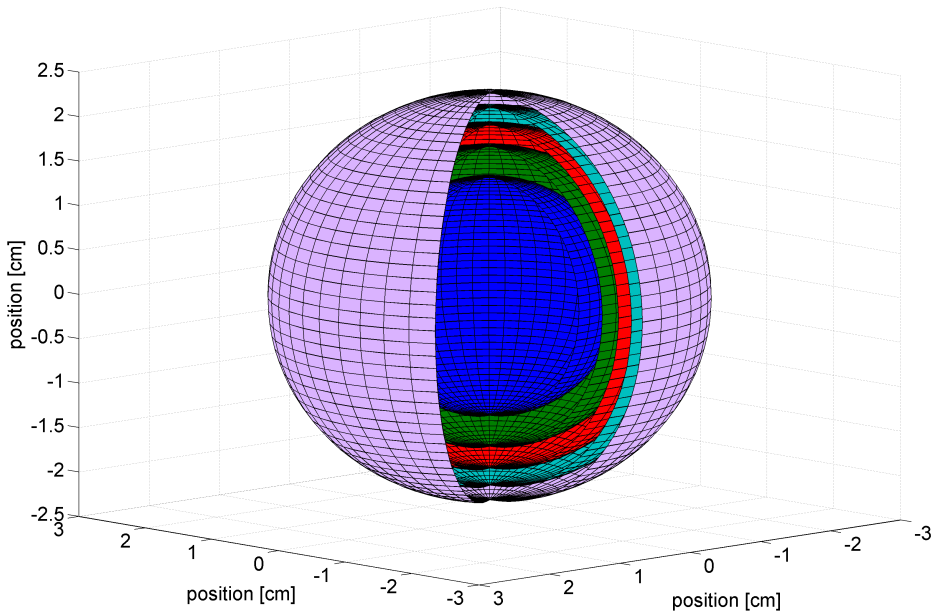


Figure 5.5: 1000 g solid sphere divided into 5 hollow spheres of equal mass, located between the depicted surfaces

5.6 shows $N(r)$ for all simulations. It can be seen that the maximum contribution to the neutron production rate in all cases occurs in vicinity of the spontaneous fission volume, although significant amounts of neutrons are produced everywhere in the sample volume. This can be explained by the mean free path of the neutrons (2.9 cm for 1 MeV neutrons in Pu-239, 2.8 cm in Pu-240 [10]). It is also in agreement with the neutron generation probability distributions (Fig. 5.7), i.e. the probabilities that a neutron within the entire neutron population of the sample belongs to a specific generation. These are based on MCNPX-PoliMi criticality calculations (1000 g solid sphere: $k_{eff} = 0.4862$, 6000 g hollow sphere: $k_{eff} = 0.5962$). In both cases over 40% of the neutron population are spontaneous fission neutrons which indicates that many neutrons leave the sample without inducing fission.

Fig. 5.6 also shows that N_{prod} and accordingly M of the individual shells differ (see equations 5.8 and 5.9, remembering that the mass of the shells per geometry are equal, so $\nu_{sf1}F + N_\alpha$ are equal as well). To better understand the dependence of M on the radius, spontaneous fission has been simulated from sphere surfaces of different radii that are located within the samples. Fig. 5.8 displays the resulting graph $M(r)$, where each data point corresponds to one fission surface.³ The average

³Although Fig. 5.4 and Fig. 5.8 show a similar behavior, they are not identical: In Figure 5.4, spontaneous fission occurs over the entire sample volume and the neutron production rate is

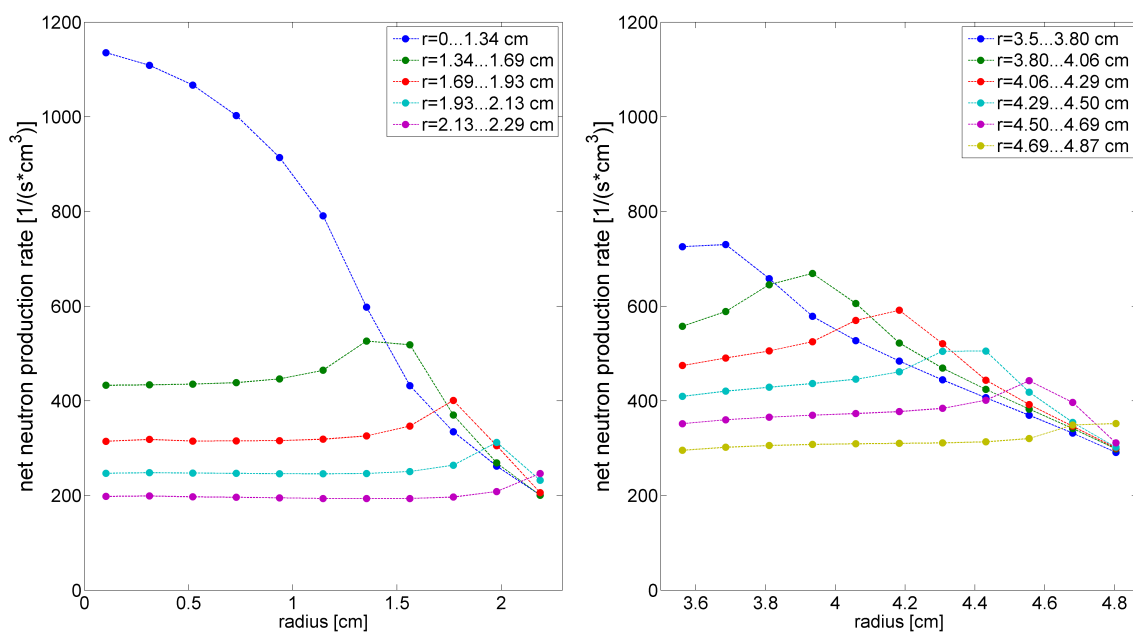


Figure 5.6: $N(r)$ of the 1000 g solid sphere (left) and 6000 g hollow sphere (right). For the individual curves, spontaneous fission is simulated only between the indicated radii, lines are for guiding the eyes only.

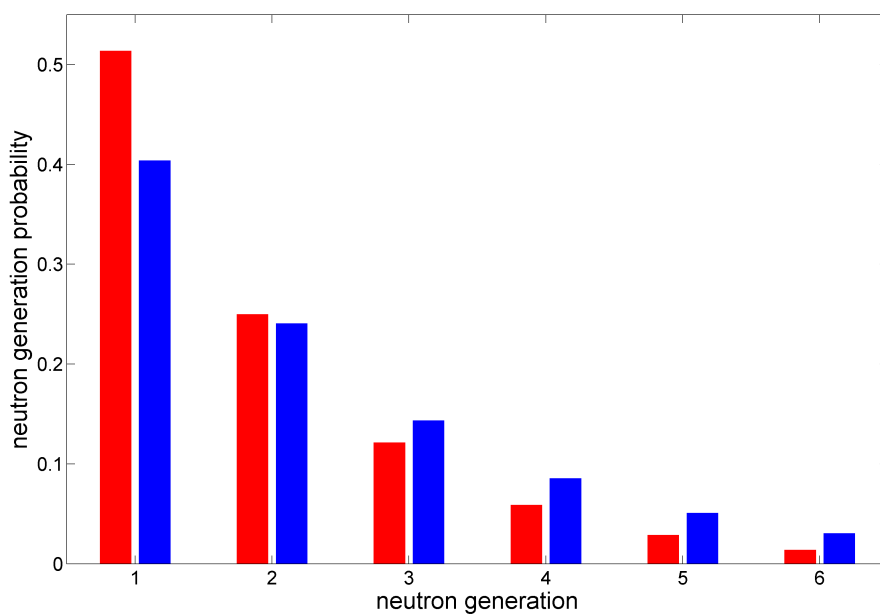


Figure 5.7: Neutron generation probabilities of the 1000 g solid sphere (red) and the 6000 g hollow sphere (blue). Neutron generation 1 refers to neutrons from spontaneous fission, generation 2 are neutrons from the first induced fission, etc.

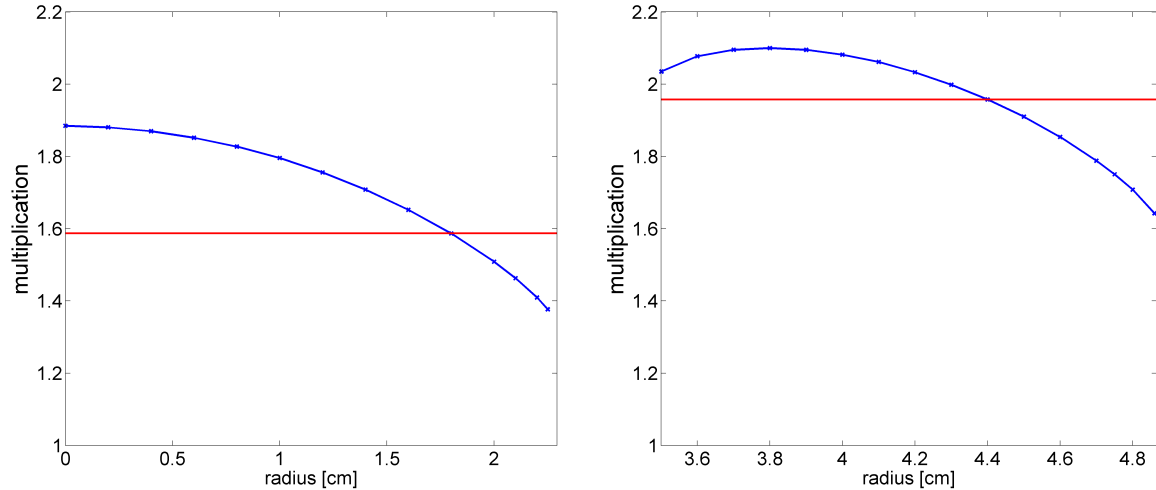


Figure 5.8: Multiplication as a function of spontaneous fission source radius (blue) and the average multiplication from spontaneous fission over the full fissile material volume (red). Left is the 1000 g solid sphere case, right is the 6000 g hollow sphere case.

multiplication of a sphere $\langle M \rangle_{sphere}$ can be calculated by appropriate weighing:

$$\langle M \rangle = \frac{1}{V} \int M(\vec{r}) dV \quad \Rightarrow \quad \langle M \rangle_{sphere} = \frac{1}{V} \int_{r_{in}}^{r_{out}} 4\pi \cdot r^2 \cdot M(r) dr \quad (5.10)$$

where $r_{in} = 0$ for a solid sphere. To explain $M(r)$, one may disregard the multiplication process / induced fission for a moment and discuss $\Phi(\vec{r})$ for a point neutron source, e.g. in the 6000 g hollow sphere. Fig. 5.9 describes the neutron flux density of a slice through the sphere for two point neutron sources, disregarding nuclear reactions in the volume. The black lines show where the neutron flux density is half of that of the preceding line. The source neutron flux density decreases with the squared distance from the point source.⁴ With sufficient scrutiny, one can estimate that $\int \Phi(\vec{r}) dV$ within the entire hollow sphere is larger for the point source at 3.8 cm than at 3.51 cm. This indicates why the neutron multiplication is higher at 3.8 cm, in agreement with Fig. 5.8. This consideration is only a first approximation as no nuclear reactions are included in the flux density distribution, but it is useful for

displayed as a function of radius. In Figure 5.8, the radius corresponds to a surface spontaneous fission source, while the multiplication that is shown at each radius is the result of neutron production in the full fissile material volume.

⁴ $\Phi = \frac{n}{4\pi r^2 \cdot t} \Rightarrow \frac{\Phi_2}{\Phi_1} = \frac{r_1^2}{r_2^2}$, where n/t is the neutron rate and Φ_1 and Φ_2 are the flux densities at radii r_1 and r_2 .

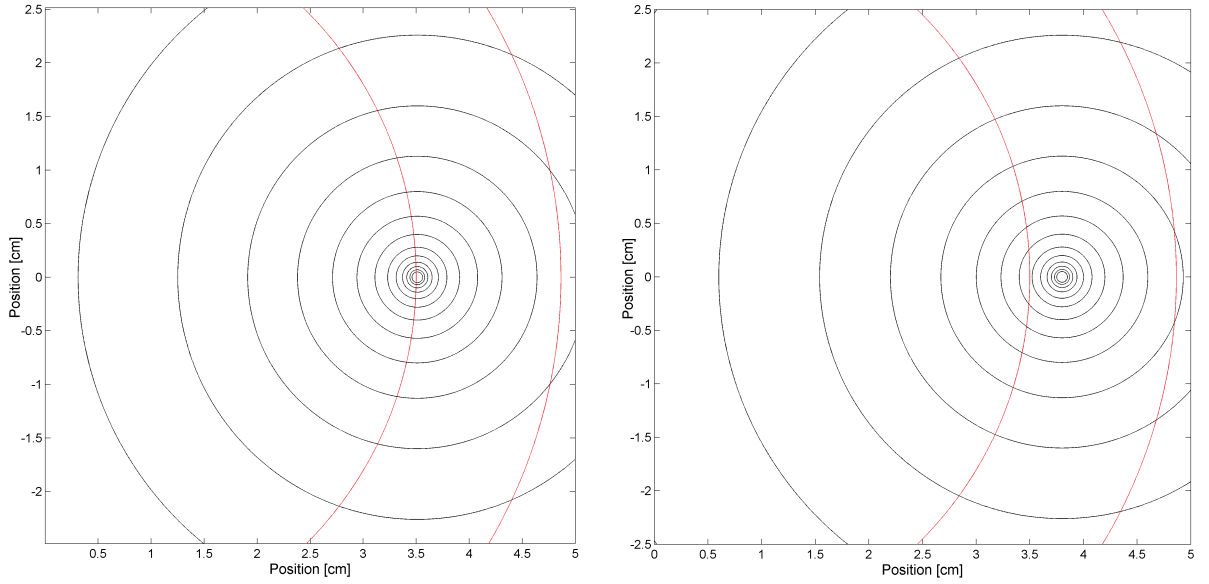


Figure 5.9: Flux density isolines (black) for a point neutron source in a 6000 *g* hollow sphere slice (red margins) at $r = 3.51$ *cm* (left) and $r = 3.8$ *cm* (right).

a qualitative description as over 60% of the neutrons leaving the sample are from spontaneous fission or the first induced fission (see Fig. 5.7).⁵ The same general argumentation explains the neutron production characteristics of the 1000 *g* solid sphere.

5.2.2 Existing correction model

As assumed, the previous sub-section has demonstrated the dependence of M on \vec{r} in the two cases (Fig. 5.8). The hypothesis that the spatially variant multiplication is the reason for the large deviations in Table 5.2 remains to be tested.

There had been limited success in applying correction factors that are functions of the measured multiplication to the multiplicity analysis: Krick et al. [49] ran MCNPX simulations with plutonium cylinders of different height/diameter ratios and masses. For each simulation, the multiplicity analysis was performed with results deviating from the true values. Separate S , D and T correction factors were empirically determined for each simulation to obtain the correct results. It was found that the correction factors can be given as a function of multiplication,

⁵Absorption of spontaneous fission neutrons (e.g. by induced fission reactions) further decreases the spontaneous fission neutron flux density over distance, but the neutrons emitted from induced fission increase the flux density and change its distribution.

independent of fissile mass. As these correction factors were determined empirically without a full theoretical understanding, it is difficult to generalize this approach, despite its specific success.

Croft et al. [50] proposed another model: In equations 2.25, 2.26 and 2.27, the multiplication appears up to the fifth order ($n = 5$). They assumed without proof that the physically correct values for the multiplication would be [50]

$$\begin{aligned}
M^n = \langle M^n \rangle &= \frac{1}{V} \int M^n(\vec{r}) dV \\
\implies \langle M^n \rangle_{sphere} &= \frac{1}{V} \int_{r_{in}}^{r_{out}} 4\pi \cdot r^2 \cdot M^n(r) dr
\end{aligned} \tag{5.11}$$

As the standard “point model” multiplicity analysis falsely assumes $M^n = \langle M \rangle^n$ ($\neq \langle M^n \rangle$), they propose that the equations of the multiplicity analysis can be corrected as follows [50]:

$$\begin{aligned}
g_n &= \frac{\langle M^n \rangle}{\langle M \rangle^n} \quad n = 2 \dots 5 \\
S &= F \cdot \epsilon \cdot M \cdot \nu_{sf1} (1 + \alpha) \\
D &= \frac{F \cdot \epsilon^2 \cdot f_d \cdot M^2}{2} \left[\nu_{sf2} g_2 + (g_3 \cdot M - g_2) \frac{\nu_{sf1} \cdot \nu_{i2}}{\nu_{i1} - 1} (1 + \alpha) \right] \\
T &= \frac{F \cdot \epsilon^3 \cdot f_t \cdot M^3}{6} \left[\nu_{sf3} g_3 + (g_4 \cdot M - g_3) (1 + \alpha) \frac{\nu_{sf1} \nu_{i3}}{\nu_{i1} - 1} + \right. \\
&\quad \left. 3(g_4 \cdot M - g_3) \frac{\nu_{sf2} \nu_{i2}}{\nu_{i1} - 1} + 3(g_5 \cdot M^2 - 2g_4 \cdot M + g_3) (1 + \alpha) \frac{\nu_{sf1} \cdot \nu_{i2}^2}{(\nu_{i1} - 1)^2} \right]
\end{aligned} \tag{5.12}$$

In the following, the proof of these equations is provided: Sub-section 2.3.1 introduced the “superfission” concept which assumes a primary neutron source (spontaneous fission and (α, n)) and subsequent multiplication of these primary neutrons by induced fission, described by M . The result was the normalized multiplicity distribution $P(\nu)$ and its factorial moments ν_1 , ν_2 and ν_3 describing the neutrons emitted by a “superfission”. According to the “point model”, $P(\nu)$ does not depend on the location of the primary neutron source, as the multiplication is independent of it. If this is not valid, ν_1 , ν_2 and ν_3 depend on the position \vec{r} of the primary neutron source. The correct factorial moments of the overall sample are the volume-weighted averages:

$$\langle \nu_n \rangle = \frac{1}{V} \int \nu_n(\vec{r}) dV \quad (5.13)$$

This integration can be performed with equations 2.8, 2.9 and 2.10. Understanding that only M depends on \vec{r} , the result is

$$\langle \nu_1 \rangle = \frac{\langle M \rangle}{1 + \alpha \nu_{sf1}} \nu_{sf1} (1 + \alpha) \quad (5.14)$$

$$\langle \nu_2 \rangle = \frac{\langle M^2 \rangle \nu_{sf2}}{1 + \alpha \nu_{sf1}} + \frac{\langle M^3 \rangle - \langle M^2 \rangle}{(1 + \alpha \nu_{sf1})(\nu_{i1} - 1)} \nu_{sf1} (1 + \alpha) \nu_{i2} \quad (5.15)$$

$$\begin{aligned} \langle \nu_3 \rangle = & \frac{\langle M^3 \rangle \nu_{sf3}}{1 + \alpha \nu_{sf1}} + \left(\frac{\langle M^4 \rangle - \langle M^3 \rangle}{(1 + \alpha \nu_{sf1})(\nu_{i1} - 1)} \right) [3\nu_{sf2} \nu_{i2} + \nu_{sf1} (1 + \alpha) \nu_{i3}] \\ & + 3 \frac{\langle M^5 \rangle - 2\langle M^4 \rangle + \langle M^3 \rangle}{(1 + \alpha \nu_{sf1})(\nu_{i1} - 1)^2} \nu_{sf1} (1 + \alpha) \nu_{i2}^2 \end{aligned} \quad (5.16)$$

$$\text{with } \langle M^n \rangle = \frac{1}{V} \int M^n(\vec{r}) dV$$

Then, $\langle \nu_1 \rangle$ must be inserted for ν_1 in equation 2.20, $\langle \nu_2 \rangle$ for ν_2 in equation 2.21 and $\langle \nu_3 \rangle$ for ν_3 in equation 2.22. The result is identical to equation 5.12, where $M^n = \langle M \rangle^n$.

In the sub-sequent sub-sections, remaining issues related to this model will be discussed:

1. The corrected multiplicity equations must be derived to calculate M , α and m_{Pu} (sub-section 5.2.3).
2. It must be tested whether the g_n remove the bias. This would show whether the bias is caused by the spatially variant multiplication, see sub-section 5.2.4.
3. In order to increase the reliability for warhead and warhead component authentication, further simulations must be performed to find out how the g_n can be determined for solid and hollow spheres. The aim is to understand the g_n based on the physics of the samples, see sub-section 5.2.5.

5.2.3 Corrected multiplicity analysis

The derivation of the equations of the corrected multiplicity analysis based on equations 5.12 is provided in Appendix D. As a result, M can be calculated from solving the following equation:

$$\begin{aligned}
0 = f(M) &= \left[D - \frac{\epsilon \cdot f_d \cdot M \cdot \nu_{i2} \cdot S}{2(\nu_{i1} - 1)} (g_3 \cdot M - g_2) \right]^{-1} \cdot \\
&\quad (a \cdot M^6 + b \cdot M^5 + c \cdot M^4 + d \cdot M^3 + e \cdot M^2 + f \cdot M + g) \\
a &= -3g_3(g_2g_5 - g_3g_4) \cdot \epsilon^3 \cdot f_d^2 f_t \cdot \nu_{sf2} \nu_{i2}^3 \cdot S^2 \\
b &= -g_3 \cdot \epsilon^3 \cdot f_d^2 f_t \cdot \nu_{i2} \cdot S^2 \{g_2g_4 \cdot \nu_{sf2} \nu_{i3} (\nu_{i1} - 1) + \\
&\quad 3g_2g_4 \cdot \nu_{sf2} \nu_{i2}^2 + 3g_3^2 \cdot \nu_{sf2} \nu_{i2}^2 - 6g_2g_4 \cdot \nu_{sf2} \nu_{i2}^2 - g_3^2 \cdot \nu_{sf3} \nu_{i2} (\nu_{i1} - 1)\} + \\
&\quad 3g_2 \cdot \epsilon^3 \cdot f_d^2 f_t \cdot \nu_{sf2} \nu_{i2}^3 \cdot S^2 (g_2g_5 - g_3g_4) \\
c &= \epsilon^2 \cdot f_d f_t \cdot \nu_{i2} \cdot S \{6\nu_{sf2} \nu_{i2} (\nu_{i1} - 1) \cdot D (g_2g_5 - g_3g_4) - \\
&\quad g_3 [6g_4 \cdot \nu_{sf2} \nu_{i2} (\nu_{i1} - 1) \cdot D + g_2g_3 \cdot \epsilon \cdot f_d \cdot (\nu_{i1} - 1) \cdot S (\nu_{sf3} \nu_{i2} - \nu_{sf2} \nu_{i3})]\} + \\
&\quad g_2 \cdot \epsilon^3 \cdot f_d^2 f_t \cdot \nu_{i2} \cdot S^2 \{g_2g_4 \cdot \nu_{sf2} \nu_{i3} (\nu_{i1} - 1) + 3g_2g_4 \cdot \nu_{sf2} \nu_{i2}^2 + \\
&\quad 3g_3^2 \cdot \nu_{sf2} \nu_{i2}^2 - 6g_2g_4 \cdot \nu_{sf2} \nu_{i2}^2 - g_3^2 \cdot \nu_{sf3} \nu_{i2} (\nu_{i1} - 1)\} \\
d &= \epsilon^2 \cdot f_d f_t \cdot (\nu_{i1} - 1) \cdot S \{2D \cdot \\
&\quad [g_2g_4 \cdot \nu_{sf2} \nu_{i3} (\nu_{i1} - 1) + 3\nu_{sf2} \nu_{i2}^2 \cdot (g_3^2 - g_2g_4) - g_3^2 \cdot \nu_{sf3} \nu_{i2} (\nu_{i1} - 1)] - \\
&\quad 2g_3^2 \cdot \nu_{i2} \cdot D (\nu_{sf3} (\nu_{i1} - 1) - 3\nu_{sf2} \nu_{i2}) + g_2 \cdot \nu_{i2} \cdot \\
&\quad [6g_4 \cdot \nu_{sf2} \nu_{i2} \cdot D - g_2g_3 \cdot \epsilon \cdot f_d \cdot \nu_{sf2} \nu_{i3} \cdot S + g_2g_3 \cdot \epsilon \cdot f_d \cdot \nu_{sf3} \nu_{i2} \cdot S]\} \\
e &= 6g_2g_3 \cdot \epsilon \cdot f_d^2 \cdot \nu_{sf2} \nu_{i2} (\nu_{i1} - 1)^2 \cdot S \cdot T + 2 \cdot \epsilon \cdot f_t \cdot (\nu_{i1} - 1) \cdot D \cdot \{(\nu_{i1} - 1) \cdot \\
&\quad [6g_4 \cdot \nu_{sf2} \nu_{i2} \cdot D - g_2g_3 \cdot \epsilon \cdot f_d \cdot S (\nu_{sf2} \nu_{i3} - \nu_{sf3} \nu_{i2})] + \\
&\quad g_2g_3 \cdot \epsilon \cdot f_d \cdot \nu_{i2} \cdot S \cdot (\nu_{sf3} (\nu_{i1} - 1) - 3\nu_{sf2} \nu_{i2})\} \\
f &= -6g_2^2 \cdot \epsilon \cdot f_d^2 \cdot \nu_{sf2} \nu_{i2} (\nu_{i1} - 1)^2 \cdot S \cdot T + 4g_3 \cdot \epsilon \cdot f_t \cdot \nu_{sf3} (\nu_{i1} - 1)^3 \cdot D^2 - \\
&\quad 12g_3 \cdot \epsilon \cdot f_t \cdot \nu_{sf2} \nu_{i2} (\nu_{i1} - 1)^2 \cdot D^2 \\
g &= -12g_2 \cdot f_d \cdot \nu_{sf2} (\nu_{i1} - 1)^3 \cdot D \cdot T
\end{aligned} \tag{5.17}$$

$0 = f(M)$ can be numerically solved for M by Newton's method

$$M_{n+1} = M_n - \frac{f(M_n)}{f'(M_n)} \tag{5.18}$$

where the above equation is applied iteratively after an initial guess of M_1 until M_n

	1000 <i>g</i> solid sphere	6000 <i>g</i> hollow sphere
$\langle M^1 \rangle$	1.5878	1.9566
g_2	1.0068	1.0048
g_3	1.0215	1.0142
g_4	1.0441	1.0280
g_5	1.0751	1.0461

Table 5.3: M and g_n determined from equations 5.11 and 5.12, based on MCNPX-PoliMi simulations

is found with acceptable accuracy. $|M_{n+1} - M_n| < 10^{-9}$ has been used for this work. M can then be inserted into the following equations to obtain the other factors (see Appendix D):

$$F = \frac{2}{\epsilon^2 \cdot f_d \cdot M^2 \cdot \nu_{sf2} \cdot g_2} \left[D - \frac{\epsilon \cdot f_d \cdot M \cdot \nu_{i2} \cdot S}{2(\nu_{i1} - 1)} (g_3 \cdot M - g_2) \right] \quad (5.19)$$

$$\alpha = \frac{S}{F \cdot \epsilon \cdot M \cdot \nu_{sf1}} - 1$$

These calculations (equations 5.17, 5.18 and 5.19) have been implemented in a MATLAB script which has been used to obtain the following results. The equations have been tested against the Ispra measurement data (see sub-section 3.2), setting all $g_n = 1$ as all samples have low multiplication and small masses. $M_1 = 1.5$ has been chosen and identical results compared to the point model multiplicity analysis have been found.

5.2.4 Testing the analysis

The g_n of the 1000 *g* solid and the 6000 *g* hollow spheres have been calculated in order to test whether they remove the bias. Croft et al. [50] propose a polynomial fit to obtain the function $M(r)$ for the simulated data points (i.e. fission surfaces) in order to integrate it afterwards according to equation 5.11. The polynomial fit is, however, very volatile.⁶ A linear interpolation has yielded satisfactory results. This fit method has been implemented in the MATLAB script to calculate the g_n . Table 5.3 shows the results. The fitting process introduces an uncertainty which depends on how close the data points are. Due to a large density of data points, the

⁶For an acceptable fit, the fit function must be a third order polynomial; in this case, however, slight changes to the data points can have dramatic effects on the integral of the polynomial fit.

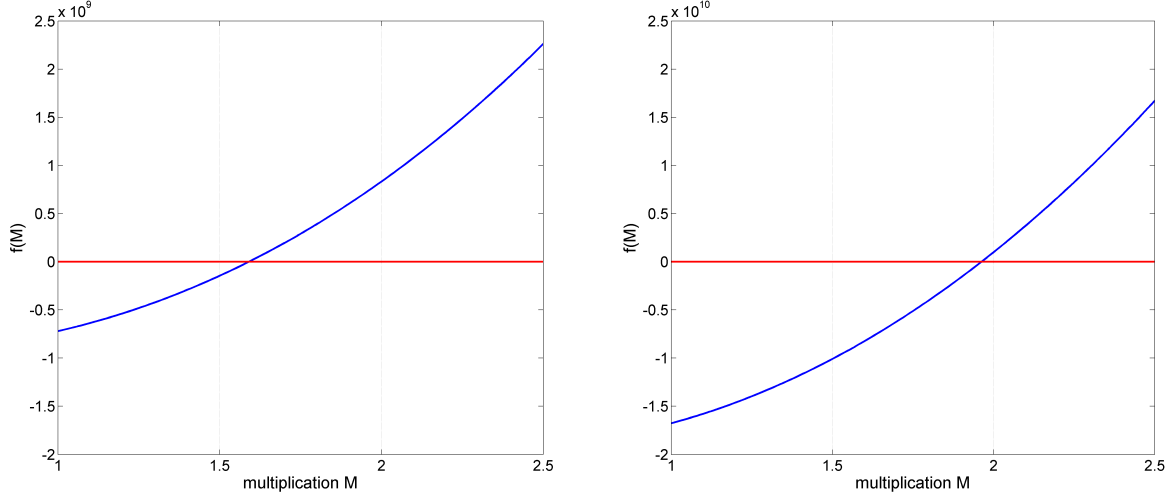


Figure 5.10: $f(M)$ (blue) for the 1000 g solid sphere (left) and 6000 g hollow sphere (right). The intersection of $f(M)$ and the zero line (red) is the solution M .

	M_{corr}	ΔM	$m_{Pu,corr}$	Δm_{Pu}
1000 g solid sphere	1.5902 ± 0.0005	$(0.18 \pm 0.03)\%$	1023 ± 5	$(2.30 \pm 0.50)\%$
6000 g hollow sphere	1.9627 ± 0.0006	$(0.26 \pm 0.03)\%$	6074 ± 33	$(1.23 \pm 0.55)\%$

Table 5.4: Results and their statistical uncertainties of the corrected multiplicity analysis (subscript *corr*) and the deviations to M_{true} and $m_{Pu,true}$

uncertainties of the data in Table 5.3 are estimated to be less than 3 %. The two $\langle M^1 \rangle$ values calculated from the integrated curves are very close to M_{true} of Fig. 5.2 which demonstrates the validity of the procedure.

Fig. 5.10 displays $f(M)$ (equation 5.17) calculated from the g_n . The corrected multiplicity analysis results are given in Table 5.4. All values lie slightly outside their statistical uncertainties, but remain small enough to be reasonably explained by the interpolation and the multiplicity uncertainties (sub-section 5.1.2). Mass deviations of -11.0 % and -7.7 % are reduced to 2.3 % and 1.2 %. The corrected multiplicity analysis has furthermore been conducted for all samples of Table 5.2 and additionally three hollow spheres series of the plutonium specified above with $r_{in} = 1.0 \text{ cm}$, 2.0 cm , 5.0 cm and different masses. The results of the point model analysis are qualitatively similar to those of Table 5.2. The corrected point model gives accurate results in all cases. The average values of the deviations between

multiplicity analysis and true simulated data from all simulations are

$$\begin{aligned}\Delta M &= (0.06 \pm 0.38)\% \\ \Delta m_{Pu} &= (0.38 \pm 1.30)\%\end{aligned}\tag{5.20}$$

Due to these results, it is concluded that spatially variant multiplication is indeed the main reason for the bias of the point model multiplicity analysis. The corrected multiplicity analysis as proposed by Croft et al. [50] is correct and generally works successfully.

5.2.5 Reducing the bias for warhead authentication

If the sample configuration is fully known, $M(r)$ can be obtained and the g_n can be accurately determined. In this sub-section, it is examined which physical factors the g_n depend on. The goal is the ability to determine the g_n from such factors without having to simulate the precise function $M(r)$. The discussion focuses on solid and hollow sphere geometries to ensure the direct relevance for warhead and warhead component authentication. In this case, the exact configuration of the fissile material will not be fully known. An example is that r_{in} and r_{out} may not be declared. Therefore, this sub-section also examines to which degree of accuracy the g_n can be determined only from parameters that are known or can be assessed. This would increase the reliability of neutron multiplicity counting for warhead and warhead component authentication.

In order to interpret simulation results, some considerations regarding the g_n follow first: g_2 and g_3 are related to the variance $\sigma^2(M)$ and the third central moment $\sigma^3(M)$:

$$\sigma^2(M) = \frac{1}{V} \int (M(\vec{r}) - \langle M \rangle)^2 dV \tag{5.21}$$

$$= \langle (M - \langle M \rangle)^2 \rangle = \langle M^2 \rangle - \langle M \rangle^2 \tag{5.22}$$

$$\begin{aligned}\sigma^3(M) &= \langle (M - \langle M \rangle)^3 \rangle \\ &= \langle M^3 \rangle - 3 \langle M \rangle \langle M^2 \rangle + 2 \langle M \rangle^3\end{aligned}\tag{5.23}$$

$$= \langle M^3 \rangle - 3 \langle M \rangle \cdot \sigma^2(M) - \langle M \rangle^3 \tag{5.24}$$

$$\implies g_2 = \frac{\langle M^2 \rangle}{\langle M \rangle^2} = \frac{\sigma^2(M) + \langle M \rangle^2}{\langle M \rangle^2} = \frac{\sigma^2(M)}{\langle M \rangle^2} + 1 \quad (5.25)$$

$$g_3 = \frac{\langle M^3 \rangle}{\langle M \rangle^3} = 1 + 3 \frac{\sigma^2(M)}{\langle M \rangle^2} + \frac{\sigma^3(M)}{\langle M \rangle^3} \quad (5.26)$$

where equations 5.22 and 5.23 are for instance derived in [51, p. 259]. Equations for g_4 and g_5 become increasingly complex. Equation 5.25 shows that $g_2 \geq 1$ because $\sigma^2(M) \geq 0$. From equation 5.26 it can be seen that $g_3 > g_2$ as $\sigma^3(M) \geq 0$. For larger variances $\sigma^2(M)$, larger corrections (g_2 and g_3) are required. In words, the square of a function is compared to the square of the function's average value. The difference between squares of function values above the average to the squared average will be larger than the difference between the squared average to the squares of function values below the average, hence positive g_2 . This explanation can be analogously applied to g_4 and g_5 with the fourth and fifth power.

Croft et al. [50] calculated correction factors from simulations of solid plutonium spheres and cylinders of different masses [50]. They propose a function based on their simulations which does not seem to be explicitly based on physical considerations :

$$g_{n,Croft} = a \cdot e^{b \cdot m_{Pu}} \quad (5.27)$$

For a range of solid spheres and cylinders, the fitting coefficients a and b are listed [50]. Simulations performed for this dissertation demonstrate, however, that the correction factors depend on the sample geometry and therefore the proposed fitting coefficients would need to be evaluated for each geometry individually: Fig. 5.11 shows the g_2 calculated from $M(r)$ which has been obtained from MCNPX-PoliMi simulations of all configurations addressed in the previous sub-section. Within the individual series ($r_{in} = const.$), increased masses result in increased g_2 as in $g_{n,Croft}$. The functions between the individual series, however, differ strongly. Appendix Fig. E.1, E.2 and E.3 show the according graphs $g_3(m_{Pu})$, $g_4(m_{Pu})$ and $g_5(m_{Pu})$. The g_n differ in magnitude, but their relative behavior for the different geometries is very similar for all g_n . All graphs show that expected uncertainties would be large when calculating g_n as a function of fissile mass without knowledge of r_{in} . The correction factors are related to $\sigma^2(M)$, $\sigma^3(M)$ etc. Accordingly, they depend on the

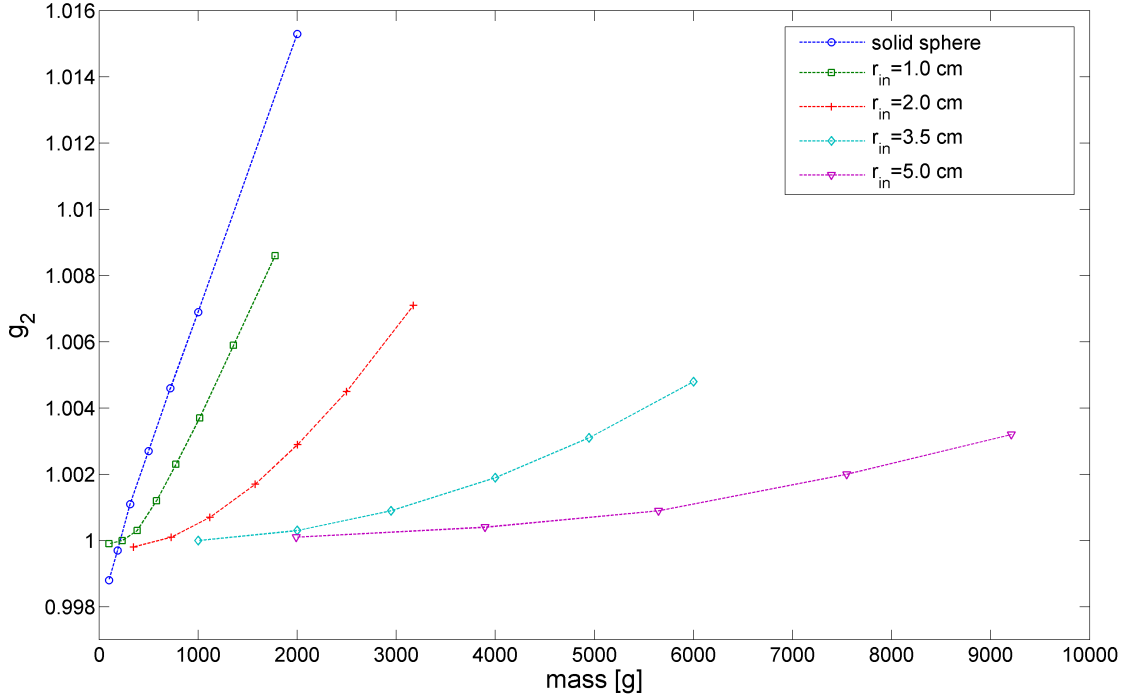


Figure 5.11: g_2 as a function of fissile mass for a range of simulations. Dots represent simulated configurations, the lines are for guiding the eyes only and connect simulations of the same same r_{in} .

specific function $M(r)$ which is only partially influenced by m_{Pu} . $g_{n,Croft}$ are very helpful if the appropriate information is available. Due to the particular challenge of warhead and warhead component authentication, where such information is likely not available, the $g_{n,Croft}$ should perhaps not be directly applied in this specific context.

A different parameter which $\sigma^2(M)$, $\sigma^3(M)$ etc. physically depend on should be identified so that the g_n could be determined from knowing or assessing this parameter. The dependence of the g_n on the thickness of the hollow spheres has been investigated (where in this dissertation the “thickness” of solid spheres refers to their radius): The multiplication increases with the amount of fissile material in the vicinity of the source location because $\int \Phi(\vec{r})dV$ increases (see sub-section 5.2.1). One can also explain the increased multiplication by a reduced neutron leakage due to these geometrical considerations. With this logic, the differences of multiplication at different radial locations in a hollow sphere increases with the thickness: The differences of the amounts of fissile material in vicinity of the source increases and so do the neutron leakage differences.⁷ Correspondingly, $\sigma^2(M)$ and $\sigma^3(M)$ grow.

⁷To understand this, one may consider two sources at $r_{in} + (r_{out} - r_{in})/2$ and r_{out} in Fig. 5.9 and the following simplified view: When increasing the thickness, for the former source the

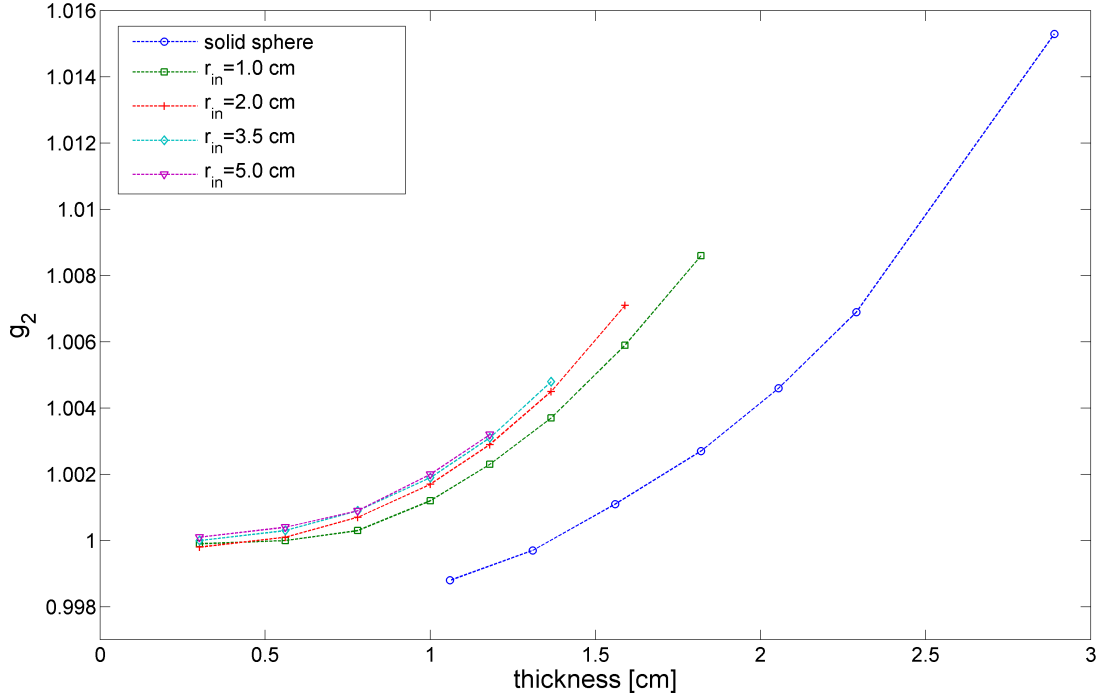


Figure 5.12: g_2 as a function of the thickness for a range of simulations. Dots represent simulated configurations, the lines are for guiding the eyes only and connect simulations of the same same r_{in} .

Fig. 5.12 shows g_2 as a function of thickness for the different geometries, based on simulation results. As above, the relative behavior of all g_n is very similar to the behavior of g_2 , see Appendix Fig. E.4, E.5 and E.6. Consistent with the logical explanation, the g_2 increase with thickness for all geometries. Fig. 5.13 shows that also the multiplication increases with thickness for all geometries. $\sigma^2(M)$ increases with a steeper slope than $\langle M \rangle^2$. This is evident from equation 5.25, but has also been confirmed by calculating $\sigma^2(M)$ for all geometries according to equation 5.21.

The most significant observation of Fig. 5.12 is that - with the exception of the solid spheres - all g_n are quantitatively very similar for all geometries (different r_{in}) of the same thickness. It follows from equations 5.25 and 5.26 that

$$d = const. \implies \begin{aligned} \frac{\sigma^2(M)}{\langle M \rangle^2} &\approx const. \\ \frac{\sigma^3(M)}{\langle M \rangle^3} &\approx const. \end{aligned} \quad (5.28)$$

contribution to $\int \Phi(\vec{r})dV$ increases both inwards and outwards, neutron leakage becomes smaller. For the latter source, $\int \Phi(\vec{r})dV$ increases only inwards, neutron leakage is reduced to a lesser extent. The difference between the two sources increases accordingly.

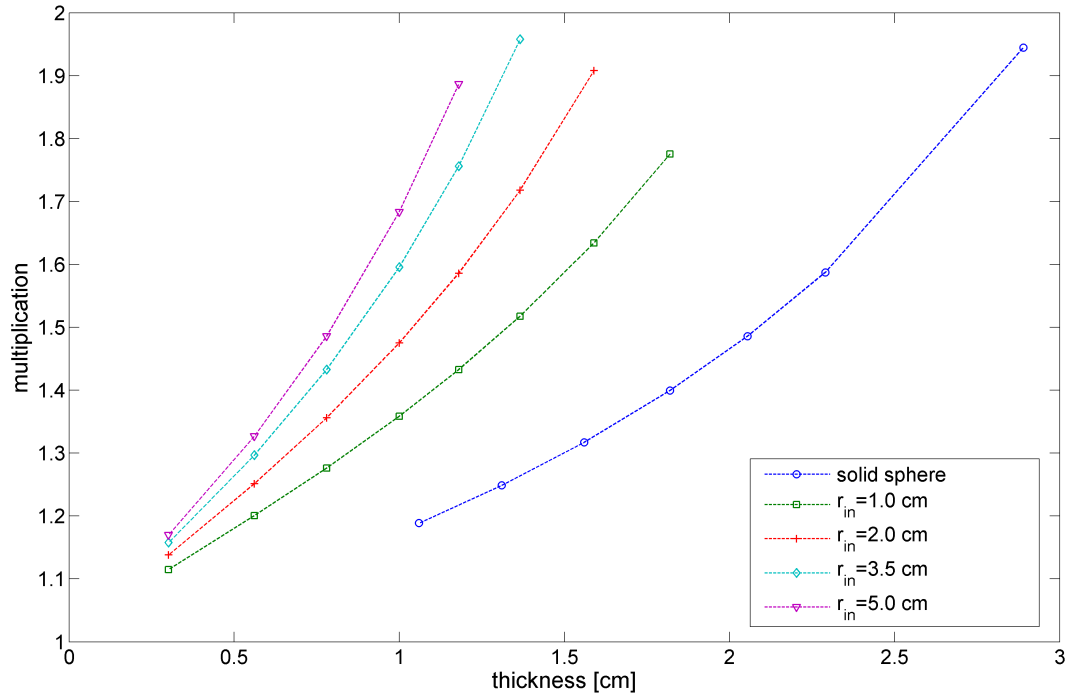


Figure 5.13: M as a function of the thickness for a range of simulations. Dots represent simulated configurations, the lines are for guiding the eyes only and connect simulations of the same same r_{in} .

for all hollow spherical geometries, where d is the thickness. M itself, however, is not constant for constant thickness, but increases with r_{in} , as Fig. 5.13 shows. Correspondingly, the same is true for $\sigma^2(M)$ and $\sigma^3(M)$. The reason is that the fissile material volume grows with r_{in} at the same thickness. $\int \Phi(\vec{r})dV$ over the fissile volume increases accordingly.

As only results for plutonium metals of the same isotopic composition were shown above, an oxide sample (solid sphere) has been simulated, see Table 5.5. The point model multiplicity analysis correctly predicts the true values within their statistical uncertainties. Oxides, in general, have a lower multiplication compared to metal samples of the same configuration mainly due to the reduced plutonium isotope density.⁸ The metal sample corresponding to the simulated oxide requires correction factors. Examining the influence of isotopic composition, the 6000 g hollow sphere has been simulated with different isotopic compositions, see Table 5.6. Together with Table 5.3 it can be seen that correction factors slightly increase with Pu-239 content. However, the influence is small compared to the influence of geometry.

The influence of oxides and isotopic composition on the m_{Pu} assessment further

⁸The density in the simulation has been chosen to be realistic for plutonium oxide [52, p. 1528]

R_{239}	94%
R_{240}	6%
ρ	10.4 g/cm ³
M_{true}	1.1518
$m_{Pu,true}$	231.64 g
M_{mult}	1.1519 ± 0.0002
α_{mult}	0.7193 ± 0.006
$m_{Pu,mult}$	231.1000 ± 0.8 g

Table 5.5: Characterization and simulated values of oxide sample (solid sphere)

R_{239}	R_{240}	g_2	g_3	g_4	g_5
0.70	0.30	1.0040	1.0118	1.0233	1.0383
0.85	0.15	1.0045	1.0133	1.0263	1.0433
0.97	0.03	1.0049	1.0146	1.0288	1.0474

Table 5.6: g_n calculated from MCNPX-PoliMi simulations of the 6000 g hollow sphere configuration and different isotopic compositions.

loses relevance in the context of authenticating plutonium warheads and warhead components: Items with large α would be rejected because warheads can be expected not to consist of plutonium oxide. Moreover, an isotopic composition threshold is usually considered as part of an information barrier; warheads with high Pu-240 content would also be rejected so that no neutron multiplicity measurement would need to be conducted. Accordingly, neutron multiplicity measurements must be accurate mainly for weapon-grade metals.

If the thickness was known and whether the fissile pit was solid or hollow, the correct g_n could be determined with a high degree of accuracy, independent of further information: For example, a reasonable estimate could be obtained by using the g_n values for $r_{in} = 2.0$ cm hollow sphere. Table 5.7 shows that applying these correction factors to other hollow sphere configurations of the same thickness introduces deviations below 1 % in the fissile mass assessments - in contrast to applying the point model with much larger uncertainties. The assessment was performed using configurations with different r_{in} and $d = const. = 1$ cm. This thickness was chosen because the differences between the correction factors of the different r_{in} seems to be roughly an average value compared to the differences at other thicknesses, see Fig. 5.12. The differences do not appear to be significantly larger for large thicknesses so that it can be concluded that the high degree of accuracy is obtained for all reasonable configurations. Accordingly, the plutonium mass could be adequately determined, keeping in mind remaining uncertainties discussed in section 5.1. The

	$r_{in} = 1.0 \text{ cm}$	$r_{in} = 3.5 \text{ cm}$	$r_{in} = 5.0 \text{ cm}$
M_{true}	1.3587	1.5955	1.6835
$m_{Pu,true}$ [g]	580.6	4000.0	7547.4
M_{point}	1.3697 \pm 0.0002	1.6115 \pm 0.0006	1.7023 \pm 0.0004
ΔM [%]	0.8 \pm 0.01	1.0 \pm 0.04	1.1 \pm 0.02
$m_{Pu,point}$ [g]	563 \pm 1	3851 \pm 20	7230 \pm 24
Δm_{Pu} [%]	-3.0 \pm 0.2	-3.7 \pm 0.5	-4.2 \pm 0.3
M_{fit}	1.3593 \pm 0.0002	1.5998 \pm 0.0006	1.6900 \pm 0.0004
ΔM [%]	0.04 \pm 0.01	0.3 \pm 0.04	0.4 \pm 0.02
$m_{Pu,fit}$ [g]	581 \pm 1	3982 \pm 20	7487 \pm 24
Δm_{Pu} [%]	0.1 \pm 0.2	-0.5 \pm 0.5	-0.8 \pm 0.3

Table 5.7: Multiplicity analysis results using the point model (subscript *point*) and the corrected model with the g_n from the $r_{in} = 2.0 \text{ cm}$ data (subscript *fit*), the true simulated values (subscript *true*) and the deviations of the simulated from the true values for different hollow spheres with $d = 1.0 \text{ cm}$

thickness would need to be determined with appropriate measurements behind an information barrier so that the measurement result can be used in the analysis without being known to an inspector. Information on a solid or hollow configuration could be declared by the host.⁹ As the determination of g_n from the thickness is based on physical understanding and as it mainly depends on parameters that are known, the accuracy and reliability would be high in the context of warhead authentication.

However, measuring the thickness is a technical challenge requiring further research and might be impossible for political reasons. An estimate on the correction factors can also be obtained from the sample multiplication. It is a direct output of the multiplicity analysis and therefore available information. Fig. 5.14 shows that slopes of $g_2(M)$ are somewhat steeper for smaller r_{in} because the thickness is larger at the same multiplication, see Fig. 5.13. In contrast to $g_2(m_{Pu})$, however, the slopes only differ somewhat. In particular when a differentiation between solid and hollow spheres is possible, estimates for g_2 can be obtained. This logic extends to all other g_n , see Appendix Fig. E.7, E.8 and E.9. The uncertainties of the g_n determined this way are larger than if they were determined from the thickness, but smaller than for $g_{n,Croft}$.

Depending on the available information on the configuration, different g_n estimates would be chosen. As an example, $g_n(M)$ for $r_{in} = 2 \text{ cm}$ may be a reasonable

⁹A decision to declare this would need to be consistent with the Non-Proliferation Treaty's Articles I and II.

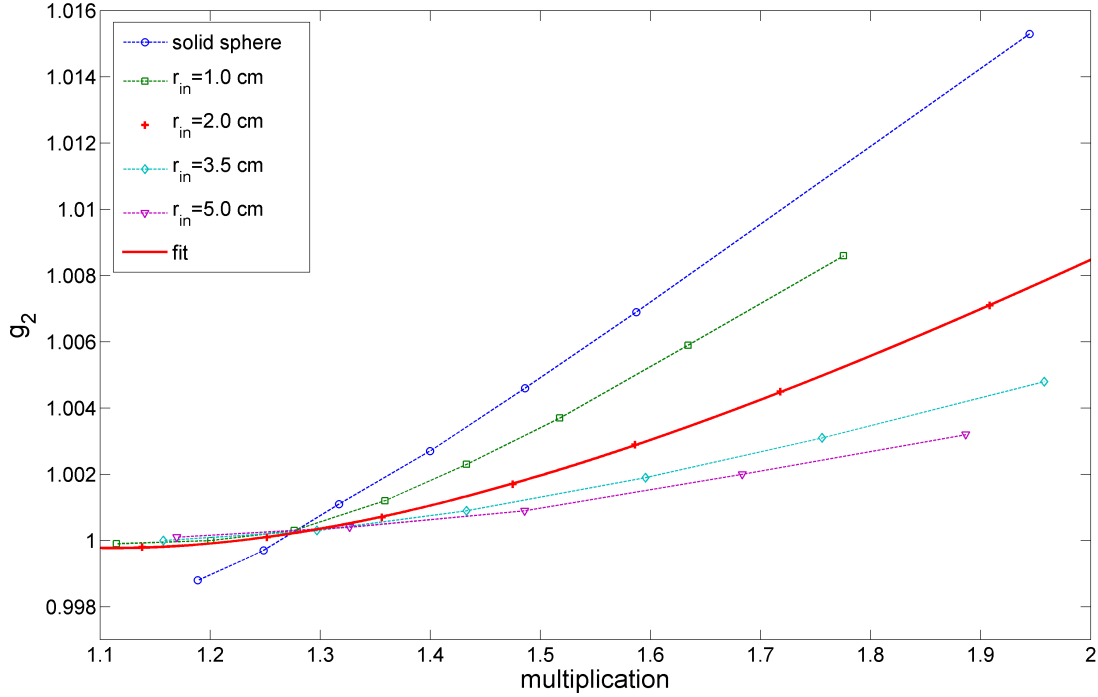


Figure 5.14: g_2 as a function of M for a range of simulations. Dots represent simulated configurations, the dotted lines are for guiding the eyes only and connect simulations of the same same r_{in} , the solid red line is an empirical fit to the $r_{in} = 2.0 \text{ cm}$ data.

	a	b	c	d
$g_2(M)$	0.087	-2.093	0.972	0.018
$g_3(M)$	0.193	-1.434	0.897	0.062
$g_4(M)$	0.396	-1.872	0.848	0.103
$g_5(M)$	0.694	-2.049	0.777	0.161

Table 5.8: Parameters for fit function (equation 5.29)

reference curve when a hollow sphere is assumed and r_{in} remains unknown. Different fit functions have been tested using MATLAB; the best functions that have been found (shown in Fig. 5.14, E.7, E.8 and E.9) are

$$g_n(M) = \begin{cases} 1 & M < 1.1 \\ a \cdot \exp(b \cdot M) + c \cdot \exp(d \cdot M) & M > 1.1 \end{cases} \quad (5.29)$$

with the parameters from Table 5.8. They are purely empirical. The shapes of the curves are physically understood and the dependence on unavailable information is limited but existent. Therefore, this procedure appears acceptable and remains a

	$r_{in} = 1.0 \text{ cm}$	$r_{in} = 3.5 \text{ cm}$	$r_{in} = 5.0 \text{ cm}$
M_{true}	1.7755	1.9577	1.8864
$m_{Pu,true}$ [g]	1777.0	6000.0	9208.5
M_{point}	1.8318 \pm 0.0004	1.9966 \pm 0.0006	1.9156 \pm 0.0006
ΔM [%]	3.2 \pm 0.02	1.99 \pm 0.03	1.5 \pm 0.03
$m_{Pu,point}$ [g]	1564 \pm 6	5541 \pm 32	8664 \pm 48
Δm_{Pu} [%]	-12.0 \pm 0.3	-7.7 \pm 0.5	-5.9 \pm 0.5
M_{fit}	1.7969 \pm 0.0004	1.9422 \pm 0.0006	1.8698 \pm 0.0006
ΔM [%]	1.2 \pm 0.02	-0.8 \pm 0.03	-0.9 \pm 0.03
$m_{Pu,fit}$ [g]	1720 \pm 6	6378 \pm 34	9754 \pm 50
Δm_{Pu} [%]	-3.2 \pm 0.3	6.3 \pm 0.6	5.9 \pm 0.5

Table 5.9: Multiplicity analysis results using the point model (subscript *point*) and the corrected model with the g_n from the reference curves $g_n(M)$ (subscript *fit*), the true simulated values (subscript *true*) and the deviations of the simulated from the true values for different hollow spheres

better option compared to $g_{n,Croft}$ for solid and hollow spheres. Table 5.9 compares the results of the multiplicity analysis using the point model and the fit function for all considered hollow sphere geometries that have the highest multiplication. For these configurations, the correction factors deviate the most from the fit function as seen in Fig. 5.14. Therefore, the deviations of the fit function analysis to the true data are expected to be large. Correspondingly, the data represents a pessimistic estimate. Still, the results show that the fit function tends to improve the results of M and m_{Pu} compared to the point model analysis. Hence, this approach can be recommended, although uncertainties may remain large for unfavorable conditions. The more information were available on the configuration, the more could uncertainties be further reduced due to the reduced variability of possible correction factors and accordingly a better fit function.

5.3 Bias from Reflected Configurations

A fully assembled warhead contains at the minimum the conventional explosive. It may also have a neutron reflector such as beryllium and further materials [48]. Due to safety reasons, warheads and warhead components are usually stored in appropriate containers which inter alia consists of materials such as Celotex or polyurethane [53]. Conventional explosives, Celotex and polyurethane contain hydrogen and carbon besides others. Effects in such materials are neutron moderation by elastic scattering and to a lesser extent absorption reactions. (n, γ) is the absorption re-

action with the largest cross-section in hydrogen and carbon [10]. These effects influence ϵ , f_d and f_t (see sub-section 5.1).

Additionally, neutrons are reflected back to the sample where they can undergo additional reactions. Corresponding effects in the fissile material are studied in this section in order to examine the g_n for reflected configurations. To focus on this, the “idealistic detector” has been used where $f_d = f_t = 1$ as the gate length remains sufficiently long. There is no influence of the energy spectrum on ϵ with the “idealistic detector”, but absorption in the material between fissile sample and detector must be taken into account. Therefore, ϵ is determined for every simulation individually so that no uncertainty is introduced. Simulations were conducted with the 1000 g solid sphere and 6000 g hollow sphere introduced in section 5.2 with a 3 cm thick layer of polyethylene ($\rho = 0.955 \text{ g/cm}^3$) directly surrounding the fissile material. Consisting of hydrogen and carbon, polyethylene is suited to represent the materials above in regard to the neutron interactions, and the quality of the simulations is provided as simulations with polyethylene have been tested against experimental data (chapter 4).

Fig. 5.15 and 5.16 show the spatial neutron flux density distributions of a slice through the two configurations which have been simulated with MCNPX-PoliMi. Comparing them to the unreflected configurations (Fig. 5.2 and 5.3), the general shape of the distributions are rather similar. However, the flux density of the reflected configurations is significantly higher: For the reflected solid sphere, the maximum flux density is $\Phi_{max} = 15300 \text{ cm}^{-2}\text{s}^{-1}$ (compared to $\Phi_{max} = 12600 \text{ cm}^{-2}\text{s}^{-1}$ for the unreflected case); for the hollow sphere, it is $\Phi_{max} = 29900 \text{ cm}^{-2}\text{s}^{-1}$ (compared to $\Phi_{max} = 15700 \text{ cm}^{-2}\text{s}^{-1}$ for the unreflected case). The flux density increase comes both directly from reflected neutrons and from further induced fission, i.e. increased multiplication. It is much larger for the hollow sphere configuration which indicates that more neutrons are reflected. The simulations show that 11.4% of all neutrons leaving the fissile material are reflected back for the solid sphere configurations and 19.5% for the hollow sphere configuration. This is consistent with geometrical considerations: The ratio of inner ($= r_{out}$) to outer surface of the polyethylene volume is larger for the hollow sphere. Hence, the probability that neutrons that entered the polyethylene leave in the direction of the fissile material is larger.

Fig. 5.17 shows the energy distribution of neutrons at various radii of the solid sphere obtained from simulations. The distributions have been normalized in such a way that the integrals of the spectra correspond to the rate of neutrons passing through

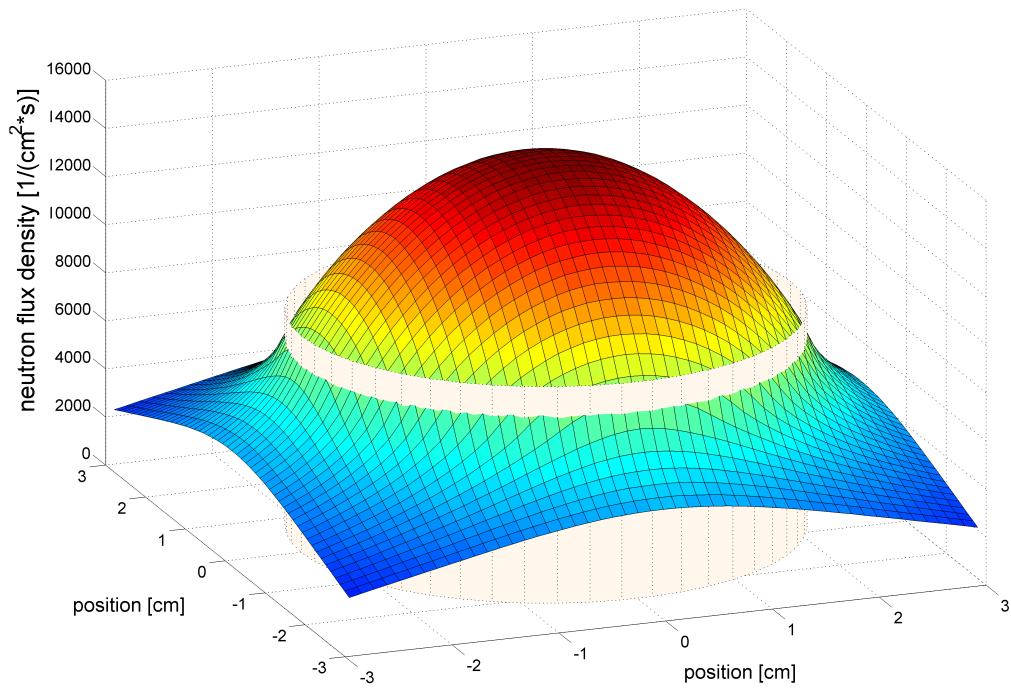


Figure 5.15: Neutron flux density of the 1000 *g* solid sphere surrounded by polyethylene. The cylinder marks r_{out} .

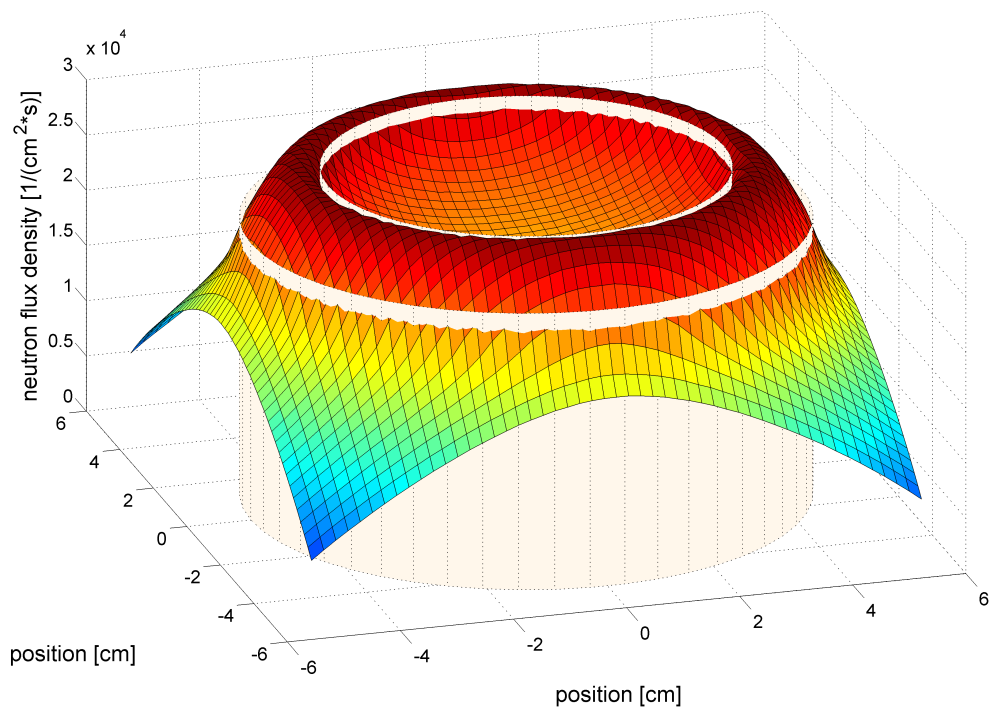


Figure 5.16: Neutron flux density of the 6000 *g* hollow sphere surrounded by polyethylene. The cylinder mark r_{in} and r_{out} .

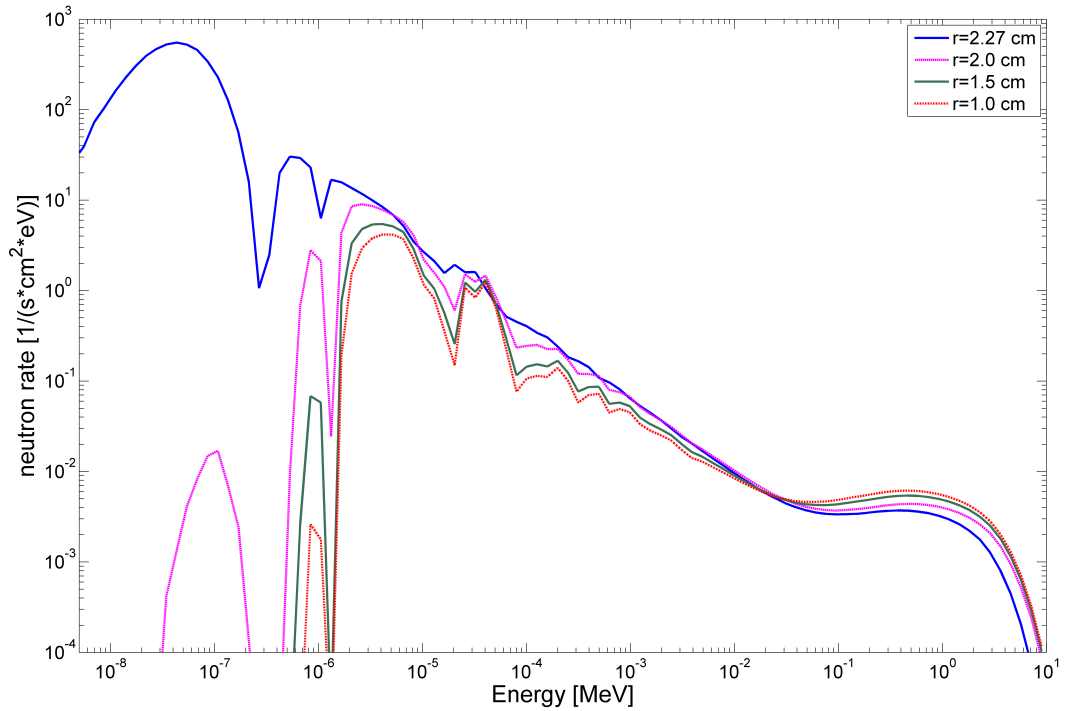


Figure 5.17: Energy distribution of neutrons passing through spherical surfaces (see indicated radii) within the 1000 g solid sphere

a 1 cm^2 surface. At all radii, the neutron spectra have a neutron fission spectrum component with some influence from inelastic scattering (compare to Fig. 2.3), but furthermore a lower energy component which is due to the reflected neutrons. The dips in the spectra are the result of Pu-239 resonances, see Fig. 2.1. With increasing radii, the ratio of neutrons with energies below 100 keV to energies above 100 keV increases. As the fission cross-section of Pu-239 increases with decreasing energy, the mean free path becomes much shorter and the reflected neutrons are absorbed at larger radii. In particular thermal neutrons do not penetrate the volume: 0.025 eV neutrons have a mean free path of 0.02 cm in plutonium metal [10]. At $r = 2.0 \text{ cm}$ the flux density of neutrons below 0.1 eV is more than four orders of magnitudes smaller compared to $r = 2.27 \text{ cm}$. From induced fission by reflected moderated neutrons, additional fast neutrons occur. Accordingly, also the fast neutron flux density increases with reflection. The simulation shows that more than 90% of all neutrons have energies above 100 keV at all radii and accordingly long mean free paths. This explains the similarity between the spatial flux density distribution shapes of the reflected configurations (Fig. 5.15 and 5.16) and their unreflected counterparts. The qualitative results are also valid for the hollow sphere. Due to the larger polyethylene volume for the hollow sphere configuration, simulations show

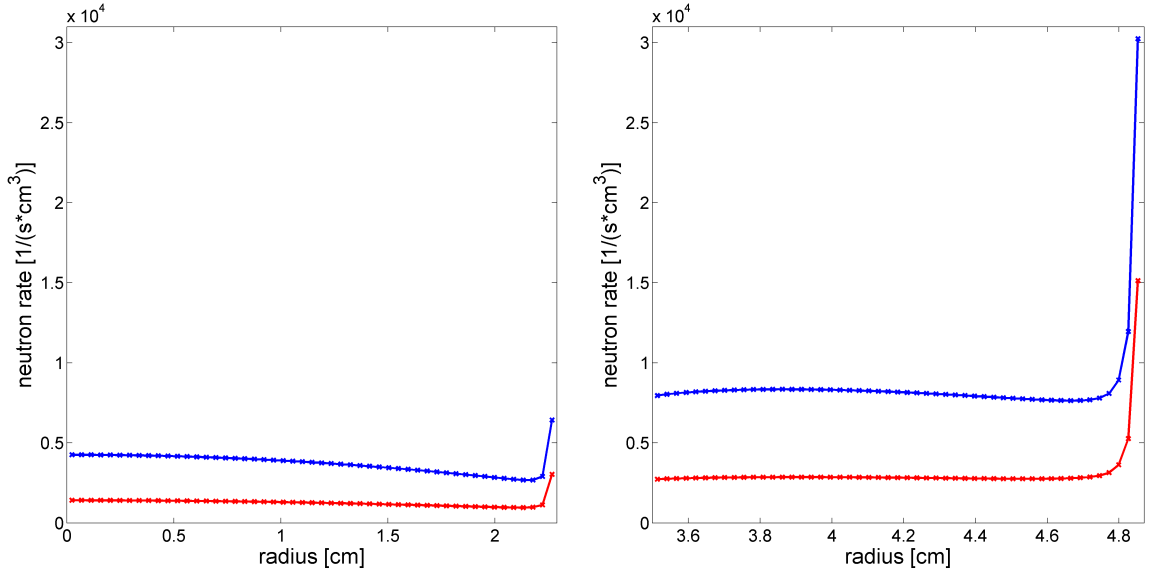


Figure 5.18: $P(r)$ (blue) and $A(r)$ (red) for the reflected 1000 g solid sphere (left) and the reflected 6000 g hollow sphere (right), lines are for guiding the eyes

that the lower energy contributions are larger compared to the solid sphere.

The neutron production and absorption rates $P(r)$ and $A(r)$ (see equations 5.6 and 5.7) of the reflected solid and hollow spheres as obtained from simulations are shown in Fig. 5.18. They sharply increase towards r_{out} due to the presence of thermal neutrons and the according high cross-sections. It is more pronounced for the hollow sphere as the amount of thermal neutrons is larger. Apart from that, the curves are qualitatively similar to the unreflected configurations (Fig. 5.4). Quantitatively, the rates are significantly larger. This is the direct consequence of the lower neutron energy component and the higher neutron fluxes of the reflected solid sphere and to an even larger extent of the hollow sphere.

5.3.1 Correction factors

The dependence of the multiplication on the radius $M(r)$ has been investigated to study the correction coefficients g_n , see Fig. 5.19. The curve shapes of the reflected configurations are somewhat similar to the shapes of the unreflected configurations, the slopes of the reflected configurations are slightly steeper. The multiplication of the reflected configurations is generally higher. The increased multiplication is the result of the larger neutron production rates. The more neutrons leave the

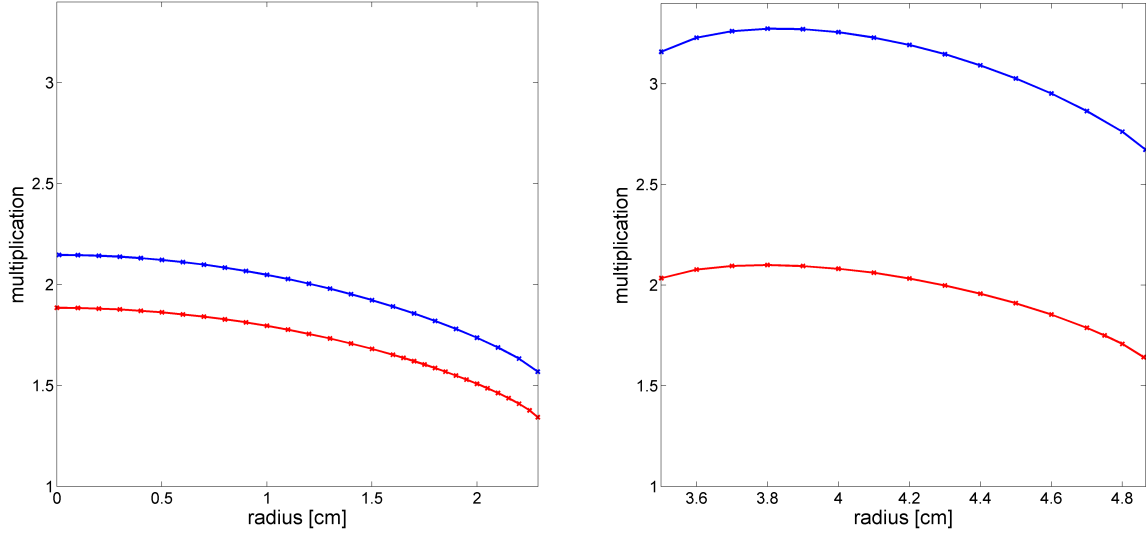


Figure 5.19: Multiplication as a function of spontaneous fission source radius for the 1000 *g* solid sphere (left) and the 6000 *g* hollow sphere. The reflected configurations (blue) are compared to the unreflected configurations (red).

	reflected 1000 <i>g</i> solid sphere	reflected 6000 <i>g</i> hollow sphere
$\langle M^1 \rangle$	1.8233	3.0873
g_2	1.0059	1.0033
g_3	1.0187	1.0098
g_4	1.0385	1.0193
g_5	1.0656	1.0319

Table 5.10: M and g_n determined from equations 5.11 and 5.12, based on MCNPX-PoliMi simulations

fissile material to enter the polyethylene, the more are also reflected back to induce further fission. Therefore, high multiplication data points of the unreflected $M(r)$ distribution will increase to a larger extent when adding polyethylene. This explains the slightly increased steepness.

Table 5.10 shows the correction factors. They can be compared to the unreflected configurations (Table 5.3). For both the solid and hollow spheres, all correction factors of the reflected configurations are somewhat smaller than for the unreflected configurations. It can be explained by equations 5.25 and 5.26: While the reflected curves are steeper and accordingly $\sigma^2(M)$ and $\sigma^3(M)$ are larger, also $\langle M \rangle^2$ and $\langle M \rangle^3$ are larger as can be seen from Fig. 5.19. The increase of $\langle M \rangle^2$ and $\langle M \rangle^3$ is greater than the increase of $\sigma^2(M)$ and $\sigma^3(M)$.

	reflected 1000 g solid sphere	reflected 6000 g hollow sphere
M_{true}	1.8357	3.1074
$m_{Pu,true}$ [g]	1000	6000.0
M_{mult}	1.8711 \pm 0.0002	3.1653 \pm 0.0006
ΔM [%]	1.9	1.9
$m_{Pu,mult}$ [g]	921 \pm 2	5623 \pm 28
Δm_{Pu} [%]	-7.9	-6.3
M_{corr}	1.8683 \pm 0.0002	3.1291 \pm 0.0005
ΔM [%]	1.8	0.7
$m_{Pu,corr}$ [g]	979 \pm 2	6166 \pm 28
Δm_{Pu} [%]	-2.1	2.8
$M_{corr,unrefl}$	1.8181 \pm 0.0002	3.1139 \pm 0.0005
ΔM [%]	-1.0	-0.2
$m_{Pu,corr,unrefl}$ [g]	1068 \pm 2	6393 \pm 29
Δm_{Pu} [%]	6.8	6.6

Table 5.11: Multiplicity analysis results using the point model (subscript *mult*), the corrected model with the correct g_n (subscript *corr*) and the g_n of the unreflected configurations (subscript *corr,unrefl*). The true simulated values (subscript *true*) and the deviations of the multiplicity analyses results from the true values are given.

In order to conduct the multiplicity analysis, the detection efficiencies have been obtained from the MCNPX-PoliMi output. They are $\epsilon = 0.979$ for the reflected solid sphere and $\epsilon = 0.974$ for the reflected hollow sphere. The ν_{in} have been calculated from equations 5.2 and 5.3. $W(E)$ has been obtained from MCNPX-PoliMi simulations of the two configurations. The results for the reflected solid and hollow spheres are

$$\begin{aligned}
\text{solid} : \quad \nu_{i1} &= 3.160 & \nu_{i2} &= 8.267 & \nu_{i3} &= 17.555 \\
\text{hollow} : \quad \nu_{i1} &= 3.140 & \nu_{i2} &= 8.127 & \nu_{i3} &= 16.037
\end{aligned} \tag{5.30}$$

With these parameters, the corrected multiplicity analysis has been performed, see Table 5.11. Compared to the point model multiplicity analysis, the results are much better. M is somewhat overestimated, m_{Pu} is somewhat underestimated for the solid and overestimated for the hollow sphere. There does not appear to be a physical reason introducing bias and the deviations are small enough to assume the same uncertainties as for the unreflected configurations (see sub-section 5.2.4). The table also shows the results of applying the “false” g_n of the unreflected configurations. In

this case, the fissile masses are overestimated by over 6%. Uncertainties could therefore be reduced if information regarding materials between plutonium and detector were available¹⁰, otherwise increased uncertainties must be taken into account.

¹⁰A decision to declare this would need to be consistent with the Non-Proliferation Treaty's Article VI.

Chapter 6

Conclusions and Implications

The motivation of this work has been the finding that there was very little research investigating proposed measurement techniques suggested for warhead authentication in regard to reducing false assessments. An example is the false assessment of a plutonium mass threshold which can be considered an attribute for an information barrier. This can occur when neutron multiplicity measurement results include large bias. It is essential for an inspecting party to trust the functionality of a system which is achieved by reducing false positives and false negatives to acceptable levels. Warheads and warhead components differ from most samples of Safeguards interest, for which sufficient knowledge and experience in regard to neutron multiplicity counting exists. Hence, this work has focused on plutonium metals in spherical geometries with large masses. It has identified sources of bias in neutron multiplicity counting when measuring such items. It has also developed methods to reduce this bias in order to minimize false positives and false negatives.

Specifically, two types of bias have been identified: First, inadequate knowledge of detector calibration parameters on the one hand and inadequate knowledge of nuclear data required for the multiplicity analysis (ν_{in}) on the other hand introduce bias. It has been physically understood by previous research. This type of bias can be reduced when certain information regarding the configuration of the samples to be measured is known. Then, the detector calibration can be performed with representative standards. As the available information regarding warheads and warhead components will be very limited, though, increased uncertainties need to be taken into account.

Due to the second type of bias, it has been shown that plutonium masses of relevant configurations (solid and hollow spheres) are underestimated by as much as 20% using the established analysis method. The reason is a false assumption used in the derivation of the neutron multiplicity counting theory: Contrary to this assumption that the multiplication M is a constant parameter, it depends on the position \vec{r} of the spontaneous fission source. By introducing correction factors which are calculated from the function $M(\vec{r})$, the erroneous assumption can be corrected. When the sample configuration is known, the correction factors can be determined accurately by simulating the sample configuration and obtaining $M(\vec{r})$ with Monte-Carlo codes such as MCNPX-PoliMi. Simulations have showed that the use of these correction factors fully removes the bias.

If the configuration is not fully known and $M(\vec{r})$ cannot be determined, the correction factors must be approximated based on the available information. When assuming a hollow plutonium sphere, it has been physically argued and tested in the dissertation that the correction factors can be approximated by a function of the hollow sphere thickness. They only show a very small dependence on the inner (or outer) radius and a small dependence on the plutonium isotopic composition. Therefore, it has been concluded that the correction factors, and accordingly the plutonium mass, can be determined with good accuracy when the thickness is known. It is estimated that not knowing the radius introduces an uncertainty of less than 1% which is negligible.

If the thickness remains unknown, an estimate of the correction factors can be obtained from the multiplication M which is known from the multiplicity analysis. When describing the correction factors as a function of M , the slopes of the curves for different radii differ, though their variation remains limited. Therefore, a less accurate estimate of the correction factors based on M is possible. In this case, a reference curve must be chosen. One can expect to reduce bias by applying this procedure compared to the “point model” even when no information on the radii exists. If upper and/or lower bounds of possible radii can be given, the accuracy of the correction factors is further enhanced as a better reference curve can be chosen.

Bias can also be removed to a large extent if the correction factors can be exactly determined for reflected configurations. It has been found that the correction factors are somewhat smaller for the considered configurations when reflection is presented compared to the bare warhead components.

Overall, bias will remain for warhead authentication as the configuration of the warheads and warhead components will not be fully known. Accordingly, there can be mis-classifications. Their rate, however, can be decreased as bias can be reduced by using the proposed correction factors. Moreover, by having critically evaluated expected bias, the research also provides means for discussing the reliability of neutron multiplicity measurements to assess a plutonium mass threshold attribute. Whether the reliability obtained with the corrected approach suffices depends on various factors:

First, this work shows that the accuracy can be enhanced by obtaining certain information on the fissile material configuration and/or material between the plutonium and detector. A precise analysis of the reliability depends on the amount of available information. Accordingly, the inspecting party should negotiate a maximum of information compatible with the Non-Proliferation Treaty Articles I and II.

Second, the functionality of the warhead authentication depends on the determination of all attributes, the fissile mass being one of them. Neutron multiplicity counting is an important part of the warhead authentication system, but not the only one. Most measurement techniques produce false positives and negatives and it is the wise combination of different techniques that increase confidence. Accordingly, some limited amount of neutron multiplicity counting bias may be acceptable on the one hand. On the other hand, as the confidence gained from an authentication concept should be maximized in any case, one must strive to enhance the reliability of all elements. As a small amount of failures of the entire authentication system may perhaps not be excluded, further verification opportunities must be used to obtain high overall confidence. Their discussion puts the results of this dissertation into the overall context of disarmament verification:

Warhead authentication must be understood in the context of the other two verification requirements, unique identification and Continuity of Knowledge. To provide an illustration, one imagine that an object looking like a warhead situated on a delivery vehicle was uniquely identified and that there is confidence in the Continuity of Knowledge of the transfer of this object to a dismantlement facility. Knowing that this object presented in the dismantlement facility was previously deployed provides an initial level of confidence that this object is a nuclear warhead, already before it has been authenticated. If all obtained information produce a coherent picture without contradictions or anomalies, it can be concluded that a state is compliant, even with limited uncertainties in the individual verification measures. Problems arise,

however, when anomalies are observed or results are inconclusive. For such cases, platforms for discussing and resolving them are required; the inspected state may be able to reasonably clarify potential issues. Drawing a conclusion on the obtained level of confidence requires expert judgment based on all available evidence.

References

- [1] Russian Federation and United States of America, *Treaty between the United States and the Russian Federation on measures for the further reduction and limitation of strategic offensive arms* (2010).
- [2] Nuclear Threat Initiative, *Innovating Verification: New Tools & New Actors to Reduce Nuclear Risks, Verifying Baseline Declarations of Nuclear Warheads and Materials* (2014).
- [3] International Panel on Fissile Materials, *Global Fissile Material Report 2008: Scope and Verification of a Fissile Material (Cutoff) Treaty* (2008).
- [4] Fissile Material Transparency Technology Demonstration, “Technical overview of Fissile Material Transparency Technology Demonstration, executive summary,” retrieved 21/01/2015, http://www.lanl.gov/orgs/n/n1/FMTTD/presentations/pdf_docs/exec_sum.pdf.
- [5] L.R. Avens, J.E. Doyle, and M.F. Mullen, “The fissile material transparency technology demonstration,” LA-UR-01-3570, Los Alamos National Laboratory (2001).
- [6] D. Langner, S.-T. Hsue, D.W. MacArthur, T.B. Gosnell, Z. Koenig, J. Wolford, M. Aparo, I. Kulikov, J. Puckett, Whichello J, S. Razinkov, A. Livke, and V.J. Poplavko, “Attribute verification systems with information barriers for classified forms of plutonium in the Trilateral Initiative,” in *IAEA Symposium on International Safeguards* (Vienna, 2001).
- [7] S. Kondratov, M. Bulatov, D. Decman, M. Leplyavkina, A. Livke, S.J. Luke, D. MacArthur, S. Razinkov, D. Sivachev, J. Thron, S. Tsybryaev, and A. V’yushin, “AVNG system demonstration,” in *51st INMM Annual Meeting* (Baltimore, 2010).

- [8] C.F. von Weizsäcker, “Zur Theorie der Kernmassen,” *Zeitschrift für Physik* **96**, 431–458 (1935).
- [9] H.A. Bethe and R.F. Bacher, “Nuclear physics A. Stationary states of nuclei,” *Reviews of Modern Physics* **8**, 82–229 (1936).
- [10] M.B. Chadwick, M. Herman, P. Obložinsky, M.E. Dunn, Y. Danon, A.C. Kahler, D.L. Smith, B. Pritychenko, G. Arbanas, R. Arcilla, R. Brewer, D.A. Brown, R. Capote, A.D. Carlson, Y.S. Cho, H. Derrien, K. Guber, G.M. Hale, S. Hoblit, S. Holloway, T.D. Johnson, T. Kawano, B.C. Kiedrowski, H. Kim, S. Kunieda, N.M. Larson, L. Leal, J.P. Lestone, R.C. Little, E.A. McCutchan, R.E. MacFarlane, M. MacInnes, C.M. Mattoon, R.D. McKnight, S.F. Mughabghab, G.P.A. Nobre, G. Palmiotti, A. Palumbo, M.T. Pigni, V.G. Pronyaev, R.O. Sayer, A.A. Sonzogni, N.C. Summers, I.J. Thompson, P. Talou, A. Trkov, R.L. Vogt, S.C. van der Marck, A. Wallner, and M.C. White, “ENDF/B-VII.1 nuclear data for science and technology: Cross sections, covariances, fission product yields and decay data,” *Nuclear Data Sheets* **112**, 2887–2996 (2011).
- [11] P.M.J. Chard, S. Croft, M. Looman, P. Peerani, H. Tagziria, M. Bruggeman, and A.-L. Weber, “A good practice guide for the use of modelling codes in non destructive assay of nuclear materials,” *ESARDA Bulletin* **42**, 26–69 (2009).
- [12] F. Zeiser, “Theory of fission neutron multiplicities and implementation in mcnp-polimi,” Bachelor thesis, Universität Hamburg (2013).
- [13] V. Weisskopf, “Statistics and nuclear reactions,” *Physical Review* **52**, 295–303 (1937).
- [14] B.E. Watt, “Energy spectrum of neutrons from thermal fission of U-235,” *Physical Review* **87**, 1037–1041 (1952).
- [15] X-5 Monte Carlo Team, “MCNP - a general monte carlo n-particle transport code, version 5,” LA-UR-03-1987, Los Alamos National Laboratory (2003).
- [16] J. Terrell, “Distributions of fission neutron numbers,” *Physical Review* **108**, 783–789 (1957).
- [17] P. Santi and M. Miller, “Reevaluation of prompt neutron emission multiplicity distributions for spontaneous fission,” *Nuclear Science and Engineering* **168**, 190–199 (2008).
- [18] M.S. Zucker and N.E. Holden, “Energy dependence of the neutron multiplicity

- P(v) in fast neutron induced fission of U-235, U-238, and Pu-239,” in *1986 American Nuclear Society Annual Meeting* (Reno, 1986).
- [19] D. Reilly, N. Ensslin, Jr. H. Smith, and S. Kreiner, *Passive Nondestructive Assay of Nuclear Materials* (U.S. Government Printing Office, Washington, 1991).
- [20] S. Croft, “The calculation of the enhancement of the (alpha,n) production rate in PuO₂ and MOX powders caused by the presence of moisture,” in *17th ESARDA Annual Meeting* (Aachen, 1995).
- [21] N. Ensslin, W.C. Harker, M.S. Krick, D.G. Langner, M.M. Pickrell, and J.E. Stewart, “Application guide to neutron multiplicity counting,” LA-13422-M, Los Alamos National Laboratory (1998).
- [22] L.C.-A. Bourva and S. Croft, “Monte carlo calculations of the neutron coincidence gate utilisation factor for passive neutron coincidence counting,” *Nuclear Instruments and Methods in Physics Research A* **431**, 485–508 (1999).
- [23] I. Pazsit, A. Enqvist, and L. Pal, “A note on the multiplicity expressions in nuclear safeguards,” *Nuclear Instruments and Methods in Physics Research A* **603**, 541–544 (2009).
- [24] R. Dierckx and W. Hage, “Neutron signal multiplet analysis for the mass determination of spontaneous fission isotopes,” *Nuclear Science and Engineering* **85**, 325–338 (1983).
- [25] W. Hage and D.M. Cifarelli, “Correlation analysis with neutron count distributions in randomly or signal triggered time intervals for assay of special fissile materials,” *Nuclear Science and Engineering* **89**, 159–176 (1985).
- [26] D.M. Cifarelli and W. Hage, “Models for a three-parameter analysis of neutron signal correlation measurements for fissile material assay,” *Nuclear Instruments and Methods in Physics Research A* **251**, 550–563 (1986).
- [27] K. Böhnelt, “The effect of multiplication on the quantitative determination of spontaneously fissioning isotopes by neutron correlation analysis,” *Nuclear Science and Engineering* **90**, 75–82 (1985).
- [28] M.M. Pickrell, A.D. Lavietes, V. Gavron, D. Henzlova, H.O. Menlove, J. Joyce, and R.T. Kouzes, “The IAEA workshop on requirements and potential technologies for replacement of He-3 detectors in IAEA safeguards applications,” *Journal of Nuclear Materials Management* **41** (2), 14–29 (2013).
- [29] M. Götttsche and G. Kirchner, “Measurement techniques for warhead authenti-

- cation with attributes: Advantages and limitations,” *Science & Global Security* **22**, 83–110 (2014).
- [30] Canberra, “PSMC-01 - Plutonium Scrap Multiplicity Counter,” retrieved 21/01/2015, www.canberra.com/products/waste_safeguard_systems/pdf/PSMC-01-SS-C40093.pdf.
- [31] P.V. Federov, P. Peerani, B. Pedersen, and M. Marin Ferrer, “Calibration procedures for the Plutonium Scrap Multiplicity Counter,” unpublished (2005).
- [32] S.A. Pozzi, S.D. Clarke, W. Walsh, E. Miller, J. Dolan, M. Flaska, B. Wieger, A. Enqvist, E. Padovani, J.K. Mattingly, D. Chichester, and P. Peerani, “MCNPX-PoliMi for nuclear nonproliferation applications,” *Nuclear Instruments and Methods in Physics Research A* **694**, 119–125 (2012).
- [33] D.B. Pelowitz, “MCNPX user’s manual, version 2.7.0,” LA-CP-11-00438, Los Alamos National Laboratory (2011).
- [34] S. Pozzi, E. Padovani, and M. Marseguerra, “MCNP-PoliMi: A monte-carlo code for correlation measurements,” *Nuclear Instruments and Methods in Physics Research, Section A* **513**, 550–558 (2003).
- [35] E. Padovani, S.A. Pozzi, S.D. Clarke, and E.C. Miller, “Introduction to MCNPX-PoliMi,” MCNPX-PoliMi v. 2.0 Manual (2012).
- [36] R.E. MacFarlane, “New thermal neutron scattering files for ENDF/B-VI release 2,” LA-12639-MS, Los Alamos National Laboratory (1994).
- [37] J.U. Koppel and D.H. Houston, “Reference manual for ENDF thermal neutron scattering data,” ENDF-269, Brookhaven National Laboratory (1978).
- [38] D. Sprevak and J.U. Koppel, “Neutron scattering by polyethylene,” *Nukleonik* **12**, 87–92 (1969).
- [39] M.S. Zucker and N.E. Holden, “Parameters of several plutonium nuclides and Cf-252 of safeguards interest,” in *6th ESARDA Annual Meeting* (Venice, 1984).
- [40] W. Harker and M. Krick, “Multiplicity neutron coincidence counting user’s manual,” LA-UR-93-1394, Los Alamos National Laboratory (1993).
- [41] N. Dytlewski, M.S. Krick, and N. Ensslin, “Measurement variances in thermal neutron coincidence counting,” *Nuclear Instruments and Methods in Physics Research A* **327**, 469–479 (1993).
- [42] K.D. Böhnel, *Die Plutoniumbestimmung in Kernbrennstoffen mit der Neutro-*

- nenkoinzidenzmethode*, Ph.D. thesis, Universität Karlsruhe (1975).
- [43] S. Croft, M.T. Swinhoe, and V. Henzl, “A priori precision estimation for neutron triples counting,” in *2nd ANIMMA Conference* (Ghent, 2011).
- [44] M.S. Krick, D.G. Langner, and J.E. Stewart, “Energy-dependent bias in plutonium verification measurements using thermal neutron multiplicity counters,” LA-UR-97-3427, Los Alamos National Laboratory (1997).
- [45] S.A. Pozzi, S.D. Clarke, W. Walsh, E. Miller, J. Dolan, B. Wieger, M. Flaska, A. Enqvist, S. Naeem, J. Mattingly, N. Puppato, E. Padovani, and P. Peerani, “MCNPX-PoliMi for the simulation of the neutron and gamma ray emissions from nuclear fission,” in *53rd INMM Annual Meeting* (Orlando, 2012).
- [46] P. Peerani and A.-L. Weber, “Analysis of uncertainties affecting the monte carlo simulation of a neutron multiplicity counter,” *Radiation Measurements* **47**, 475–480 (2012).
- [47] P. Santi, S. Croft, L.J. Dowell, A. Favalli, D.K. Hauck, V. Henzl, D. Henzlova, M. Swinhoe, and L.G. Worrall, “The development of advanced processing and analysis algorithms for improved neutron multiplicity measurements,” in *2014 IAEA Symposium on International Safeguards* (Vienna, 2014).
- [48] S. Fetter, V.A. Frolov, M. Miller, R. Mozley, O.F. Prilutsky, S.N. Rodionov, and R.Z. Sagdeev, “Detecting nuclear warheads,” *Science & Global Security* **1**, 225–253 (1990).
- [49] M.S. Krick, W.H. Geist, and D.R. Mayo, “A weighted point model for the thermal neutron multiplicity assay of high-mass plutonium samples,” LA-14157, Los Alamos National Laboratory (2005).
- [50] S. Croft, E. Alvarez, P.M.J. Chard, R.D. McElroy, and S. Philips, “An alternative perspective on the weighted point model for passive neutron multiplicity counting,” in *48th INMM Annual Meeting* (Tucson, 2007).
- [51] C.P. Tsokos, *Probability Distributions: An Introduction to Probability Theory with Applications* (Duxbury Press, Belmont, 1972).
- [52] D.G. Cacuci, *Handbook of Nuclear Engineering: Nuclear Engineering Fundamentals* (Springer, New York, 2010).
- [53] L. Hansen, “A comparison of the shielding performances of the AT-400A, model FL and model AL-R8 containers,” UCRL-JC-120849, Lawrence Livermore National Laboratory (1995).

- [54] M.M.R. Williams, *The Slowing Down and Thermalization of Neutrons* (North-Holland Publishing Company, Amsterdam, 1966).
- [55] D.E. Parks, M.S. Nelkin, J.R. Beyster, and N.F. Wikner, *Slow Neutron Scattering and Thermalization* (W.A. Benjamin Inc. Publishers, New York, 1970).
- [56] W. Marshall and S.W. Lovesey, *Theory of Thermal Neutron Scattering* (Clarendon Press, Oxford, 1971).

Appendix A

Elements of the Mathematical Formalism of Neutron Multiplicity Counting

A.1 The Multiplicity Distribution of Emitted Neutrons

The following derivation of the multiplicity distribution of emitted neutrons in section A.1 fully follows Böhnel [27] using probability generating functions (PGF) which are defined as

$$f(u) = \sum_{n=0}^{\infty} p(n)u^n \quad (\text{A.1})$$

where $p(n)$ is the probability of obtaining the variable n . The following properties of the PGF will be used in the course of the derivation:

1) The derivatives of $f(u)$ at $u = 1$ yield the factorial moments, which are defined as

$$\begin{aligned} \frac{df(u)}{du} \Big|_{u=1} &= \sum_{n=0}^{\infty} np(n) = \mathbf{n}_1 \\ \frac{d^2f(u)}{du^2} \Big|_{u=1} &= \sum_{n=0}^{\infty} n(n-1)p(n) = \mathbf{n}_2 \\ \frac{d^i f(u)}{du^i} \Big|_{u=1} &= \sum_{n=0}^{\infty} n(n-1)\dots(n-i+1)p(n) = \mathbf{n}_i \end{aligned} \quad (\text{A.2})$$

2) When $f_1(u)$ and $f_2(u)$ are PGFs of two independent variables \mathbf{n}_1 and \mathbf{n}_2 , the PGF of their sum is

$$f(u) = f_1(u) \cdot f_2(u) \quad (\text{A.3})$$

3) Let $g_k(u)$ be the PGF with the conditional probabilities $p(n | k)$ that the variable will become n under condition k . With the probability of condition k being P_k , the PGF for quantity n without conditions is

$$f(u) = \sum_{\text{all } k} p(n | k) P_k = p(n) \quad (\text{A.4})$$

With $f_s(u)$ being the PGF for the number of neutrons from a source event (spontaneous fission or (α, n) reaction) and $f_i(u)$ the PGF for the number of neutrons from induced fission, one obtains

$$f_s(u) = \sum_{k=0}^{\infty} P_s(k) u^k \quad (\text{A.5})$$

$$f_i(u) = \sum_{k=0}^{\infty} P_i(k) u^k \quad (\text{A.6})$$

Let $h_1(u)$ denote the PGF for the number of neutrons from the first and following generations that leave the system when one initial neutron is present. Then, assuming n initial neutrons, the PGF can be expressed using property 2):

$$h_n(u) = [h_1(u)]^n \quad (\text{A.7})$$

A neutron in a system can induce fission producing k neutrons with the probability $p \cdot P(k)$ or leave the system with probability $1 - p$. Using property 3), the PGF for one initial source neutron can be expressed in terms of p :

$$h_1(u) = (1 - p)u + \sum_{k=0}^{\infty} p \cdot P_i(k) \cdot h_k(u) \quad (\text{A.8})$$

By applying equation [A.7](#) and comparing it to equation [A.6](#) one obtains an implicit equation that contains only basic constants in addition to the PGF $h_1(u)$ for the prediction of the consequences of one initial source neutron:

$$h_1(u) = (1 - p)u + p \cdot \sum_{k=0}^{\infty} P_i(k) (h_1(u))^k = (1 - p)u + p \cdot f_i[h_1(u)] \quad (\text{A.9})$$

where $f_i[h_1(u)]$ is the PGF of the PGF $h_1(u)$. After having derived the PGF for one initial neutron, the PGF for a general source event is now introduced as

$$H(u) = \sum_{k=0}^{\infty} P(k)u^k \quad (\text{A.10})$$

where $P(k)$ without subscript describes the probability that k neutrons leave the sample after multiplication as a consequence of one source event. With equations 2.5 and A.5 as well as property 3) it becomes

$$H(u) = f_s[h_1(u)] = \frac{N_\alpha}{R_s} \cdot h_1(u) + \frac{F}{R_s} \cdot f_{sf}[h_1(u)] \quad (\text{A.11})$$

where $f_{sf}[h_1(u)]$ is the PGF for the number of neutrons after a spontaneous fission event including multiplication. Equations A.9 and A.11 are the basic equations that will yield the factorial moments of the ‘‘superfission’’ multiplicity distribution. According to property 1), these are the derivatives of $H(u)$. All derivatives are calculated in detail by Böhnel [27], the final results using equation 2.6 are

$$\nu_1 = \frac{dH}{du} \Big|_{u=1} = M\nu_{s1} = \frac{M}{1 + \alpha\nu_{sf1}} \nu_{sf1}(1 + \alpha) \quad (\text{A.12})$$

$$\begin{aligned} \nu_2 &= \frac{d^2H}{du^2} \Big|_{u=1} = M^2 \left\{ \nu_{s2} + \left(\frac{M-1}{\nu_{i1}-1} \right) \nu_{s2}\nu_{i2} \right\} \\ &= \frac{M^2}{1 + \alpha\nu_{sf1}} \left\{ \nu_{sf2} + \left(\frac{M-1}{\nu_{i1}-1} \right) \nu_{sf1}(1 + \alpha)\nu_{i2} \right\} \end{aligned} \quad (\text{A.13})$$

$$\begin{aligned} \nu_3 &= \frac{d^3H}{du^3} \Big|_{u=1} = M^3 \left\{ \nu_{s3} + \left(\frac{M-1}{\nu_{i1}-1} \right) [3\nu_{s2}\nu_{i2} + \nu_{s1}\nu_{i3}] + 3 \left(\frac{M-1}{\nu_{i1}-1} \right)^2 \nu_{s1}\nu_{i2}^2 \right\} \\ &= \frac{M^3}{1 + \alpha\nu_{sf1}} \left\{ \nu_{sf3} + \left(\frac{M-1}{\nu_{i1}-1} \right) [3\nu_{sf2}\nu_{i2} + \nu_{sf1}(1 + \alpha)\nu_{i3}] \right. \\ &\quad \left. + 3 \left(\frac{M-1}{\nu_{i1}-1} \right)^2 \nu_{sf1}(1 + \alpha)\nu_{i2}^2 \right\} \end{aligned} \quad (\text{A.14})$$

where ν_{sn} are the factorial moments of the general source multiplicity distribution, ν_{sfn} are the factorial moments of the spontaneous fission multiplicity distributions, ν_{in} are the factorial moments of the induced fission multiplicity distribution and ν_n are the factorial moments of the ‘‘superfission’’ multiplicity distribution.

A.2 The Multiplicity Distribution of Detected Neutrons

Above, the first three factorial moments of the multiplicity distribution of emitted neutrons have been derived. Here it is described how the detection efficiency

transforms this distribution to the distribution of neutrons from one “superfission” measured by the detector $D(n)$ [24]:

$$D(n) = \sum_{\nu=n}^{max} P(\nu) \binom{\nu}{n} \epsilon^n (1 - \epsilon)^{\nu-n} \quad (\text{A.15})$$

where $P(\nu)$ is the distribution of emitted neutrons from a “superfission”. All emitted events with $\nu \geq n$ contribute to the probability of detecting n neutrons, where the probability of detecting n out of ν emitted neutrons depends on the detection efficiency ϵ .

The mean of this distribution can be derived by using the expectation value of the binomial distribution $\sum_{k=0}^n k \binom{n}{k} \epsilon^k (1 - \epsilon)^{n-k} = n\epsilon$ and becomes [21]

$$\sum_{n=0}^{max} n D(n) = \epsilon \nu_1 \quad (\text{A.16})$$

Similarly, it can be shown that [27]

$$\sum_{n=0}^{max} n(n-1) D(n) = \epsilon^2 \nu_2 \quad (\text{A.17})$$

$$\sum_{n=0}^{max} n(n-1)(n-2) D(n) = \epsilon^3 \nu_3 \quad (\text{A.18})$$

These values are the factorial moments of detected neutrons from one “superfission” event. Even though these are principally detected, further aspects must be considered to understand the counting mechanism, see the next sub-section.

A.3 The Multiplicity Distribution of Detected and Counted Neutrons

Unless otherwise stated below, section A.3 follows the derivation in [21]. Besides the detection efficiency, the multiplicity distribution obtained from the gate measurements (i.e. detected and counted neutrons) depends on how these gates function. Their principal mechanism is explained in section 2.2. The multiplicity distribution of detected and counted neutrons first depends on whether there is a trigger to open the gate and second on how many of the neutrons are then detected within the finite gate length.

The probability of detecting one of the emitted neutrons from one “superfission” event which would trigger a gate between t and $t + dt$ is $nf(t)dt$. $f(t)$ is the neutron signal distribution. The probability of then detecting one of the remaining $(n - 1)$ neutrons within the time interval of the open gate is given by

$$p_t = \int_{t+PD}^{t+PD+G} f(s)ds \quad (\text{A.19})$$

The probability of obtaining a trigger and then counting i of the $(n - 1)$ neutrons of the same event is

$$p_{t,i} = n \int_0^{\infty} f(t) \binom{n-1}{i} p_t^i (1-p_t)^{n-1-i} dt \quad (\text{A.20})$$

which is the probability of obtaining a trigger and the appropriate binomial distribution.

With this, the multiplicity distribution $r(i)$, which refers to the detected and counted neutrons from one “superfission”, can be defined. It is obtained by summing over all possible numbers of detected neutrons n (the maximum i is $(n - 1)$, which is equal to n ranging from $(i + 1)$ to a maximum N). Therefore, within the sum, $D(n)$ is multiplied by the probability of obtaining a trigger and the probability of counting i of the $(n - 1)$ neutrons (equation A.20):

$$r(i) = \sum_{n=i+1}^N \frac{D(n) \cdot n}{\epsilon \nu_1} \int_0^{\infty} f(t) \binom{n-1}{i} p_t^i (1-p_t)^{n-1-i} dt \quad (\text{A.21})$$

The denominator $\epsilon \nu_1$ is the normalization factor which is obtained by applying equation A.16, so that the zeroth moment $r_0 = 1$. The normalization is necessary as it will be required at a later step of the derivation.

To calculate the first factorial moment of this distribution, the expectation value of the binomial distribution is used (equation A.16), which can be rearranged as

$$\sum_{i=0}^{n-1} i \binom{n-1}{i} p_t^i (1-p_t)^{n-1-i} = (n-1)p_t \quad (\text{A.22})$$

In addition to applying equation A.17 and some algebraic operations, one obtains

$$\mathbf{r}_1 = \sum_{i=1}^{N-1} i \cdot r(i) = \frac{\epsilon^2 \nu_2}{\epsilon \nu_1} \int_0^{\infty} f(t) \cdot p_t dt \quad (\text{A.23})$$

Similarly, using equation A.18 for the second factorial moment one obtains

$$\mathbf{r}_2 = \sum_{i=1}^{N-1} i(i-1) \cdot r(i) = \frac{\epsilon^3 \nu_3}{\epsilon \nu_1} \int_0^{\infty} f(t) \cdot p_t^2 dt \quad (\text{A.24})$$

In order to solve the integrals of these two equations, an assumption must be made for the neutron signal distribution $f(t)$. [21] and [25] assume that it has a single exponential die-away with the time constant τ after a rise during the predelay. One finds that

$$\mathbf{r}_1 = \frac{\epsilon f_d \cdot \nu_2}{2\nu_1} \quad (\text{A.25})$$

$$\mathbf{r}_2 = \frac{\epsilon^2 f_t \cdot \nu_3}{3\nu_1} \quad (\text{A.26})$$

$$\text{with } f_d = e^{-PD/\tau}(1 - e^{-G/\tau}) \quad (\text{A.27})$$

$$f_t = f_d^2 \quad (\text{A.28})$$

A.4 Solving S , D and T

The equations for S , D and T (2.25, 2.26 and 2.27) can be solved for the unknown parameters [21]. For M , the following cubic equation with its parameters a , b and c needs to be solved:

$$a + bM + cM^2 + M^3 = 0 \quad (\text{A.29})$$

$$a = \frac{-6T\nu_{sf2}(\nu_{i1} - 1)}{\epsilon^2 f_t S(\nu_{sf2}\nu_{i3} - \nu_{sf3}\nu_{i2})} \quad (\text{A.30})$$

$$b = \frac{2D[\nu_{sf3}(\nu_{i1} - 1) - 3\nu_{sf2}\nu_{i2}]}{\epsilon f_d S(\nu_{sf2}\nu_{i3} - \nu_{sf3}\nu_{i2})} \quad (\text{A.31})$$

$$c = \frac{6D\nu_{sf2}\nu_{i2}}{\epsilon f_d S(\nu_{sf2}\nu_{i3} - \nu_{sf3}\nu_{i2})} - 1 \quad (\text{A.32})$$

After M has been determined, F and α can be obtained:

$$F = \frac{\frac{2D}{\epsilon f_d} - \frac{M(M-1)\nu_{i2}S}{\nu_{i1}-1}}{\epsilon M^2 \nu_{sf2}} \quad (\text{A.33})$$

$$\alpha = \frac{S}{F \epsilon \nu_{sf1} M} - 1 \quad (\text{A.34})$$

Appendix B

Measurements and Simulations

	Pu mass [g]	diameter [mm]	length [mm]	isotopic comp. [wt% Pu_{tot}]
PM1	12.5	7.5	15.5	^{238}Pu : 0.004 ^{239}Pu : 95.420 ^{240}Pu : 4.529 ^{241}Pu : 0.032 ^{242}Pu : 0.015 ^{241}Am : 0.245
PM2	18.8	10.0	13.2	^{238}Pu : 0.004 ^{239}Pu : 95.493 ^{240}Pu : 4.455 ^{241}Pu : 0.033 ^{242}Pu : 0.015 ^{241}Am : 0.235
PM3	18.9	10.45	10.45	^{238}Pu : 0.025 ^{239}Pu : 91.358 ^{240}Pu : 8.468 ^{241}Pu : 0.102 ^{242}Pu : 0.047 ^{241}Am : 0.895

Table B.1: Characteristics of measured metal samples (personal communication Dr. Paolo Peerani)

	Pu mass [g]	diameter [mm]	length [mm]	isotopic comp. [wt% Pu_{tot}]
PERLA PuO_2 10	1.987	13	4	^{238}Pu : 0.058 ^{239}Pu : 86.082 ^{240}Pu : 13.270 ^{241}Pu : 0.321 ^{242}Pu : 0.270 ^{241}Am : 1.483
PERLA PuO_2 20	4.983	13	8	same as PuO_2 10
PERLA PuO_2 21	9.967	13	15	same as PuO_2 10
PERLA PuO_2 22	19.919	13	30	same as PuO_2 10
PERLA PuO_2 23	20.566	13	34	^{238}Pu : 0.084 ^{239}Pu : 70.906 ^{240}Pu : 26.856 ^{241}Pu : 0.691 ^{242}Pu : 1.463 ^{241}Am : 4.878
CBNM 61	5.547	14.75	3.75	^{238}Pu : 1.028 ^{239}Pu : 65.837 ^{240}Pu : 26.698 ^{241}Pu : 2.020 ^{242}Pu : 4.418 ^{241}Am : 6.357
CBNM 70	5.635	14.75	3.75	^{238}Pu : 0.720 ^{239}Pu : 76.442 ^{240}Pu : 19.036 ^{241}Pu : 1.634 ^{242}Pu : 2.167 ^{241}Am : 5.137
CBNM 84	5.851	14.75	3.75	^{238}Pu : 0.058 ^{239}Pu : 84.995 ^{240}Pu : 14.289 ^{241}Pu : 0.297 ^{242}Pu : 0.361 ^{241}Am : 0.931
CBNM 93	5.829	14.75	3.75	^{238}Pu : 0.010 ^{239}Pu : 93.575 ^{240}Pu : 6.312 ^{241}Pu : 0.064 ^{242}Pu : 0.040 ^{241}Am : 0.257

Table B.2: Characteristics of measured oxide samples (personal communication Dr. Paolo Peerani)

sample		measured [1/s]	σ_{stat} [%]	simulated [1/s]	σ_{stat} [%]	deviation [%]
Cf-252	S	2884.0	0.1	2835.4	0.1	-1.7
	D	1547.0	0.2	1606.5	0.2	3.8
	T	470.0	0.5	519.2	0.5	10.5
PM1	S	360.2	0.5	342.2	0.1	-5.0
	D	137.9	0.5	136.5	0.2	-1.0
	T	42.2	1.1	41.5	0.5	-1.8
PM2	S	542.2	0.2	514.8	0.1	-5.1
	D	212.9	0.5	216.0	0.2	1.5
	T	69.7	1.7	74.0	0.5	6.1
PM3	S	1091.7	0.2	988.9	0.1	-9.4
	D	414.0	0.5	426.0	0.2	2.9
	T	133.8	1.3	154.3	0.3	15.3
PERLA PuO_2 10	S	250.6	0.1	258.0	0.1	2.9
	D	50.6	0.7	51.9	0.3	2.4
	T	10.2	1.7	10.2	0.8	-0.4
PERLA PuO_2 20	S	654.2	0.1	652.2	0.1	-0.3
	D	134.9	0.3	136.0	0.3	0.8
	T	29.9	1.3	28.6	0.6	-4.3
PERLA PuO_2 21	S	1329.1	0.0	1316.6	0.1	-0.9
	D	281.5	0.1	283.1	0.3	0.6
	T	66.9	0.4	63.6	0.7	-5.0
PERLA PuO_2 22	S	2685.6	0.1	2687.1	0.1	0.1
	D	584.0	0.2	582.7	0.3	-0.2
	T	147.2	1.3	137.2	0.9	-6.8
PERLA PuO_2 23	S	5819.5	0.1	5571.5	0.1	-4.3
	D	1205.9	0.3	1218.7	0.3	1.1
	T	285.6	0.3	280.2	1.0	-1.9
CBNM 61	S	2287.5	0.2	2216.1	0.1	-3.1
	D	393.6	0.2	406.6	0.4	3.3
	T	84.0	0.5	93.2	1.0	11.0
CBNM 70	S	1684.0	0.1	1631.5	0.1	-3.1
	D	272.4	0.5	279.8	0.4	2.7
	T	59.7	1.4	64.4	1.0	7.9
CBNM 84	S	768.4	0.2	779.8	0.1	1.5
	D	168.0	0.6	184.1	0.2	9.6
	T	35.6	1.8	42.6	0.6	19.9
CBNM 93	S	392.0	0.1	386.2	0.1	-1.5
	D	72.7	0.2	80.4	0.2	10.7
	T	15.7	0.4	18.8	0.6	19.9

Table B.3: Comparison of measured Singles, Doubles and Triples rates to the corresponding simulated values for all samples including the deviation between simulation and measurement. Statistical uncertainties are given for the measured and simulated values.

Appendix C

The Thermal Neutron Scattering Kernel

A general quantum-mechanical scattering kernel describing the thermal neutron cross-sections can be derived, as for instance in [54], [55] or [56]. Cross-sections are obtained by applying Fermi's Golden Rule (which describes the transition rate from an initial energy eigenstate of a quantum system to eigenstates after perturbation by a potential) and the definition of the scattering amplitude $f(\vec{k}, \vec{k}')$ which is a function of the appropriate wave function of the system and the potential of the scatterer [56, p. 6]:

$$\frac{d\sigma}{d\Omega} = \frac{k'}{k} |f(\vec{k}, \vec{k}')|^2 \quad (\text{C.1})$$

where \vec{k} is the wave vector of the initial and \vec{k}' of the final state. In order to calculate the cross-sections, as performed in [54], one would begin with the Schrödinger equation for the system with appropriate boundary conditions. They are that a sum of an incoming plane wave and an outgoing spherical wave is obtained at large separations between neutron and scatterer. Then, the first order Born approximation is used which replaces the outgoing wave function by a plane-wave wave function, assuming that the perturbation on the incident wave is small. This assumption is reasonable as the range of nuclear forces is extremely small compared to the relevant dimensions. Finally, it must be considered that the moderator is in a state of thermal motion which is described by the Boltzmann distribution. The result of this derivation is [36]

$$\sigma(E \rightarrow E', \mu) = \frac{\sigma_b}{2kT} \sqrt{\frac{E'}{E}} S(\alpha_{sc}, \beta_{sc}) \quad (\text{C.2})$$

where E and E' are the incident and final neutron energies, μ is the cosine of the scattering angle, σ_b is the bound scattering cross-section which is material-specific

(see further information in [55, pp. 23]), kT is the thermal energy and $S(\alpha_{sc}, \beta_{sc})$ is the so-called scattering law which depends only on the momentum transfer α_{sc} and the energy transfer β_{sc}

$$\alpha_{sc} = \frac{E' + E - 2\sqrt{E'E}\mu}{BkT} \quad \beta_{sc} = \frac{E' - E}{kT} \quad (\text{C.3})$$

where B is the ratio of scatterer mass to neutron mass. Therefore, $S(\alpha_{sc}, \beta_{sc})$ does not depend on the incident neutron energies.

The scattering law must be evaluated for the specific scatterer. For crystalline solids, it can be assumed that the individual atoms in a lattice act as coupled harmonic oscillators [54], where the vibrations are described by phonons. Energy transfer corresponds to phonon excitation [36]. For such a system, the scattering law is expressed as a series showing the contributions of 0, 1, ..., n phonons [36]:

$$S(\alpha_{sc}, \beta_{sc}) = \exp \left[-\alpha_{sc} \int_{-\infty}^{\infty} \frac{\rho(\beta'_{sc})}{2\beta_{sc} \cdot \sinh(\beta'_{sc}/2)} e^{-\beta'_{sc}/2} d\beta'_{sc} \right] \cdot \left\{ \sum_{n=0}^{\infty} \frac{1}{n!} \alpha_{sc}^n \frac{1}{2\pi} \int_{-\infty}^{\infty} e^{i\beta_{sc}t} \left[\int_{-\infty}^{\infty} \frac{\rho(\beta''_{sc})}{2\beta''_{sc} \cdot \sinh(\beta''_{sc}/2)} e^{-\beta''_{sc}/2} e^{-i\beta''_{sc}t} d\beta''_{sc} \right]^n dt \right\} \quad (\text{C.4})$$

where β'_{sc} and β''_{sc} have the same definition as in equation C.3. $\rho(\beta_{sc})$ is the frequency spectrum of excitations in the system. The thermal cross-sections can be calculated when the material-specific frequency distribution is known.

Polyethylene consists of long hydrocarbon chains and is partially crystalline. The coupling between neighboring chains is rather weak so that the spectrum can be derived from evaluating a single chain [38]. In polyethylene, vibrations come from stretching, bending, wagging, rocking, torsion and twisting. Nine major modes corresponding to these types of vibration have been identified. From the frequency spectrum, the scattering cross-sections can be calculated using the equations given above. Sprevak and Koppel [38] performed these two steps and their results can be seen in Fig. C.1 and 4.1.

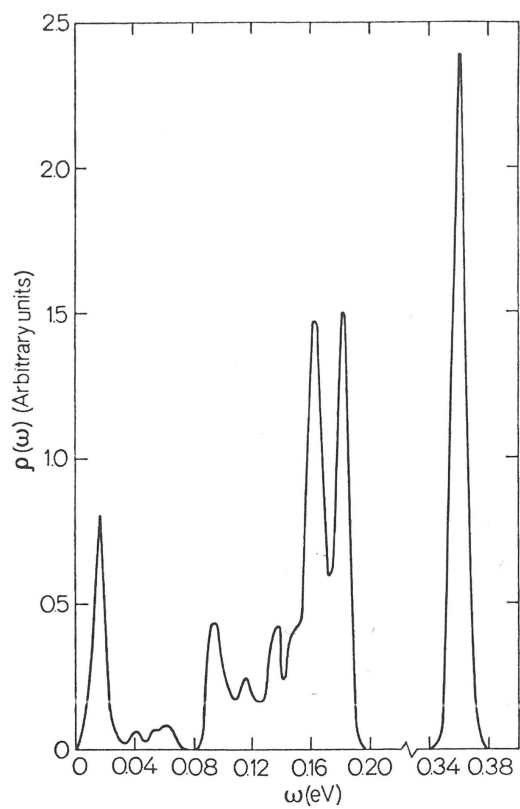


Figure C.1: Phonon frequency spectrum for the polyethylene chain used in the neutron calculations, taken from [38]

Appendix D

Derivation of the Corrected Multiplicity Analysis

The following derivation leads to the solution of equations 5.12 for M , α and F . First, S is solved for $1 + \alpha$, then the result is inserted into D which is solved for F , the result is inserted into T :

$$1 + \alpha = \frac{S}{F \cdot \epsilon \cdot M \cdot \nu_{sf1}} \quad (\text{D.1})$$

$$\implies D = \frac{F \cdot \epsilon^2 \cdot f_d \cdot M^2}{2} \left[\nu_{sf2} \cdot g_2 + (g_3 \cdot M - g_2) \frac{\nu_{i2}}{\nu_{i1} - 1} \left(\frac{S}{F \cdot \epsilon \cdot M} \right) \right] \quad (\text{D.2})$$

$$\implies F = \frac{2}{\epsilon^2 \cdot f_d \cdot M^2 \cdot \nu_{sf2} \cdot g_2} \left[D - \frac{\epsilon \cdot f_d \cdot M \cdot \nu_{i2} \cdot S}{2(\nu_{i1} - 1)} (g_3 \cdot M - g_2) \right] \quad (\text{D.3})$$

$$\implies 1 + \alpha = \frac{\epsilon \cdot f_d \cdot M \cdot \nu_{sf2} \cdot g_2 \cdot S}{2\nu_{sf1}} \left[D - \frac{\epsilon \cdot f_d \cdot M \cdot \nu_{i2} \cdot S}{2(\nu_{i1} - 1)} (g_3 \cdot M - g_2) \right]^{-1} \quad (\text{D.4})$$

$$\begin{aligned} \implies T = & \left(\frac{1}{f_d \cdot \nu_{sf2} \cdot g_2} \left[D - \frac{\epsilon \cdot f_d \cdot M \cdot \nu_{i2} \cdot S}{2(\nu_{i1} - 1)} (g_3 \cdot M - g_2) \right] \right) \frac{\epsilon \cdot f_t \cdot M}{3} \cdot \\ & \left\{ \nu_{sf3} \cdot g_3 + (g_4 \cdot M - g_3) \cdot \frac{\nu_{sf1} \cdot \nu_{i3}}{\nu_{i1} - 1} \cdot \right. \\ & \left. \left(\frac{\epsilon \cdot f_d \cdot M \cdot \nu_{sf2} \cdot g_2 \cdot S}{2\nu_{sf1}} \left[D - \frac{\epsilon \cdot f_d \cdot M \cdot \nu_{i2} \cdot S}{2(\nu_{i1} - 1)} (g_3 \cdot M - g_2) \right]^{-1} \right) + \right. \\ & \left. 3 \cdot (g_4 \cdot M - g_3) \cdot \frac{\nu_{sf2} \cdot \nu_{i2}}{\nu_{i1} - 1} + 3(g_5 \cdot M^2 - 2g_4 \cdot M + g_3) \cdot \right. \\ & \left. \frac{\nu_{i2}^2}{(\nu_{i1} - 1)^2} \cdot \frac{\epsilon \cdot f_d \cdot M \cdot \nu_{sf2} \cdot g_2 \cdot S}{2} \left[D - \frac{\epsilon \cdot f_d \cdot M \cdot \nu_{i2} \cdot S}{2(\nu_{i1} - 1)} (g_3 \cdot M - g_2) \right]^{-1} \right\} \quad (\text{D.5}) \end{aligned}$$

After simplifications and transformations, one obtains

$$\begin{aligned}
0 = & \left[D - \frac{\epsilon \cdot f_d \cdot M \cdot \nu_{i2} \cdot S}{2(\nu_{i1} - 1)} (g_3 \cdot M - g_2) \right]^{-1} \cdot \\
& \left\{ -T \left[D - \frac{\epsilon \cdot f_d \cdot M \cdot \nu_{i2} \cdot S}{2(\nu_{i1} - 1)} (g_3 \cdot M - g_2) \right] + \right. \\
& \left. \left[\frac{D \cdot \epsilon \cdot f_t \cdot M}{3f_d \cdot \nu_{sf2} \cdot g_2} - \frac{\epsilon^2 \cdot f_t \cdot M^2 \cdot \nu_{i2} \cdot S(M \cdot g_3 - g_2)}{6(\nu_{i1} - 1)\nu_{sf2} \cdot g_2} \right] \cdot \right. \\
& \left. \left\{ \frac{M \cdot \epsilon \cdot f_d \cdot \nu_{sf2} \cdot g_2 \cdot \nu_{i3} \cdot S(g_4 \cdot M - g_3)}{2(\nu_{i1} - 1)} + \right. \right. \\
& \left. \frac{3 \cdot g_4 \cdot \nu_{sf2} \cdot \nu_{i2} \cdot M}{\nu_{i1} - 1} \left[D - \frac{\epsilon \cdot f_d \cdot M \cdot \nu_{i2} \cdot S}{2(\nu_{i1} - 1)} (g_3 \cdot M - g_2) \right] - \right. \\
& \left. \frac{3g_3 \cdot \nu_{sf2} \cdot \nu_{i2}}{\nu_{i1} - 1} \left[D - \frac{\epsilon \cdot f_d \cdot M \cdot \nu_{i2} \cdot S}{2(\nu_{i1} - 1)} (g_3 \cdot M - g_2) \right] + \right. \\
& \left. \frac{3M\nu_{i2}^2 \cdot \epsilon \cdot f_d \cdot \nu_{sf2} \cdot g_2 \cdot S(g_5 \cdot M^2 - 2g_4M + g_3)}{2(\nu_{i1} - 1)^2} + \right. \\
& \left. \left. \nu_{sf3} \cdot g_3 \left[D - \frac{\epsilon \cdot f_d \cdot M \cdot \nu_{i2} \cdot S}{2(\nu_{i1} - 1)} (g_3 \cdot M - g_2) \right] \right\} \right\} \tag{D.6}
\end{aligned}$$

After some rearrangement, one arrives at equation 5.17.

Appendix E

Graphs of the Correction Coefficients

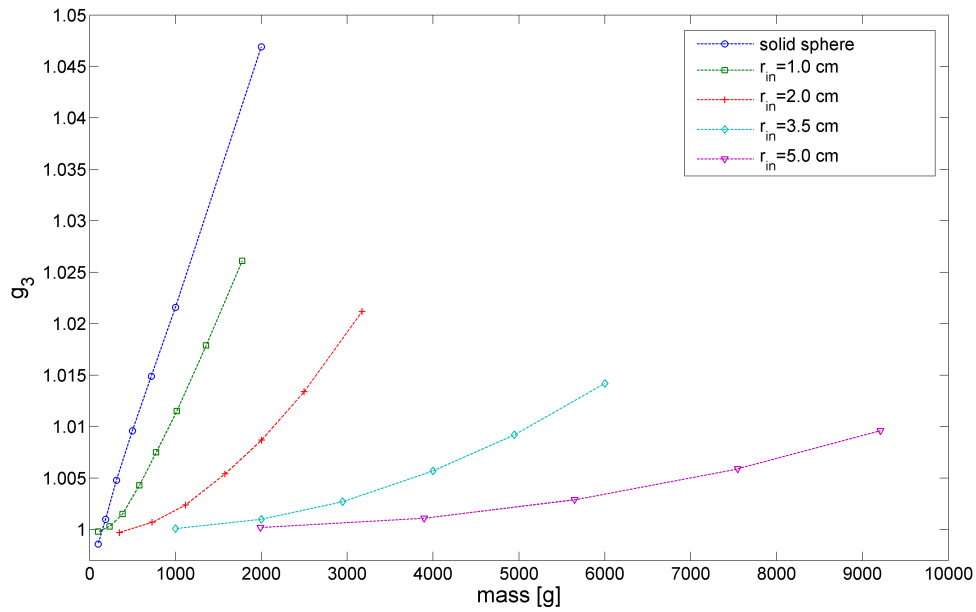


Figure E.1: g_3 as a function of fissile mass for a range of simulations. Dots represent simulated configurations, the lines are for guiding the eyes only and connect simulations of the same same r_{in} .

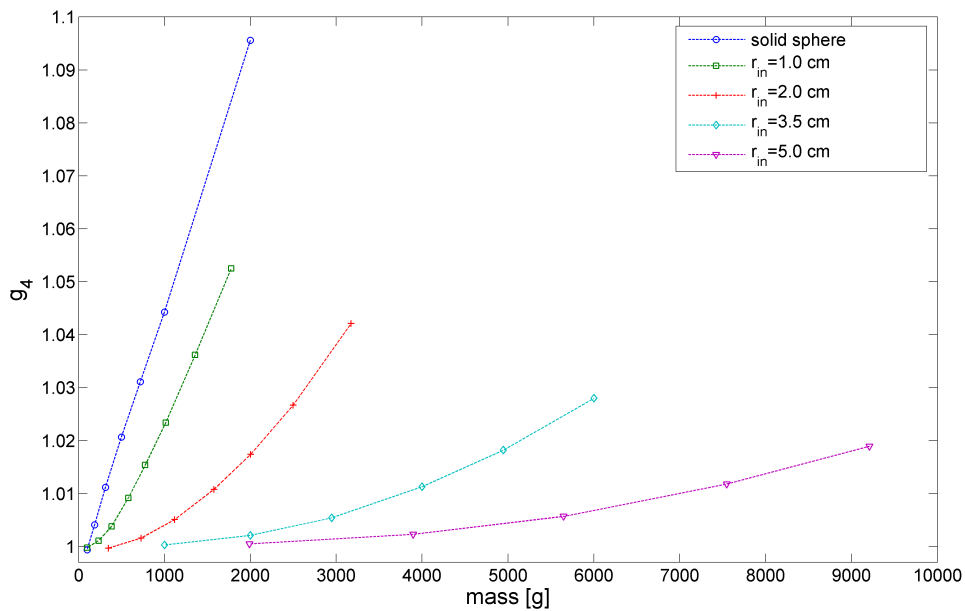


Figure E.2: g_4 as a function of fissile mass for a range of simulations. Dots represent simulated configurations, the lines are for guiding the eyes only and connect simulations of the same same r_{in} .

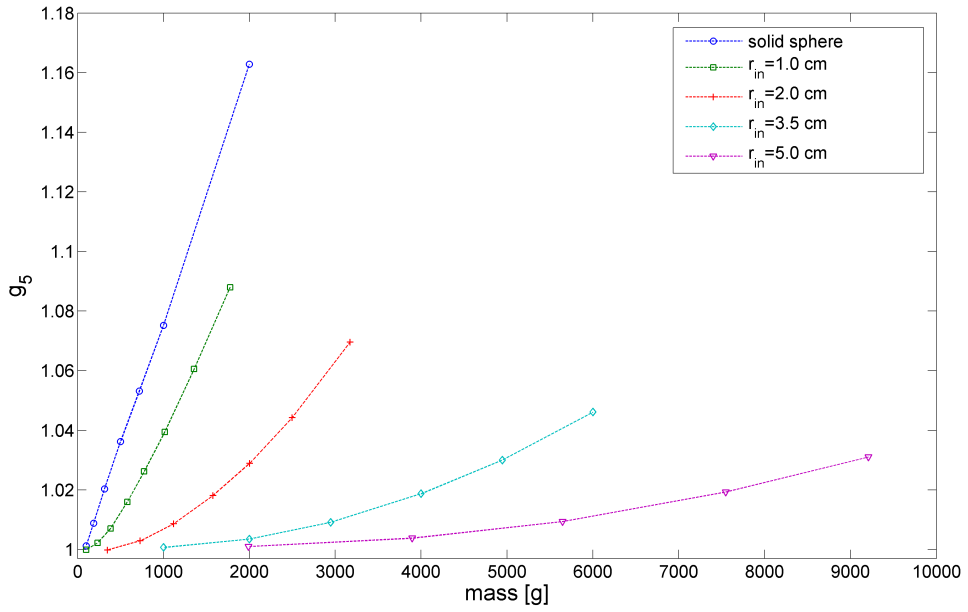


Figure E.3: g_5 as a function of fissile mass for a range of simulations. Dots represent simulated configurations, the lines are for guiding the eyes only and connect simulations of the same same r_{in} .

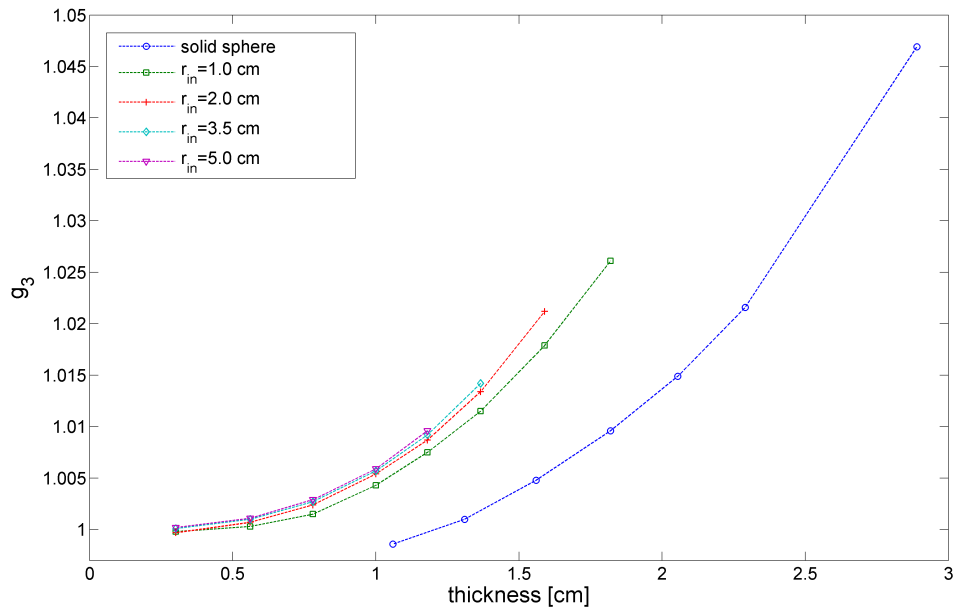


Figure E.4: g_3 as a function of thickness for a range of simulations. Dots represent simulated configurations, the lines are for guiding the eyes only and connect simulations of the same same r_{in} .

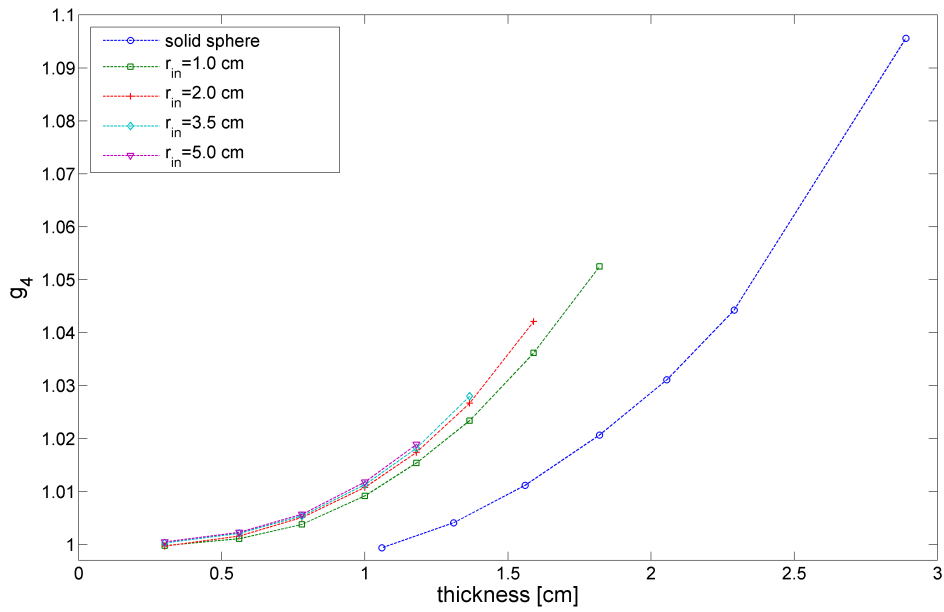


Figure E.5: g_4 as a function of thickness for a range of simulations. Dots represent simulated configurations, the lines are for guiding the eyes only and connect simulations of the same same r_{in} .

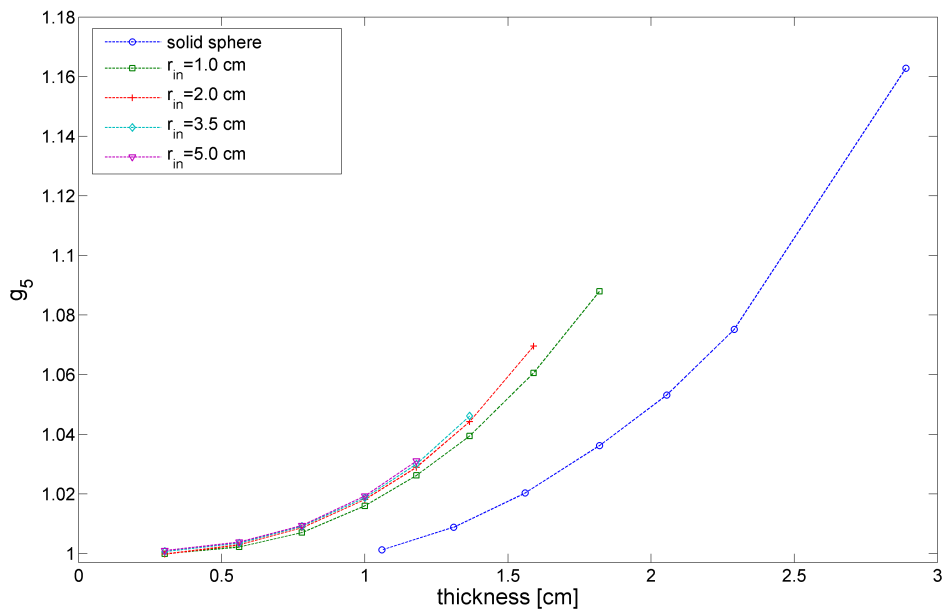


Figure E.6: g_5 as a function of thickness for a range of simulations. Dots represent simulated configurations, the lines are for guiding the eyes only and connect simulations of the same same r_{in} .

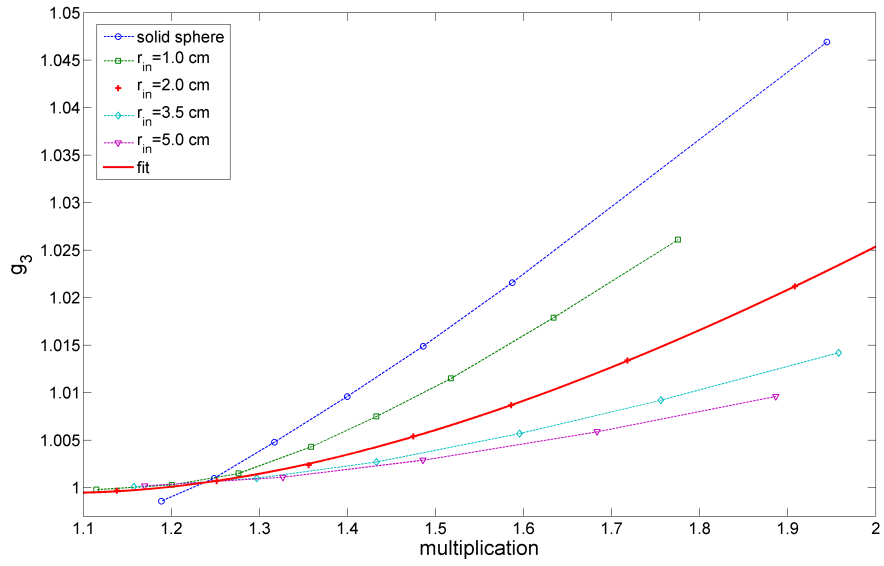


Figure E.7: g_3 as a function of M for a range of simulations. Dots represent simulated configurations, the dotted lines are for guiding the eyes only and connect simulations of the same same r_{in} , the solid line is an empirical fit to the $r_{in} = 2.0$ cm data.

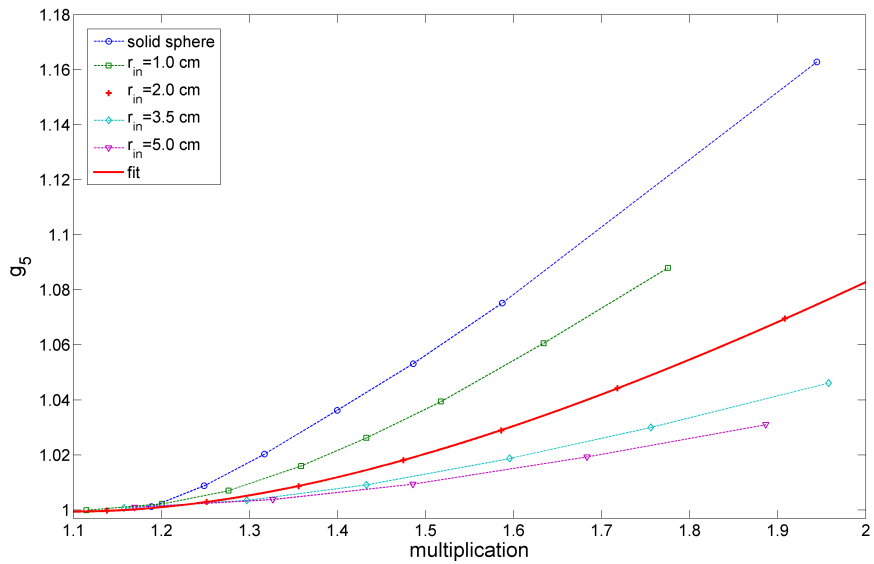


Figure E.8: g_4 as a function of M for a range of simulations. Dots represent simulated configurations, the dotted lines are for guiding the eyes only and connect simulations of the same same r_{in} , the solid line is an empirical fit to the $r_{in} = 2.0$ cm data.

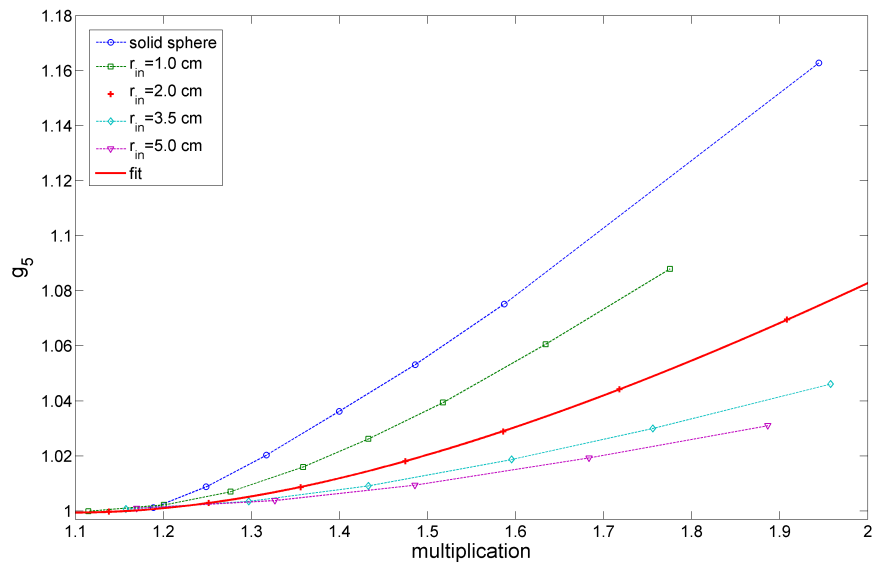


Figure E.9: g_5 as a function of M for a range of simulations. Dots represent simulated configurations, the dotted lines are for guiding the eyes only and connect simulations of the same same r_{in} , the solid line is an empirical fit to the $r_{in} = 2.0 \text{ cm}$ data.